# CONSTRAINED GPS-BASED PRECISE ORBIT DETERMINATION OF LOW EARTH ORBITERS

Amandeep Mander

A THESIS SUBMITTED TO THE FACULTY OF GRADUATE STUDIES

IN PARTIAL FULFILLMENT OF THE REQUIREMENTS

FOR THE DEGREE OF

MASTER OF SCIENCE

GRADUATE PROGRAM IN PHYSICS AND ASTRONOMY

YORK UNIVERSITY

TORONTO, ONTARIO

July, 2011

**CONSTRAINED GPS-BASED PRECISE ORBIT DETERMINATION OF LOW EARTH ORBITERS**

by **Amandeep Mander**

a thesis submitted to the Faculty of Graduate Studies of York University in partial fulfillment of the requirements for the degree of

**MASTER OF SCIENCE**

**CONSTRAINED GPS-BASED PRECISE ORBIT DETERMINATION OF**

**LOW EARTH ORBITERS**

by **Amandeep Mander**



Examination Committee members:

1. Sunil Bisnath
2. Jian-Guo Wang
3. Jinjun Shan
4. Regina Lee
5. Michael De Robertis
6. Spiros Pagiatakis

# Abstract

The Global Positioning System (GPS) is a proven technology that can be used to determine the position and velocity of a low Earth orbiting satellite. By combining spaceborne GPS measurements with various high-fidelity dynamic models for the Low Earth Orbiter (LEO) via a Kalman filter/smoother, the position and velocity of the LEO can be determined at the subdecimetre-level, referred to as Precise Orbit Determination (POD). Such accuracy can only be achieved if the GPS data are continuous, post-processed and a dual-frequency receiver is utilized. The focus of this study is to analyze the degradations in position accuracy in the presence of various constraints. The results of this work are processing and analysis software that can be used as a mission data processing and planning tool for GPS LEO POD. Based on mission-specific constraints and requirements, degradations in accuracy from a reference solution are determined based on actual data. The experiments are conducted with 6-hour data arcs for 7 separate days with data from the CHAllenging Mini-Satellite Payload (CHAMP). A 3D root mean square (rms) error of 15 cm is observed in the reference solution. Various levels of accuracy degradations are observed as constraints are placed on this reference solution. The rms error of the post-processed, single-frequency solution is 68 cm and 1.3 m for the real-time, dual-frequency solution. In very challenging environments, for example, with the receiver on for only 10 minutes of a 90 minute orbit, the 3D rms increases to 350 m.

## Acknowledgements

I would like to thank my supervisor, Professor Sunil Bisnath for all the support and encouragement that he has offered me throughout this research. Not only has he helped me in expanding my knowledge in the field of satellite positioning and navigation, but taught me general life skills as well, that will take me a long way in life. I would also like to thank my family and friends for providing me with the motivation to keep going. Special thanks to NSERC for the financial support to make this research possible. I would also like to acknowledge JPL, CDAAC, CDDIS and NRCan for providing data used in the experiments.

# Table of Contents

# List of Tables

# List of Figures

# Acronyms

| | |
|---|---|
| **CDAAC** | COSMIC Data Analysis and Archive Centre |
| **CDDIS** | Crustal Dynamics Data Information System |
| **CHAMP** | CHAllenging Mini-Satellite Payload |
| **CSRS-PPP** | Canadian Spatial Reference System-Precise Point Positioning |
| **EIGEN** | CHAMP Gravity Model |
| **EKF** | Extended Kalman Filter |
| **GGM02** | GRACE Gravity Model |
| **GMST** | Greenwich Mean Sidereal Time |
| **GPS** | Global Positioning System |
| **GRACE** | Gravity Recovery and Climate Experiment |
| **GRAPHIC** | GRoup And PHase Ionospheric Correction |
| **ICRS** | International Celestial Reference System |
| **IERS** | International Earth Rotation and Reference Systems Service |
| **IGS** | International GPS Service |
| **ITRF** | International Terrestrial Reference System |
| **JGM-3** | Joint Gravity Model |
| **JPL** | Jet Propulsion Laboratory |
| **LEO** | Low Earth Orbiter |
| **NORAD** | North American Aerospace Defense |

| | |
|---|---|
| **NRCAN** | Natural Resources of Canada |
| **PDOP** | Position Dilution of Precision |
| **POD** | Precise Orbit Determination |
| **PPP** | Precise Point Positioning |
| **PRARE** | Precise Range and Range Rate Equipment |
| **RINEX** | Receiver INdependent EXchange |
| **rms** | Root Mean Square |
| **SI** | International System of Units |
| **SLR** | Satellite Laser Ranging |
| **TAI** | International Atomic Time |
| **TOA** | Time of Arrival |
| **TT** | Terrestrial Time |
| **UT1** | Universal Time |
| **UTC** | Coordinated Universal Time |

# Chapter 1

# 1 Introduction

Satellite positioning has now been conducted for many decades, with many applications such as determination of the Earth's gravity field, study of geodynamics, tomography of the atmosphere and communications (Seeber, 2003). The techniques utilized in the determination of satellite position have evolved since their inception. This study focuses on the positioning of satellites that are in low Earth orbit (LEO), which are satellites that orbit at altitudes as low as a few hundred kilometres, and as high as 1000 km. A more recent method for determining the position of a LEO is GPS. This chapter presents an introduction to orbital mechanics and tracking techniques, followed by an introduction to GPS. The thesis objects, novelty and outline are presented thereafter.

## 1.1 Orbital Mechanics

There are many different levels of complexity involved in the determination of the position or velocity of a satellite in orbit around the Earth. If the Earth were a perfectly spherical body of uniform density, its gravitational effects would be easy to calculate from a point mass approximation. Unfortunately, the Earth is not a perfect sphere, but has the form of an oblate spheroid and contains a non-uniform mass density. Thus the complexity of the gravitational model needs to be increased in order to accurately determine the gravitational force on an object due to the Earth. Other than the Earth, third-body gravitational forces also exist on a satellite with the Sun and Moon being the largest contributors. Other significant forces, which will be discussed in more detail below, include solar radiation pressure, air drag and relativistic effects. Since an analytical solution only exists for the two-body problem, the acceleration on a satellite is determined from fully perturbed equations of motion that require numerical integration (Beutler, 2005).

## 1.2 Tracking Techniques

The objective of orbit determination of artificial Earth satellites is mainly to determine the position and velocity of the satellite and predict future and past states, which are a function of time. Some of the early techniques for orbit determination involved angle measurements. The method of accurately determining the position of celestial objects with angle measurements began in the seventeenth century with the advent of the telescope to study the stars (Connexions, 2004). In order to determine the position of satellites, the optics-based measurements were replaced with radio wave measurements. The accuracies obtained by angle measurements vary from 100 m to 5000 m depending on the altitude of the object. A major problem with angle measurements is that they are significantly affected by systematic errors such as calibration deficiencies, thermoelastic distortions, and wind or snow loads (Montenbruck and Gill, 2005). The way to obtain such a measurement is to have the satellite emit a radio signal and have an antenna on the ground track the signal (Hightower and Borriello, 2001). Another technique that is quite common for orbit determination is two-way radar ranging. The ground station sends a signal to the satellite and the satellite's transponder receives the signal and sends it back to the ground station. From the signal travel time, the range between the ground station and the satellite can then be determined (Gaudenzi et al., 1993). A successful system that provides high-precision, two-way range and range rate measurements is the spaceborne tracking system PRARE (Precise Range and Range Rate Equipment), which can provide the position of a satellite accurate to less than 10 cm (Andersen et al., 1998). If the satellite, or any other object is not equipped with a transponder, it is still possible to track it using radar. A radar system sends out radar signals and when these signals strike any spaceborne objects, a small percentage of them bounce off the objects and return back to the antenna. This is how North American Aerospace Defense (NORAD) tracks objects orbiting the Earth, with accuracy levels of approximately 1 km (NORAD, 2011). Doppler tracking is another commonly used orbit determination technique that is based on the frequency shift of radio waves. The frequency shift is dependent on the relative motion between the ground station and the satellite (Glish, 1971). An example of a precise Doppler tracking system is the DORIS (Doppler Orbitography and Radiopositioning Integrated by Satellite), which is accurate to within 1.5 cm (Willis et al., 2004). A relatively more modern approach that is in wide use today is satellite laser ranging (SLR), which precisely measures the range between a laser station on the ground and the satellite's retroreflector. This technique is proven to be as accurate as one centimetre

(Marshall et al., 1995). The major downside to SLR is that it requires a global network of observation stations and can thus prove to be very expensive. A global network of observation stations for SLR is required since SLR works by measuring the round trip time of pulses of light. The measurements used for orbit determination in this study are from GPS, which utilizes the concept of one-way ranging of radio signals. GPS provides an excellent alternative to the other methods due to its ability to provide decimetre-level accuracy with global continuous coverage with just a simple, relatively inexpensive, spaceborne GPS receiver.

## 1.3 Global Positioning System

Positioning and navigation have always been very important aspects in human history. In the 1960s, it was the goal of the U.S. government to develop an optimum positioning and navigation system that had global continuous coverage and all weather operation, with the ability to serve high-dynamic platforms and provide good accuracy. With these goals came the advent of GPS that provides accurate, continuous, three-dimensional position, velocity and time of an object almost anywhere in the world with the appropriate receiving equipment. The current GPS constellation consists of 32 satellites. The GPS satellites contain atomic clocks for accurate timing, which operate close to the GPS timescale. In order to assign a position to the receiver, GPS uses the intersection of 3 spheres. Therefore, at least 4 satellites must be in the line of sight of the receiver in order obtain a position: 3 for spatial positioning and 1 for the receiver clock offset correction (Kaplan and Hegarty, 2006).

The concept of one-way time of arrival (TOA) ranging is utilized in GPS. The GPS satellites broadcast ranging codes and navigation data on two frequencies: L1 (1575.42 MHz) and L2 (1227.60 MHz), and a third frequency, L5, coming soon. There exist short codes known as coarse/acquisition (C/A) broadcast at a rate of 1 Mbps (repeats after 1 ms) and precision codes known as P(Y) code broadcast at a rate of 10 Mbps (repeats after 266 days). The receiver utilizes these time-tagged signals to determine the range to each GPS satellite in view by measuring signal travel time, which is then scaled by the speed of light to estimate range. The problem is that the GPS satellite clock and the receiver clock are not synchronized; hence the term *pseudorange* is used to refer to the range measurements. Another more accurate strategy is to use the underlying carrier-phase observables, which is a count of the number of carrier wave cycles of the signal since acquisition. Since the raw carrier-phase measurements are just a measure of the number of carrier wave cycles and do not contain the time-of-transmission information as is the case with the code measurements, the receiver cannot discriminate one wavelength from another. This inability of the receiver to differentiate between the cycles is what gives the carrier-phase measurements their ambiguous nature. Although providing accurate measurements, the pitfall in using the carrier-phase measurements along with its ambiguous nature is that there may exist discontinuities in the measurements, known as *cycle slips*. Nonetheless, many different methods have been developed to solve for the ambiguities and handle cycle slips without causing a large degradation to positioning accuracy (El-Rabbany, 2002). The positional accuracy obtained from utilizing GPS ranges from tens of metres to millimetres, depending on how well the errors in the measurements are handled. There exist random and systematic errors in GPS measurements, as summarized in Table 1.1 (Leick, 2004).

| **Name** | **Error** |
|---|---|
| **Generation** | |
| Orbit | ~1 – 5 m |
| Clock | ~1 – 5 m |
| Antenna Biases | ~0 – 2.5 m |
| Hardware Biases | ~few cm – few dm |
| **Transmission** | |
| Ionospheric Refraction | ~0 – 15 m |
| Tropospheric Refraction | ~0 – 15 m |
| **Reception** | |
| Multipath | ~few cm – few dm |
| Antenna Biases | ~few cm – few dm |
| Receiver Noise | ~few cm – few dm |

Table 1.1 Major GPS error sources

GPS is applicable but not limited to the following industries: utilities, forestry and natural resources, precision farming, civil engineering, monitoring structural deformations, open-pit mining, land seismic surveying, marine seismic surveying, airborne mapping, seafloor mapping, vehicle navigation, transit systems, retail, defence, surveying and many more. (Kaplan and Hegarty, 2006). There exist various modes of GPS operation, with accuracy levels ranging from tens of metres to just a few centimetres. One mode of GPS operation is single point positioning, which provides a position solution accurate to within 16 m (3D). Most hand held receivers available at retail stores operate in single point positioning mode. If an application demands more accuracy, one can switch to relative GPS or Precise Point Positioning (PPP). PPP, which can achieve centimetre-level accuracy, is discussed in more detail in section 3.2. Relative GPS, which can achieve accuracy levels of just a few centimetres, utilizes a base receiver whose position is known and a rover receiver that is placed over a location whose position is to be determined. In order to increase the accuracy of the position solution, one can use the carrier-phase measurement under the relative GPS mode. This technique allows for accuracy levels of just a few centimetres, and is typically used where very accurate positioning is required such as in construction or surveying (NRCan, 2007).

## 1.4 Recent Research

Since the beginning of the 1990s, the use of observations from GPS data for precise orbit determination (POD) has been an attractive area of research. Yunck et al. (1990) proposed a method known as the reduced dynamic technique, which combines the GPS measurements with dynamic modelling to determine the orbit of a LEO. The reduced dynamic technique, which was first demonstrated on the TOPEX/POSEIDON mission in 1992, promised to offer subdecimetre tracking accuracy. TOPEX/POSEIDON was one of the first major scientific missions where GPS was being utilized for LEO orbit determination. After the success of the reduced dynamic technique, much work was done on improving the force models as well as increasing the efficiency of the technique. For example, real-time on-board orbit determination is a requirement for many missions and thus requires a high degree of efficiency in the orbit determination process. The implemented dynamic models typically require numerical integration in order to be solved, but much work has been performed that explore the merits of analytical force models in order to increase the efficiency of the processor (Montenbruck, 2000). Although more efficient, the analytical force models do not provide the same level of accuracy as the numerical models. Traditionally, accuracies at the decimetre-level could only be obtained with use of double-differenced measurements. Processing strategies using double-difference measurements with the ability to achieve such accuracies has been demonstrated in studies such as Svehla and Rothacher (2003) and Jaggi et al. (2007). The limitation of using double-differenced measurements for LEO orbit determination is that a global ground station network must be utilized. Researchers in the field thus began to improve processing strategies using undifferenced GPS measurements. The launch of the CHAllenging Mini-Satellite Payload (CHAMP) satellite then further fueled activities improving strategies and algorithms for LEO POD, which is also accurate to the decimetre level (Hugentobler and Beutler, 2003). New techniques such as those involving the kinematic and reduced-dynamic approach simultaneously were explored to improve accuracy and efficiency levels (Colombo and Luthcke, 2004). Due to the flexibility and improvement in the methods developed for orbit determination, work then began on constrained orbits, where ideal conditions that provide maximum accuracy were not available. Techniques to improve accuracy levels in orbits with requirements such as real-time processing were explored (Yoon et al., 2004). Hardware constraints such as the use of a single-frequency receiver rather than a dual-frequency receiver would also cause a loss in accuracy. Thus, choosing appropriate processing techniques when processing single-frequency data are crucial, as explored by Jaggi et al. (2008).

## 1.5 Thesis Objectives

Nanosatellites, which are very small satellites weighing typically between 1 kg and 10 kg, are becoming popular for their low cost and growing scientific and commercial capabilities. Such satellites can carry a GPS receiver, but in many cases would contain single-frequency receivers, require positioning information in real-time and would be unable to operate the receiver continuously due to onboard resource constraints. Resource constraints may also apply to larger satellites, if other resource consuming electronics such as cameras or other sensors are included. Due to such constraints, the GPS receiver cannot be used to its full potential. In situations where positioning information is required in real-time and processing time or processing capabilities needs to be conserved, the use of dynamic modelling also becomes limited.

The objective of this research is to quantitatively explore the accuracy levels in the positioning of a LEO under constrained circumstances based on a variety of parameters. In order to accomplish this task, a flexible piece of software has been developed in MATLAB. The description of the software is given in Appendix A. The software has been developed from first principles, containing various components. The first component is the dynamic modelling that describes a LEO with the ability to accurately predict future states (position and velocity). The second component is the GPS measurement processor, where the GPS measurements are used to produce an accurate state. These two components are then combined using the reduced dynamic technique to produce a more accurate and reliable continuous solution. Once the reduced dynamic orbit has been developed, various constraints are then applied to this reference solution and the degradation in accuracy is observed. The most accurate positioning solution is produced by post-processing dual-frequency data from a continuously operating receiver with the utilization of full dynamic models. A constraint such as real-time processing rather than post-processing will reduce the accuracy of the solution. The purpose of this research is to determine the absolute and relative decrease in accuracy from the reference solutions under various constraints. The constraints explored in this study are real-time processing requirements, availability of only single-frequency data, use of limited dynamic models and non-continuous GPS receiver operation.

## 1.6 Research Contributions

Accuracy at the decimetre level can only be achieved under the best cases: post-processing dual-frequency data with continuous receiver operation. In smaller LEOs, particularly nanosatellites, such requirements may not be attainable. For example, due to budget constraints, a single-frequency receiver may be installed. The low power budget on a nanosatellite also poses constraints due to the fact that the GPS receiver may not be powered on at all times. The different constraints will affect the accuracy of the solution differently. Although much work has been done to improve methods for single-frequency data, real-time requirements and the reduced dynamic technique itself, the implications of small or large data gaps have not been thoroughly explored. The novelty of this research is that the decrease in accuracy with the various constraints will be provided quantitatively, with an emphasis on small and large GPS data gaps. The small and large GPS data gaps result from non-continuous receiver operation, which is common in nanosatellites with a low power budget. The following experiments will help determine the types of accuracies to expect based on mission requirements. This information is also crucial during mission planning when estimating the costs associated with positioning requirements based on the mission.

## 1.7 Thesis Outline

Chapter 2 provides an in-depth discussion of the dynamic models associated with a LEO along with a discussion on CHAMP and its associated reference solution. Chapter 3 provides details of the measurement models and outlier elimination methods utilized in the GPS processor. The results for the position solution of the LEO using the sequential least-squares method processing only the GPS measurements are also presented. Chapter 4 introduces the reduced dynamic technique and presents the results for the reduced dynamic orbit solution. Chapter 5 discusses the results of the experiments exploring the various constraints. Extreme cases, typical in nanosatellites where the duty cycle of the receiver is very low are analyzed in Chapter 6. Finally, Chapter 7 summarizes all the findings and provides suggestions for future work.

# Chapter 2

## 2 Dynamic Orbit

This chapter presents the background and the experimental results of the dynamic modelling utilized in this study. A more in depth discussion on the dynamic modelling can be found in textbooks such as Beutler (2005) and Montenbruck and Gill (2005). There are two major types of forces that act on a LEO: gravitational forces and non-gravitational forces. The gravitational forces arise from Earth's gravitational field and third-body perturbations. The major non-gravitational forces acting on the LEO are solar radiation pressure and air drag. The total force acting on the LEO can be determined by solving the following equations of motion (Erdogan and Karsioglu, 2009):

$$\ddot{\boldsymbol{r}} = \boldsymbol{a}_{\boldsymbol{g}} + \boldsymbol{a}_{\boldsymbol{ng}} \tag{2.1}$$

where

$\ddot{\boldsymbol{r}}$ = second derivative of the position of the LEO's centre of mass

$\boldsymbol{a}_{\boldsymbol{g}}$ = total acceleration acting on the LEO from gravitational forces

$\boldsymbol{a}_{\boldsymbol{ng}}$ = total acceleration acting on the LEO from non-gravitational forces

In order to utilize the force models, a good understanding of the time and coordinate systems used in orbit determination is required. All required parameters to transform between time and coordinate systems are available from the International Earth Rotation and Reference Systems Service (IERS) (IERS, 2010).

## 2.1 Time Systems

There exist many time scales that are used in the precision modelling of LEOs including Terrestrial Time (TT), International Atomic Time (TAI), GPS Time (GPST), Greenwich Mean Sidereal Time (GMST), Universal Time (UT1) and Coordinated Universal Time (UTC). Terrestrial Time consists of days comprised of 86400 SI seconds and is used as the independent argument to calculate the precession and nutation of the Earth. Universal Time is the current realization of a mean solar time, which can be determined from the Greenwich Mean Sidereal Time. Terrestrial Time, International Atomic Time, GPS Time and Coordinated Universal Time are timescales based on atomic clocks. International Atomic Time relates to Terrestrial Time in the following manner (Montenbruck and Gill, 2005):

$$TT = TAI + 32.184\ s \tag{2.2}$$

GPS Time also works on the principle of atomic time and currently differs from International Atomic Time by 19 s:

$$GPS = TAI - 19\ s \tag{2.3}$$

The time of origin of GPS Time, chosen arbitrarily, is the same as that of Coordinated Universal Time on 1980 January 6.0 UTC. GMST is also known as the Greenwich Hour

Angle and represents an angle between the mean vernal equinox of date and the Greenwich meridian. GMST can be expressed as either an angle between 0 and $2\pi$ or as a time between 0 h and 24 h. Universal Time strives on achieving a constant average length of the solar day of 24 hours. Since the actual mean length of a day depends on the Earth's rotation and apparent movement of the Sun, a period of one second is not constant in Universal Time. Since the length of the day is never constant, Universal Time is defined as a function of sidereal time. $0^h$ in Universal Time is defined as the instant when GMST has the value (Aoki et al., 1982):

$$GMST\ (0^h UT1) = 24110\overset{s}{.}54841 + 8640184\overset{s}{.}812866 \cdot T_0$$
$$+ 0\overset{s}{.}093104 \cdot T_0^2 - 0\overset{s}{.}0000062 \cdot T_0^3 \tag{2.4}$$

where

$$T_0 = \frac{JD(0^h UT1) - 2451545}{36525} \tag{2.5}$$

which is the number of Julian centuries since 2000 January 1.5 UT1 at the beginning of the present day. The expression for GMST can be generalized for an arbitrary time of day:

$$GMST = 24110\overset{s}{.}54841 + 8640184\overset{s}{.}812866 \cdot T_0$$
$$+1.002737909350795\, UT1 + 0\overset{s}{.}093104 \cdot T^2 - 0\overset{s}{.}0000062 \cdot T^3 \tag{2.6}$$

where

$$T = \frac{JD(UT1) - 2451545}{36525} \quad (2.7)$$

which is the number of Julian centuries since 2000 January 1.5 UT1. The offset between UT1 and TAI is published in Bulletin B of the IERS. Coordinated Universal Time is tied to TAI, except by a constant offset that is regularly updated and published in Bulletin C of the IERS.

## 2.2 Coordinate Systems

The equations of motion that determine the force acting on the LEO require an inertial reference system: a reference system that is not acceleration. The inertial reference system adopted in this study is the International Celestial Reference System (ICRS) that is defined by the mean equator and vernal equinox at the Julian epoch 2000.0 (Arias et al., 1995). Since GPS calculates the position of the LEO in the International Terrestrial Reference System (ITRS), it is important to be able to transform the coordinates of the LEO between the two systems. The transformation between the two systems is achieved by accounting for precession, nutation, sidereal time and polar motion, which are all with respect to the ICRS. In general, precession is the change in the orientation of the rotation axis of a rotating body. The precession of the Earth describes the change in the orientation of the rotation axis of the Earth and the equinox, with respect to the ICRS (Lieske et al., 1977). Nutation is the back-and-forth motion in the axis of rotation of a rotating body. Thus, Nutation describes the periodic and short-term variation, with respect to the ICRS, of the equator and the vernal equinox (Seidelmann, 1982). Sidereal time describes the rotation of the Earth about its axis and polar motion describes the movement of the Earth's rotational axis about a mean axis, which is with respect to the ITRS. (Aoki et al., 1982). Therefore, in order to transform coordinates from ICRS to ITRS, the following transformation must be applied (Montenbruck and Gill, 2005):

$$\boldsymbol{r}_{ITRS} = \boldsymbol{\Pi}\left(t_{x_p,y_p}\right) \cdot \odot(t_{UT1}) \cdot \boldsymbol{N}(t_{TT}) \cdot \boldsymbol{P}(t_{TT}) \cdot \boldsymbol{r}_{\boldsymbol{ICRS}} \tag{2.8}$$

where the rotation matrices **Π**, ⊙, **N**, **P**, represent changes due to polar motion, Earth rotation, nutation and precession, respectively. The precession and nutation are a function of Terrestrial Time, Earth rotation is a function of Universal Time, and polar motion is a function of the $x_p$ and $y_p$ coordinates that are published in Bulletin B of the IERS.

## 2.3 Geopotential

The acceleration $\ddot{\boldsymbol{r}}$ felt by the LEO due to the gravitational field of the Earth can be expressed in a fashion that involves using the gradient of the gravitational potential U:

$$\ddot{\boldsymbol{r}} = \nabla U \tag{2.9}$$

Solving the above differential equation involves the use of Legendre polynomials. The Earth's gravitational potential is thereby expressed in terms of a spherical harmonic expansion that takes the form (Kaula, 1966):

$$U = \frac{GM}{r} \sum_{n=0}^{\infty} \sum_{m=0}^{n} \frac{R^n}{r^n} P_{nm}(\sin \emptyset)(C_{nm} \cos(m\lambda) + S_{nm} \sin(m\lambda)) \tag{2.10}$$

where

GM = gravitational constant of the Earth times mass of the Earth

$R^n$ = mean equatorial radius of the Earth

r = radial distance from the centre of mass of the Earth to LEO

$P_{nm}$ = associated Legendre function of degree n and order m

$C_{nm}, S_{nm}$ = spherical harmonic coefficients of degree *n* and order *m*

$\emptyset, \lambda$ = geocentric latitude and longitude, respectively

## 2.4 Sun and Moon Coordinates

In order to determine the forces acting on the satellite from celestial bodies, the coordinates of the celestial bodies are required. It is sufficient to determine the forces acting on the satellite from just the Sun and the Moon and neglect the forces from other celestial bodies. In order to calculate the solar and lunar coordinates, one can utilize advanced analytical theories or the Chebyshev approximation. It is an approximation because the polynomial must be truncated at a certain degree, thus producing an approximate instead of an exact solution. The Chebyshev approximation is used when accurate numerical values of the solar and lunar coordinates are required. For one wanting to determine the force due to the Sun and the Moon, low-precision solar and lunar coordinates are sufficient, since the coordinates are accurate to about 0.1 – 1%. In this study, since the forces exerted by the celestial bodies are much smaller than the force due to the Earth, the low-precision coordinates of the Sun and the Moon are determined from advanced analytical theories (Montenbruck, 1989; Montenbruck and Pfleger, 2000). The method used to determine the solar and lunar coordinates is described in more detail in Appendix B.

## 2.5 Sun and Moon Perturbing Acceleration

There is one general formula that can be used to model gravitational perturbations from celestial bodies. The accelerations felt by the LEO from the Sun and Moon are calculated sufficiently accurately using the following point mass approximation (Montenbruck and Gill, 2005):

$$\ddot{\boldsymbol{r}} = GM \cdot \frac{\boldsymbol{s} - \boldsymbol{r}}{|\boldsymbol{s} - \boldsymbol{r}|^3} \tag{2.11}$$

where

G = gravitational constant

M = mass of perturbing body

**r**, **s** = geocentric coordinates of the satellite and of the perturbing body, respectively

## 2.6 Solar Radiation Pressure

The LEO, due to the absorption or reflection of photons experiences a small force from solar radiation pressure. For the case of the LEO, it suffices to assume that the surface normal points in the direction of the Sun. The acceleration from solar radiation pressure can then be calculated using the following formula (Montenbruck and Gill, 2005):

$$\ddot{\boldsymbol{r}} = -PC_R \frac{A}{m} \frac{\boldsymbol{r}}{r^3} AU^2 \tag{2.12}$$

where

P = solar radiation pressure

$C_R$ = radiation pressure coefficient

A = cross-sectional area of the LEO normal to the Sun

m = mass of the LEO

$\boldsymbol{r}$ = vector pointing from the LEO to the Sun

$AU^2$ = square of distance from the Sun to the LEO (Astronomical Unit)

## 2.7 Air Drag

Air drag can be the largest non-gravitational force to be acting on the LEO. The acceleration due to air drag is modelled by (Montenbruck and Gill, 2005):

$$\ddot{\boldsymbol{r}} = -\frac{1}{2} C_D \frac{A}{m} \rho v_r^2 \boldsymbol{e}_v \qquad (2.13)$$

where

$C_D$ = drag coefficient

A = cross-sectional area of LEO normal to the velocity

m = mass of LEO

$\rho$ = atmospheric density

$v_r$ = velocity of LEO

$\boldsymbol{e}_v$ = velocity unit vector

The atmospheric density is obtained from the Harris-Priester atmospheric density coefficients (Harris and Priester, 1962).

## 2.8 Numerical Integration

The GPS receiver onboard CHAMP collects data at a frequency of once every 10 seconds. Since the state is propagated via numerical integration at each epoch of data collection, an efficient integration method is crucial, especially for real-time processing. The 4$^{th}$-order Runge-Kutta integrator is reliable and efficient for the purpose of this study (Gupta et al., 1985; Kinoshita and Nakai, 1989). The equations that need to be solved in order to propagate the state from one epoch to another are assumed to be n-dimensional, first-order differential equations:

$$\dot{\boldsymbol{y}} = \boldsymbol{f}(t, \boldsymbol{y}) \quad \boldsymbol{y}, \dot{\boldsymbol{y}}, \boldsymbol{f} \in \mathbb{R}^n \tag{2.14}$$

where

$$\boldsymbol{y} = \begin{pmatrix} \boldsymbol{r} \\ \dot{\boldsymbol{r}} \end{pmatrix} \tag{2.15}$$

where $\boldsymbol{r}$ and $\dot{\boldsymbol{r}}$ are the position and velocity of the LEO, respectively. The following differential equation is then satisfied:

$$\dot{\boldsymbol{y}} = \boldsymbol{f}(t, \boldsymbol{y}) = \begin{pmatrix} \dot{\boldsymbol{r}} \\ \boldsymbol{a}(t, \boldsymbol{r}, \dot{\boldsymbol{r}}) \end{pmatrix} \tag{2.16}$$

In order to initiate the integrator, initial values $\boldsymbol{y_0} = \boldsymbol{y}(t_0)$ are required at time $t_0$. The initial values are obtained from the GPS measurements. It is then possible to obtain the approximation of $\boldsymbol{y}$ at a later time $t_0 + h$ from a first-order Taylor expansion known as

Euler step. The 4th-order Runge-Kutta method yields the following equations for the approximation of $\boldsymbol{y}(t_0 + h)$:

$$\mathbf{y}(t_0 + h) = \boldsymbol{y_0} + \frac{1}{6}h(\boldsymbol{k_1} + \boldsymbol{2k_2} + 2\boldsymbol{k_3} + \boldsymbol{k_4}) \tag{2.17}$$

where $\frac{1}{6}(\boldsymbol{k_1} + \boldsymbol{2k_2} + 2\boldsymbol{k_3} + \boldsymbol{k_4})$ is the weighted average of the slopes, which are $\boldsymbol{k_1}, \boldsymbol{k_2}, \boldsymbol{k_3}, \boldsymbol{k_4}$:

$$\boldsymbol{k_1} = \boldsymbol{f}(t_0, \boldsymbol{y_0}) \tag{2.18}$$

$$\boldsymbol{k_2} = \boldsymbol{f}\left(t_0 + \frac{h}{2}, \boldsymbol{y_0} + \frac{h\boldsymbol{k_1}}{2}\right) \tag{2.19}$$

$$\boldsymbol{k_3} = \boldsymbol{f}\left(t_0 + \frac{h}{2}, \boldsymbol{y_0} + \frac{h\boldsymbol{k_2}}{2}\right) \tag{2.20}$$

$$\boldsymbol{k_4} = \boldsymbol{f}(t_0 + h, \boldsymbol{y_0} + h\boldsymbol{k_3}) \tag{2.21}$$

## 2.9 Overview of the CHAMP Mission and Experimental Data

CHAMP, shown in Figure 2.1, was launched from Plesetsk, Russia aboard a COSMOS launch vehicle on 15 July 2002 and re-entered the Earth's atmosphere on 20 September 2010 (GFZ, 2011). CHAMP's primary objective was geophysical research. CHAMP had a circular, near polar orbit of 94 minutes at an altitude of approximately 454 km and carried a Blackjack dual-frequency GPS receiver (Grunwaldt, 2002). The experiments conducted in this study utilize a randomly chosen 7-day consecutive period of GPS data from CHAMP. The raw files that are used as input into the processor are in the Receiver INdependent EXchange (RINEX) format. The RINEX files used are from days 115 – 121 in the year 2008. The files can be obtained from Crustal Dynamics Data Information

System (CDDIS) (CDDIS, 2009). In general, recent measurements tend to be more accurate due to improvements in receiver firmware and data processing technology. Thus data from the year 2008 were chosen so that they can provide reliable accuracy levels, the results for which can be extended to other missions and dates.

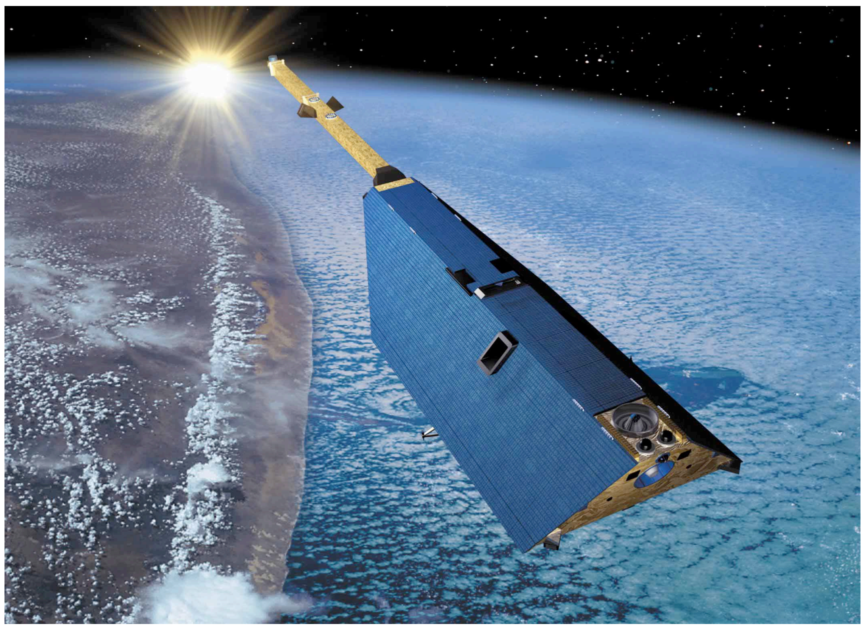

Figure 2.1 The CHAllenging Mini-Satellite Payload (CHAMP) (GFZ, 2011)

In order to assess the accuracy of experiments conducted in this study, reference or “truth” solutions provided by the Jet Propulsion Laboratory (JPL) are utilized. The reference solutions are produced using the GIPSY/OASIS II software. The data that are used consist of undifferenced dual-frequency pseudorange and carrier-phase measurements, which produce a position accuracy of less than one decimetre. The computational method consists of solving for a dynamic orbit solution by estimating global perturbing force parameters. The final solution is obtained with a reduced-dynamic filtering technique that estimates the remaining perturbing accelerations as a stochastic time series. The GPS precise orbits and clocks that are used in the generation of this solution are the JPL quick-look products. The output is the position and velocity of CHAMP at 1-minute intervals. (JPL Quick Orbits, 2008).

## 2.10 Dynamic Orbit Results

The following section describes experiments performed solely with the dynamic models, without the use of any GPS measurements. The dynamic models are initialized from and compared against the position and velocity obtained from the JPL reference reduced dynamic solution. Using the initial GPS-based state, the dynamic models are used to propagate the state in 1-minute intervals for a total of 30 minutes. Although the state produced at each epoch produces a position and velocity solution, only the accuracy of the position solution is assessed. Generally, an accurate position state indicates an accurate velocity as well. Hence, only the position state is compared with the reference solution in this section and others that follow.

The largest acceleration acting on the LEO arises from the geopotential, thus the degree and order of the gravitational model play a large role in the orbit determination process. The gravitational coefficients for the gravitational models were obtained from three separate sources, all yielding practically equal results. The three gravitational models compared in this study were the Joint Gravity Model (JGM-3) from TOPEX/POSEIDON (Tapley et al., 1996), the Gravity Recovery and Climate Experiment (GRACE) Gravity Model (GGM02) (Tapley et al., 2005) and the CHAMP Gravity Model (EIGEN) (Reigber et al., 2004). The currently employed model is EIGEN-CHAMP03S. Figure 2.2

shows a time-series of the 3D difference between the solution produced by the dynamic models and the JPL reference solution with varying degree and order values of the gravitational model. All solutions were produced by including perturbations due to the solar and lunar gravitational forces, solar radiation pressure and air drag. The degree and order of the Earth gravitational model were varied and the results were analyzed. As expected, the accuracy of the dynamic models increases as the degree and order of the gravitational model are increased. If one desires to obtain position accuracy to tens of metres, a 10x10 gravitational model will suffice. For applications where a higher accuracy is required, a 40x40 gravitational model is more suitable, since the amount of deviation from the true position after a 30-minute interval is less than a metre.

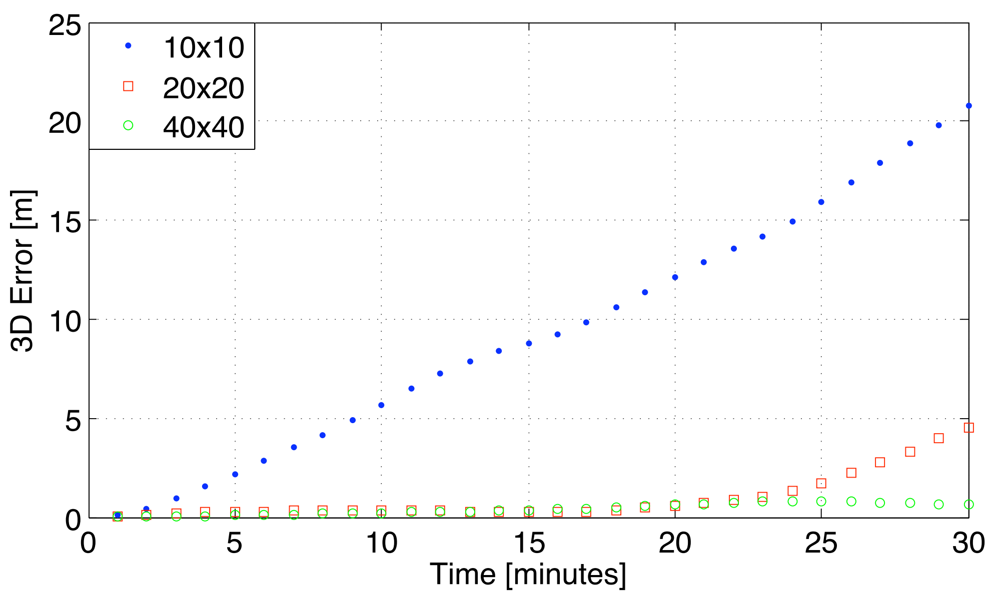


Figure 2.2 3D Error between reference solution and dynamic solution for various degree/order expansions

Figure 2.3 displays the same information, but the degree and order of the gravitational model have been increased. As the degree and order of the gravitational model increase, the improvements in the accuracy of the solution become less significant. The largest improvement in the accuracy of the solution is observed when transitioning from a 10x10 gravitational model to a 20x20 gravitational model and the smallest improvement is seen when going from an 80x80 gravitational model a 100x100 gravitational model. In the case of the 40x40 gravitational model, the solution diverges relatively quickly, but begins to converge to the reference solution as time goes on. This trend can be caused for many reasons including the LEOs position in the gravitational field. The 40x40 gravitational model may be less accurate in a certain location in the gravitational model and increase in accuracy as the LEO moves to through the gravitational field. If the time period was extended, the general trend will prevail where the 40x40 gravitational model will gradually diverge from the reference solution faster than the 60x60, 80x80 and 100x100 gravitational models, with similar results using the latter three models. Figure 2.4 gives the 3D difference between the solution obtained by the dynamic models at the end of a 5-minute and 30-minute period in form of a semi log graph. The error in the solution ranges from 2.2 m to 1.6 cm after 5 minutes and 21 m to 55 cm after 30 minutes. During the processing of GPS data for LEO POD, the length of a GPS data outage is typically less than a few minutes. Thus, if the utmost accuracy is required and a 100x100 gravitational model is used, the produced position solution should deviate less than about 2 cm from the true position if a GPS data outage occurs. Aside from naturally occurring data gaps, the effect on solution accuracy with manually inserted long data gaps that simulate receiver off-times is also assessed.

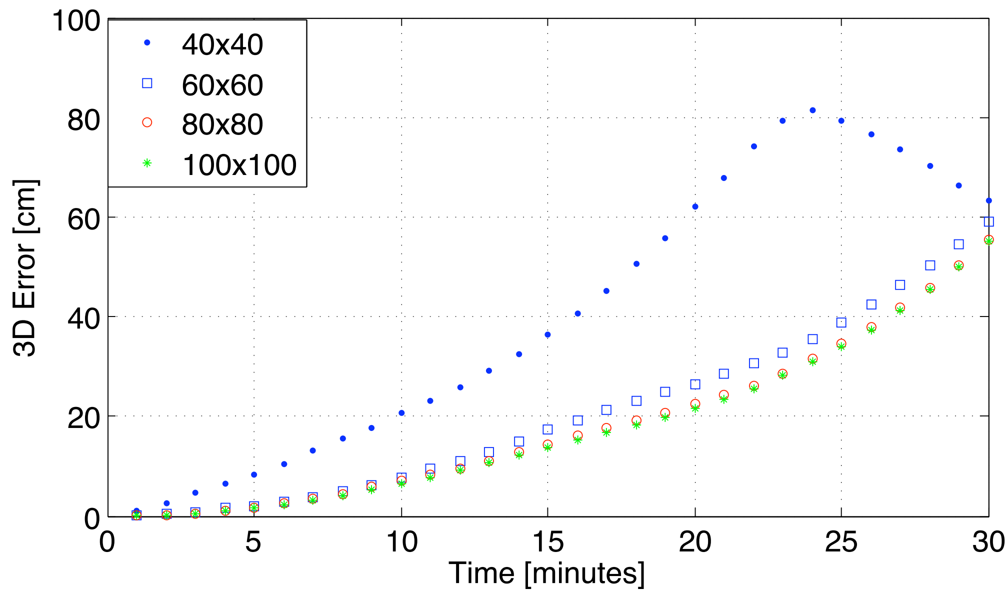


Figure 2.3 3D Error between reference solution and dynamic solution for various degree/order expansions

In terms of the results obtained in Figure 2.4, if a GPS data outage of 30 minutes occurs onboard a LEO, the solution can be maintained to an accuracy of 55 cm using only the dynamic models. This however is typically not the case in real-life scenarios. In order to maintain the accuracy of the reduced dynamic solution to this caliber, the initial state must be extremely accurate, as is the case with the reference solution from which the dynamic models were initialized in this case. The details of the reduced dynamic solution will be examined more closely in the following sections. In the reduced dynamic solution, the dynamic models are initialized from the filtered solution just before the GPS data outage, which is rarely exact. The offset between the true initial state and the filtered initial state will cause the dynamic solution to diverge faster from the actual orbit. Therefore, the rate of divergence of the dynamic solution does not only depend on the quality of the dynamic models, but the quality of the initial state assigned to the dynamic models as well.

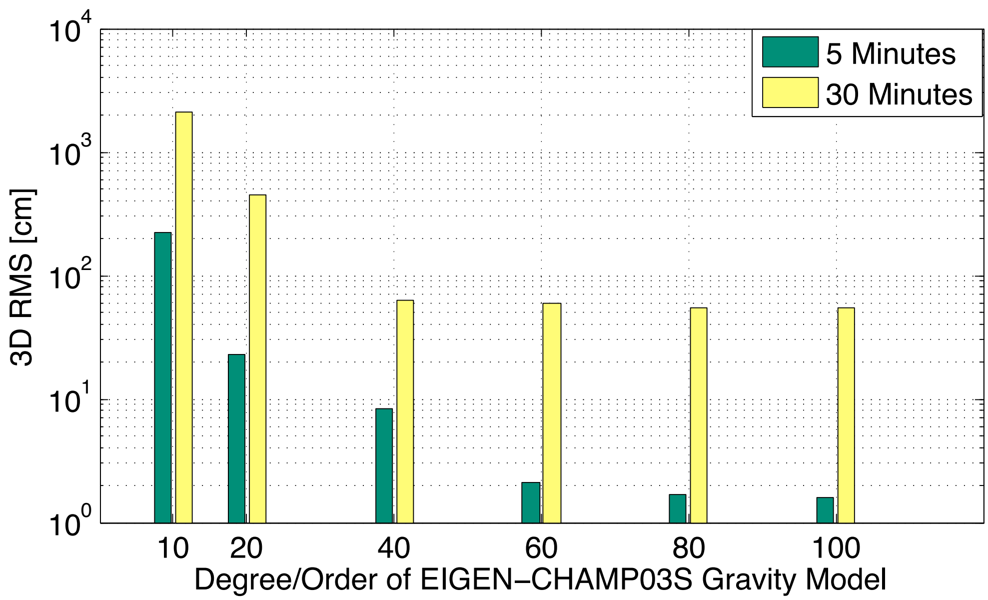


Figure 2.4 3D error of solution obtained from dynamic models for various degree/order expansions at end of a 5-minute and 30-minute period

The impact of the perturbations due to solar and lunar gravitational forces, solar radiation pressure and air drag is displayed in Figure 2.5, which is generated by first running a reference solution that contains a 100x100 gravitational model, solar and lunar gravitational forces, solar radiation pressure and air drag. Each of the perturbations is switched off and on, one-by-one, while maintaining a 100x100 gravitational model. By switching off a specific perturbation, its effect on the solution can be interpreted. Table 2.1 shows the difference in the solution for a 5-minute and 30-minute period. Since

CHAMP had a relativity low orbit of 454 km, it comes to no surprise that the air drag has a significant contribution to the total acceleration experienced by the satellite.

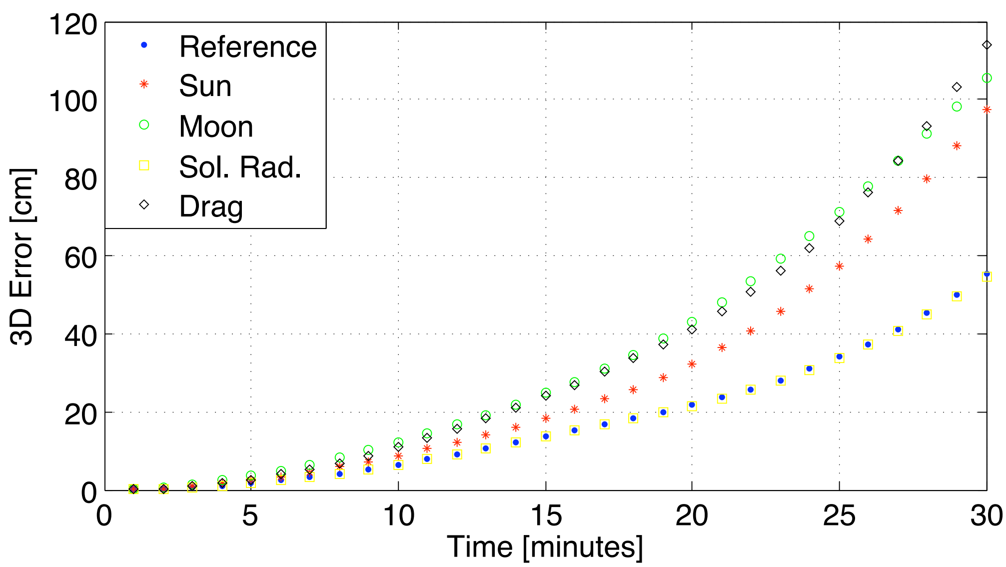


Figure 2.5 The effect of perturbations other than the geopotential

| Perturbation Neglected | 3D Difference after 5 Minutes | 3D Difference after 30 Minutes |
|---|---|---|
| Sun | 7.9 cm | 42 cm |
| Moon | 1.9 cm | 50 cm |
| Solar Radiation Pressure | 0.12 mm | 5.2 mm |
| Air Drag | 1.1 cm | 59 cm |

Table 2.1 Maximum 3D error from reference solution obtained from dynamic models for various perturbations

The results obtained for the 5-minute period and 30-minute period show different trends. After the 5-minute period, the gravitational force of the Sun tends to be the largest perturbation followed by the Moon, air drag and solar radiation pressure. One must also keep in mind that these results, especially for short intervals, depend heavily on the position of the LEO, as well as the geometry of the Earth, Sun and Moon. During this particular 5-minute period, it is possible that the LEO is closer to the Sun than the Moon, hence the reason for the larger perturbation by the Sun. Thus in order to accurately fill in the GPS data gaps during LEO POD with the dynamics, the accelerations caused by the Sun, Moon and air drag must be included. Solar radiation pressure plays a very small role in improving the accuracy of the position solution. In terms of the long data gaps that simulate receiver off-times, it would be more appropriate to observe the 3D difference of the position solution after a 30-minute period. Hence in terms of achieving good accuracy with dynamic models, modelling air drag is the most important, followed by the lunar gravitational force, solar gravitational force and solar radiation pressure. The effect of the solar radiation pressure is again extremely small and would only be required in applications where the requirements are high accuracy levels.

One very important aspect of the calculations involving the dynamic models is the processing power that is required. The integration methods involved in the propagation of the state are very complex and thus require relatively large amounts of processor time and much work has been done to explore methods for reducing the large burden on the processor (Erdogan and Karslioglu, 2009). Reducing the processor time is especially important in situations where the position of the LEO is required in real-time with limited computing power. It is therefore worthwhile to examine the processor time required for the various gravitational models. Figure 2.6 shows the processor times when varying the degree and order of the gravitational model with all other perturbations turned off, which was generated using MATLAB, for one step of processing. The integration of the dynamic models is performed using an executable file developed in C++ and is called from MATLAB using the appropriate UNIX commands. In this case, it is more important to observe the values relative to each other rather than the absolute value of each case. In accordance with theory, the processing time increases as the degree and order of the gravitational model is increased. Along with the actual data points, the least-squares fitted function is also plotted:

$$T = 0.00000983d^2 - 0.0000913d + 0.0231 \tag{2.22}$$

where $T$ is the processing time and $d$ is the degree and order of the gravitational model. The processing times increase in a quadratic manner as the degree and order of the gravitational model increase. Therefore, for 5 minutes of processing, the cumulative processing time would range from 1 s to 11 s for the 10x10 and 100x100 gravitational models, respectively. The cumulative processing time would range from 3 s to 19 s for the 10x10 and 100x100 gravitational model, respectively after 30 minutes of processing.

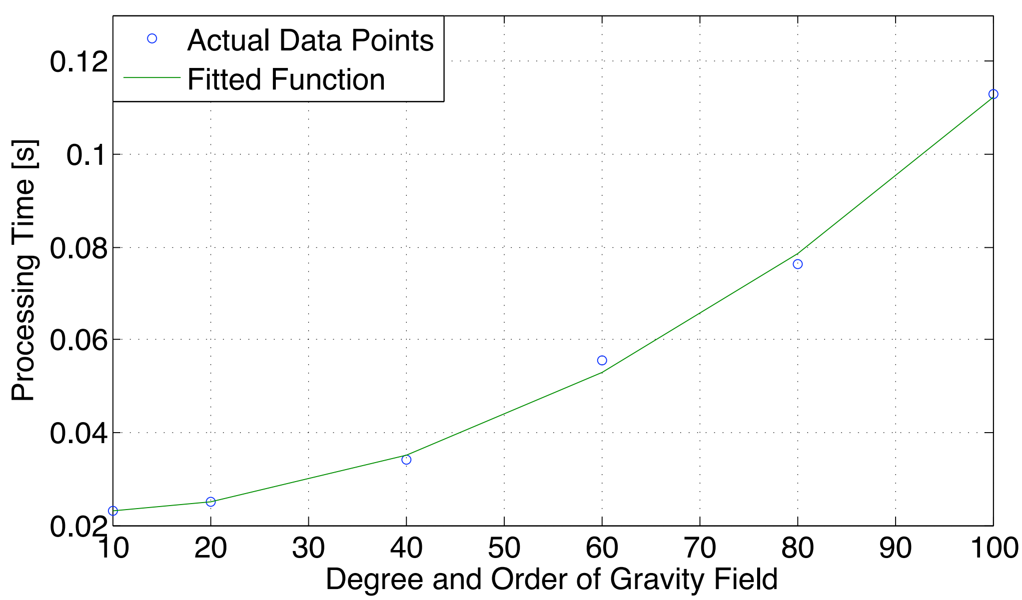


Figure 2.6 Sample processor times for various degree and order values of the gravity model

The obtained results for the dynamic models are in full agreement the current scientific standard, as verified by Montenbruck et al. (2005). A deviation of only 1.6 cm after 5-minutes and 55 cm after 30-minutes with a 100x100 gravitational model along with perturbations due to the Sun, Moon, solar radiation pressure is more than sufficient to meet the strict demands of LEO POD. Previous studies have shown that the utilization of these dynamic models plus empirical accelerations produce errors as small as 10 cm for CHAMP in the reduced dynamic formulation (Montenbruck et al., 2005). Thus, it is possible to achieve decimetre-level accuracy in the reduced dynamic solution with these dynamic models.

# Chapter 3

# 3 GPS Data Processing

This chapter begins with a discussion of the GPS measurement models used in this study. A more detailed description of the models can be found in textbooks such as Leick (2004) and Seeber (2003). A discussion of outlier and cycle slip detection techniques, in order to validate the quality of the measurements, is then presented. This chapter concludes with the kinematic-only orbit results produced by the GPS processor.

## 3.1 Single Point Positioning

The GPS single point positioning or the GPS navigation solution is obtained with the use of least-squares estimation. The purpose of least-squares estimation is to minimize the square of the difference between actual measurements and modelled observations. The most basic GPS solution is obtained with an epoch-by-epoch least-squares estimation in which each epoch is independent from all others. Neglecting smaller GPS errors, the observation equation is as follows (Grewal et al., 2007):

$$P = \sqrt{(X-x)^2 + (Y-y)^2 + (Z-z)^2} + c(dt_r - dt^s) \tag{3.1}$$

where

| | |
|---|---|
| $P$ | = Pseudorange |
| $(X, Y, Z)$ | = GPS satellite position coordinates |
| $(x, y, z)$ | = GPS receiver position coordinates |
| $c$ | = speed of light |
| $dt_r$ | = receiver clock offset |
| $dt^s$ | = GPS satellite clock offset |

The above observation equation is non-linear in the unknowns. In order to most efficiently solve the problem, the model can be linearized about the reference state $(x_0, y_0, z_0)$. The iterated least-squares solution is obtained from:

$$\boldsymbol{x} = \boldsymbol{x_0} + \boldsymbol{\delta} \tag{3.2}$$

where $\boldsymbol{x}$ is the state estimate, $\boldsymbol{x_0}$ is the a priori state estimate and

$$\boldsymbol{\delta} = (\boldsymbol{H^T H})^{-1}\boldsymbol{H^T w} \tag{3.3}$$

In the above equation, $H$ is the Jacobian that consists of the measurement partials and the misclosure $w$ is the difference between actual measurements and modelled observations:

$$\boldsymbol{H} = \begin{pmatrix} \frac{\partial P_1}{\partial x} & \frac{\partial P_1}{\partial y} & \frac{\partial P_1}{\partial z} & 1 \\ \frac{\partial P_2}{\partial x} & \frac{\partial P_2}{\partial y} & \frac{\partial P_2}{\partial z} & 1 \\ \cdots & \cdots & \cdots & \cdots \\ \frac{\partial P_n}{\partial x} & \frac{\partial P_n}{\partial y} & \frac{\partial P_n}{\partial z} & 1 \end{pmatrix} \tag{3.4}$$

$$\boldsymbol{w} = \begin{pmatrix} P_1 & - & \rho_{0_1} \\ P_2 & - & \rho_{0_2} \\ \dots & \dots & \dots \\ P_n & - & \rho_{0_n} \end{pmatrix} \tag{3.5}$$

where

$$\rho_0 = \sqrt{(X - x_0)^2 + (Y - y_0)^2 + (Z - z_0)^2} \tag{3.6}$$

The terms in the matrix *H* are known as the direction cosines:

$$\frac{\partial P}{\partial x} = \frac{(X - x_0)}{\sqrt{(X - x_0)^2 + (Y - y_0)^2 + (Z - z_0)^2}} \tag{3.7}$$

$$\frac{\partial P}{\partial y} = \frac{(Y - y_0)}{\sqrt{(X - x_0)^2 + (Y - y_0)^2 + (Z - z_0)^2}} \tag{3.8}$$

$$\frac{\partial P}{\partial z} = \frac{(Z - z_0)}{\sqrt{(X - x_0)^2 + (Y - y_0)^2 + (Z - z_0)^2}} \tag{3.9}$$

where (*X, Y, Z*) are the GPS satellite coordinates and ($x_0$, $y_0$, $z_0$) are the approximate receiver coordinates. The terms in the vector $\boldsymbol{w}$, *P* and $\rho_0$ represent the measured pseudorange and the modelled range, respectively.

The measurement residuals are calculated using the following formula:

$$\boldsymbol{r} = \boldsymbol{w} - \boldsymbol{H\delta} \tag{3.10}$$

## 3.2 Precise Point Positioning

Unmodelled errors and biases contribute a great deal to the loss of accuracy in standard GPS point positioning. The errors and biases present in the GPS measurements include ephemeris errors, residual satellite clock errors, multipath error and atmospheric effects. In the case of a LEO, the effect of the troposphere is disregarded, since the receiver onboard the LEO is above the troposphere, thus leaving ionospheric refraction as the only atmospheric error to be managed. The measurement error caused by the ionosphere is addressed by combining the L1 and L2 measurements to synthesize the ionosphere-free linear combination. In order to reduce the ephemeris errors, precise satellite ephemeris and clock data can be utilized. The precise orbit and clock products are generated by many institutions such as the International GNSS Service (IGS). The precise orbits have an rms error of about 2.5 cm in each spatial component (IGS, 2009). In order to achieve centimetre level accuracy, relative positioning is very effective and has widespread acceptance. In addition to collecting data with the receiver whose position is to be determined, the fact that simultaneous observations must also be made at reference stations poses significant limitations, especially in the case of a LEO. Thus, PPP provides an excellent alternative to relative GPS. PPP is the process of utilizing the undifferenced carrier-phase measurement along with the undifferenced pseudorange measurements, appropriately dealing with the errors and biases, and using precise orbits and clocks (Kouba and Héroux, 2001).

The precise orbits are available in 15-minute intervals. Therefore, in order to make use of the precise orbit information for intermediate measurements, the precise coordinates of the GPS satellites must be interpolated to the time of observation. There exist several interpolation techniques, but the one used in this study is the Chebyshev interpolation, due to its good accuracy and relatively simple implementation. The technique of

Chebyshev interpolation involves the use of Chebyshev polynomials. The Chebyshev polynomials are determined for 6-hour data arcs that provide an increase in accuracy. Once the Chebyshev polynomials have been determined, the GPS satellite coordinates can then be determined at the desired time (Sarra, 2006). The precise clock files contain GPS satellite clock offsets at a rate of every 30-seconds. The high frequency of precise clock information then does not require a high precision interpolator, unlike the precise orbits. In this study, the built-in MATLAB functions “polyfit” and “polyval” are utilized for the interpolation. (MathWorks, 2011).

When post-processing the data, one additional method of improving the accuracy of the state is by smoothing the data. The data are initially processed in the order in which they appear in the RINEX format file, while the processor saves the state and covariance information for the forward run. Once the end of the file is reached, the data are fed backwards into the processor, starting with the latest observation. The state and covariance information for the forward and backward run is then combined, producing a more accurate state with a lower covariance (NRCan, 2007).

## 3.3 GPS Measurement Models for Determination of LEO Orbits

This section contains a discussion on the basic observation equation where all the error sources are introduced. Each error source is then described in more detail with an indication of its implementation in the GPS processor.

### 3.3.1 Basic Observation Equation

The GPS receiver is able to make pseudorange (code-based) measurements, as well as phase (carrier-phase-based) measurements. The observation model for the code measurement $P$ taken onboard the LEO is as follows (Kouba and Héroux, 2001):

$$P = \rho + c(dt_r - dt^s) + \Delta\rho_{rel} + \Delta\rho_{ion} + \Delta\rho_{gps\_ant} + \Delta\rho_{LEO\_ant} + \Delta\rho_{CodeMP} + e \quad (3.11)$$

where

$\rho$ = geometric range between GPS satellite and receiver

$c(dt_r - dt^s)$ = range error due to difference between receiver clock offset and GPS satellite clock offset

$\Delta\rho_{rel}$ = relativistic error

$\Delta\rho_{ion}$ = ionospheric refraction

$\Delta\rho_{gps\_ant}$ = GPS satellite antenna phase centre offset

$\Delta\rho_{LEO\_ant}$ = LEO GPS antenna phase centre offset

$\Delta\rho_{CodeMP}$ = code multipath

$e$ = code measurement noise

The observation equation for the phase measurement $\phi$ is slightly different:

$$\phi = \rho + c(dt_r - dt^s) + \Delta\rho_{rel} + \Delta\rho_{ion} + \Delta\rho_{gps\_ant} + \Delta\rho_{LEO\_ant} + \Delta\rho_{windup} + \Delta\rho_{PhaseMP} + N\lambda + \varepsilon \tag{3.12}$$

where

$\Delta\rho_{windup}$ = phase windup

$\Delta\rho_{PhaseMP}$ = phase multipath

$N\lambda$ = phase integer ambiguity scaled by phase wavelength

$\varepsilon$ = phase measurement noise

### 3.3.2 Ionosphere-Free Linear Combination

The use of various linear combinations of the GPS measurements is useful in eliminating the effect of the ionosphere and detecting outliers. When a dual-frequency receiver is utilized, the code and carrier-phase measurements can be combined to form linear combinations using the following general formulae (Leick, 2004):

$$P_{mn} = mP_1 + nP_2 \tag{3.13}$$

$$L_{mn} = mL_1 + nL_2 \tag{3.14}$$

where $P_{mn}$ and $L_{mn}$ are the code and carrier-phase linear combinations, respectively. $P_1$ and $P_2$ represent the code measurements from the L1 and L2 frequencies and $L_1$ and $L_2$ represent the carrier-phase measurements from the L1 and L2 frequencies. When measurements from both the L1 and L2 frequencies are available, the following ionosphere-free linear combination can be formed for the code and carrier phase in units of distance:

$$P_{IF} = \frac{f_1^2 P_1 - f_2^2 P_2}{f_1^2 - f_2^2} \tag{3.15}$$

$$L_{IF} = \frac{f_1^2 L_1 \lambda_1 - f_2^2 L_2 \lambda_2}{f_1^2 - f_2^2} \tag{3.16}$$

where $f_1$ = 1575.42 MHz and $f_2$ = 1227.60 MHz are the frequencies of the L1 and L2 signals, respectively, and $\lambda_1$ = 19.0 cm and $\lambda_2$ = 24.4 cm are the wavelengths of the L1 and L2 signals, respectively. The ionosphere-free linear combination of the measurements is used in the processing when the data from both frequencies are available.

### 3.3.3 Ionospheric Delay

The model used to correct for the ionospheric refraction depends on whether the GPS receiver is a single-frequency or dual-frequency receiver. A very simple and elegant linear combination is used for dual-frequency receivers (Leick, 2004):

$$P_{IF} = \frac{f_1^2}{f_1^2 - f_2^2} P_1 - \frac{f_2^2}{f_1^2 - f_2^2} P_2 \tag{3.17}$$

for the pseudorange measurements and

$$\phi_{IF} = \frac{f_1^2}{f_1^2 - f_2^2} \phi_1 - \frac{f_2^2}{f_1^2 - f_2^2} \phi_2 \tag{3.18}$$

for the carrier-phase measurements where $\phi_1$ and $\phi_2$are in units of length and $f_1$ and $f_2$ represent the frequencies for the L1 and L2 signals, respectively.

Although there exist many methods to correct for the ionosphere effect, such as ionosphere modelling and parameter estimation a method called GRoup And PHase Ionospheric Correction (GRAPHIC) is best suited for single-frequency, spaceborne receivers (Bock et al., 2008). GRAPHIC utilizes an ionosphere-free linear combination formed by the $P_1$-code and L1 phase observations that eliminates the first order error caused by the ionosphere:

$$P_{GRAPHIC} = {(P_1 + \ \phi_1)}/{2} \tag{3.19}$$

Since the ionosphere delays the code signal but advances the carrier-phase, the GRAPHIC linear combination eliminates the ionospheric error term, but introduces an unknown ambiguity (Montenbruck, 2003):

$$\begin{aligned} P_{GRAPHIC} = \ & \rho + c(dt_r - \ dt^s) + \ \Delta\rho_{rel} \ + \ \Delta\rho_{gps\_ant} \\ & + \Delta\rho_{LEO\_ant} \ + \ \Delta\rho_{CodeMP} + \ N_{IF}\lambda + \ e \end{aligned} \tag{3.20}$$

### 3.3.4 Sagnac Effect

The Sagnac effect results from the rotation of the Earth during the period between the times of transmission of the GPS signal from the GPS satellite to the reception of the signal by the receiver. Once determined, the Sagnac effect is added to the pseudorange and the carrier-phase, which is typically between 0 and 10 metres. (Ashby, 2007).

### 3.3.5 Relativistic Effect

The relativistic effect arises from the fact that clocks run at different speeds when undergoing different gravitational potentials. The clocks in the GPS satellite are running at a faster rate than the clock in the receiver. The position and velocity of the GPS satellite are used to determine a relativistic correction to the pseudorange and the carrier-phase measurements, which ranges between 0 and 10 metres. (Ashby, 2007).

### 3.3.6 Phase Windup

The signals broadcast by the GPS satellites are circularly polarized. Thus the relative orientation of the transmission and receiver antennas is important. Phase windup is an effect that arises from the relative orientation change of a GPS satellite's antenna with respect to a receiver's antenna. The effect of phase windup is modelled as an angle between effective dipoles of receiver and satellite antennas. Once calculated, the phase windup correction is used to correct for the carrier-phase measurements, which is typically between 0 and 5 cm. (Kouba and Héroux, 2001).

### 3.3.7 GPS Satellite Antenna Phase Centre Offset

The IGS precise orbit products give the coordinates of the GPS satellites to the centre of mass. The GPS signal however, originates from the GPS antenna phase centre and thus the offset between the centre of mass and antenna phase centre needs to be taken into account. The values given in the ANTEX file describe the conventional components of the vector between the satellite centre of mass and the phase centre of the antenna in the satellite reference frame (along, across and radial) (Kouba, 2003).

### 3.3.8 LEO GPS Receiver Phase Centre Offset

The orbit integration equations are solved for in the celestial reference system, which means that the coordinates of the LEO are given to the centre of mass of the satellite. The coordinates calculated from the GPS measurements are calculated in the terrestrial reference system to the phase centre of the GPS antenna. Thus in addition to a coordinate transformation between the two reference systems, the antenna offset from the centre of mass must also be dealt with. The antenna offset for CHAMP in the spacecraft coordinate system is (-1488.0 mm, 0.0 mm, -392.8 mm) (JPL Quick Orbits, 2008).

The offset corresponds to a 3D difference vector of magnitude 1.5388 m. There are two methods to account for the antenna offset. One method is to transform the LEO position coordinates into the spacecraft coordinate system and subtract each component individually (Hwang et al., 2008). The other method is to subtract the 3D antenna displacement vector from the 3D displacement error vector when comparing the calculated solution to the reference solution. The latter approach is used in this study. More explicitly, the antenna offset is accounted for with the use of the following formula:

$$E = \sqrt{(X_{cal} - X_{true})^2 + (Y_{cal} - Y_{true})^2 + (Z_{cal} - Z_{true})^2} - 1.5388 \quad (3.21)$$

where $E$ is the 3D difference between the calculated and reference solution, both to the centre of mass.

This method for the LEO lever arm correction is approximate and does not account for the attitude of the LEO. The exact method of determining the lever arm correction involves the use of CHAMP attitude information in quaternion form. Unfortunately, these data were not available. Nonetheless, the method used in this study is accurate enough to provide reliable results from the experiments.

## 3.4 Measurement Quality Control and Outlier Detection

The undifferenced GPS measurements are processed in a recursive manner that verifies the quality of the measurements and rejects any outliers. The pre-process screening of the measurements is conducted individually for each satellite. First, a basic screening is conducted to detect any large outliers. Then the narrow-lane and wide-lane linear combinations are analyzed in order to ensure absence of cycle slips. The code and phase ionosphere-free linear combinations are then screened to verify the quality of the measurements. If the measurements pass through the initial screening, they are used in the determination of the receiver state. Once the state for the current epoch has been computed, the measurement residuals for each satellite are computed. Any satellite exhibiting a large residual, or a large difference between the modelled and actual measurement, is removed and the epoch is processed once again. In addition to the post-process screening of the residuals, the position dilution of precision (PDOP) is also computed. If the PDOP is above an empirically set cutoff value, the state of the current epoch is considered unreliable and thus not used. The residual and PDOP cutoff values are given in Appendix A.

### 3.4.1 Data Screening

The quality of each measurement is assessed before it is used in the positioning algorithm with the use of the narrow-lane and wide-lane linear combinations. The narrow-lane linear combination for the carrier-phase in units of distance is synthesized in order to detect any cycle slips in the carrier-phase measurements (Leick, 2004):

$$L_{NL} = L_2\lambda_2 - L_1\lambda_1 \tag{3.22}$$

The value of the narrow-lane linear combination is compared with the value of the narrow-lane linear combination from the previous epoch of the same satellite. If the difference between the narrow-lane linear combination from the current epoch and the previous epoch is within 20 cm, then the measurement is considered reliable (NRCan, 2007). In a similar fashion, the wide-lane linear combination is constructed for both the code and the carrier-phase measurements. The usefulness of the wide-lane linear combination arises from the fact that this particular linear combination eliminates the effects of the ionosphere, geometry and the clocks. The code wide-lane linear combination is expressed as:

$$P_{WL} = \frac{P_1 + P_2}{2} \tag{3.23}$$

The carrier-phase wide-lane linear combination in units of distance is expressed as:

$$L_{WL} = (L_1 + L_2)\frac{c}{f_1 - f_2} \tag{3.24}$$

By subtracting the code wide-lane linear combination from the carrier-phase wide-lane linear combination, ones arrives at the following equation:

$$L_{WL} = (L_1 + L_2)\frac{c}{f_1 - f_2} - \frac{P_1 + P_2}{2} \tag{3.25}$$

which is expressed in units of distance. This wide-lane linear combination of the current epoch is compared with the wide-lane linear combination from the previous epoch for the same satellite. If the difference between current epoch and previous epoch values is larger than 3 m, the measurement is considered unreliable (NRCan, 2007).

### 3.4.2 Pseudorange Smoothing

Once the outliers have been detected and discarded, by empirical means, the pseudorange code measurements can be filtered with the use of the carrier-phase measurements. The purpose of "pseudorange smoothing", or the "carrier-phase smoothed pseudorange method" is to filter out the pseudorange noise over a time period. The carrier-phase allows the filtering of the pseudoranges by averaging the point-by-point difference between the continuous phase measurements, which are precise but biased, and the pseudorange measurements that are noisy but absolute. The averaged phase-pseudorange is then added back to the phase point to produce an absolute pseudorange measurement that is now more precise. Let $P_i$ be the pseudorange measurement at time $i$. Also, let $\Delta\phi$ be the delta range measurement between times $i$ and $i$+1 obtained from the continuous carrier-phase measurements. The smoothed pseudorange at time $i$+1 is then obtained from (Wang and Gao, 2008):

$$P_{i+1} = \frac{i}{i+1}(P_i + \Delta\phi_{i+1}) + \frac{1}{i+1}P_{i+1} \tag{3.26}$$

This equation is nothing more than a simple average of the current pseudorange value with the previously averaged pseudorange value that has been propagated forward with the current delta range measurement.

## 3.5 Kinematic Orbit Results

A sequential least-squares approach is utilized in the determination of the GPS solution in this study. In the sequential least-squares approach, the covariance information of the GPS solution is carried forward, thus producing a more accurate and reliable solution as compared to the epoch-by-epoch least-squares approach. The covariance matrix that is carried forward contains the uncertainty information about the three position components, as well as the receiver clock bias. The utilization of the sequential least-squares approach provides the ability to determine the float ambiguities associated with the carrier-phase measurements. A more in depth discussion on the sequential least-squares technique can be found in Kouba and Héroux (2001).

The results for the 3D rms error for the 7 days are displayed in Figure 3.1 along with the associated summary statistics in Table 3.1. These results were generated by using the JPL orbit solution as the reference solution, as discussed in Section 2.9. The results in Figure 3.1 are for the smoothed solution utilizing only the GPS measurements without any dynamical aiding. In order to ensure that the statistics are not affected by the converging period that manifests during the beginning and ending of the data arc, the error values for first and last 20 minutes of the data arc are not considered in the determination of the daily rms. The mean 3D rms error for the 7 days daily solution is 29 cm, with a standard deviation of the error of 4.6 cm. Since these results are processed without the use of any dynamical information, the accuracy of the solution is completely dependent on the quality of the measurements. Although all effort has been made to eliminate any outlying measurements, there still exist inaccurate measurements that are not filtered and therefore degrade the accuracy of the solution, which can be fixed if the outlier detection algorithms are improved. Since a solution is not calculated if there are not enough GPS data available, approximately 20% of the epochs for each day do not contain a solution.

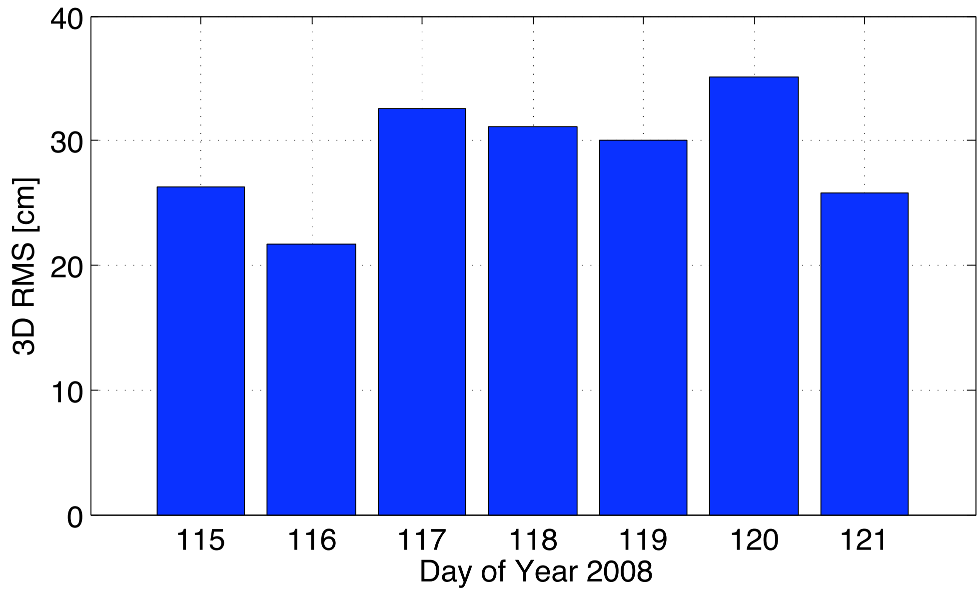


Figure 3.1 3D rms of 24-hour intervals for days 115 – 121 of year 2008 by post-processing dual-frequency data using only GPS measurements

| Mean | Std. Dev. | Maximum | Minimum |
|---|---|---|---|
| 29 cm | 4.6 cm | 35 cm | 22 cm |

Table 3.1 Summary statistics of 3D rms of 24-hour intervals for days 115 – 121 of year 2008 by post-processing dual-frequency data using only GPS measurements

A plot displaying the 3D difference between the smoothed solution with respect to time for the 119$^{th}$ day of the year 2008 is displayed in Figure 3.2. The solution is computed every 10 seconds, but the reference solution is available in intervals of 60 seconds. Thus the computed solution is compared with the reference solution at 60-second intervals. The reason for choosing the 119$^{th}$ day of the year is because the 119$^{th}$ day is in closest agreement with the mean value for the 7 days, therefore providing a reliable sample for a typical solution. The range of the 3D error is less than 3 metres, with the bulk of the solutions to within $\pm$0.5 m. The solution error appears to be close to white noise, with perhaps some systematic errors arising from imperfections in the modelling of the GPS errors. There are certain time intervals in which the solution becomes significantly degraded, thus driving the daily rms higher. The degradation in accuracy that is observed around the 7 hour, 15 hour, 17 hour and 22 hour mark is for the most part caused by inaccurate measurements that are not filtered. In addition, undesirable GPS satellite geometry also contributes to the degradation in solution accuracy.

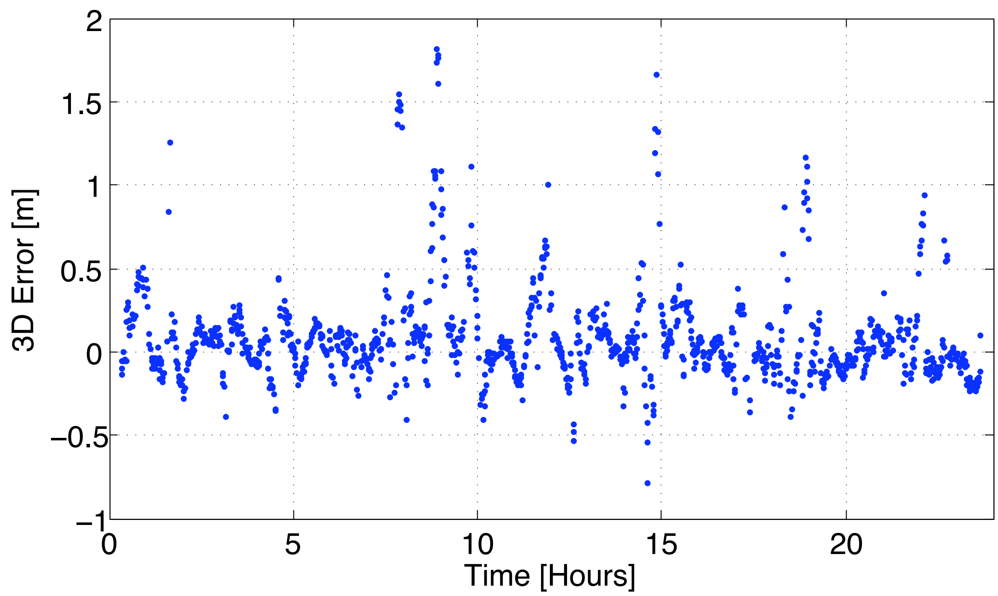


Figure 3.2 Time series of 3D error of a 24-hour interval for 119th day of year 2008 by post-processing dual-frequency data using only GPS measurements compared at 60-second intervals

In order to determine whether or not the produced kinematic solution is accurate, the online CSRS-PPP (Canadian Spatial Reference System-Precise Point Positioning) Service by Natural Resources Canada (NRCan) was utilized for comparison. NRCan's online PPP service produces a solution for a given RINEX file using only the GPS measurements without applying any dynamic modelling. A time series of the 3D difference between the NRCan solution and the JPL solution for the 119th day of 2008 is displayed in Figure 3.3. The major differences between the calculated solution and the one produced by NRCan when comparing to the reference JPL solution is that the NRCan solution contains more gaps and outliers. The reason for the large solution gaps and outliers is because the online PPP service by NRCan is designed primarily for terrestrial receivers. The service does include the error correction models required by LEOs. Nonetheless, this comparison still gives a good indication that the solution produced by the processor used in this study provides a fairly accurate solution, when using only the GPS measurements without any dynamic modelling. Dynamic modelling consists of using the force models whereas kinematic modelling consists of using only the GPS measurements without any force models.

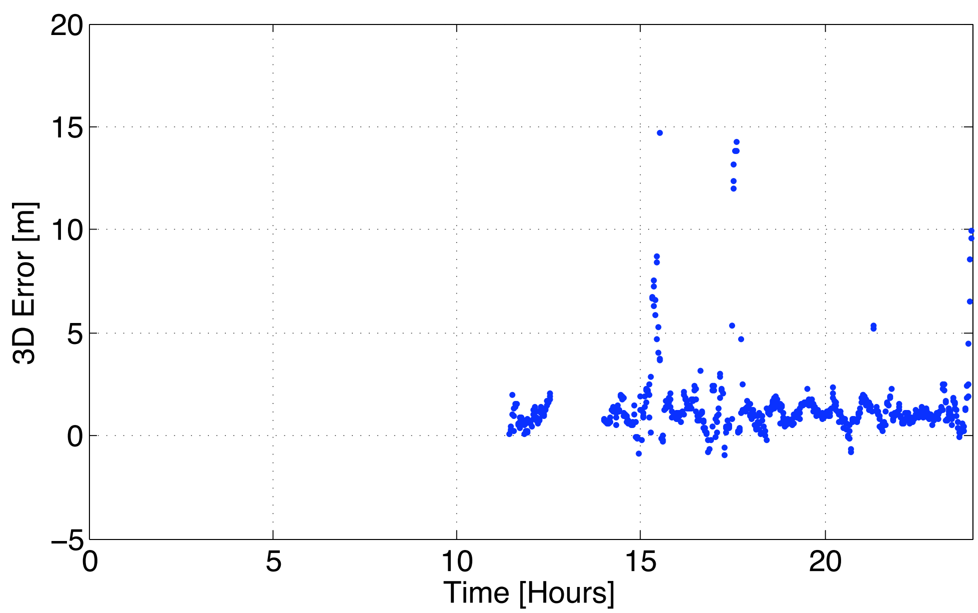


Figure 3.3 Time series of the 3D difference between solutions produced by JPL and NRCan for a 24-hour interval for 119th day of year 2008 comparing at 60-second intervals

An internal method of assessing the accuracy of the GPS solution is by analyzing the dilution of precision. The position dilution of precision, also known as PDOP, is calculated using the following equation (Langley, 1999):

$$PDOP = \sqrt{\sigma_x^2 + \sigma_y^2 + \sigma_z^2} \tag{3.27}$$

where $\sigma_x^2$, $\sigma_y^2$ and $\sigma_z^2$ are the variances of the three components of the Cartesian coordinate system obtained from the design matrix from an epoch-by-epoch solution. Figure 3.4 shows the PDOP and the number of tracked GPS satellites for day 119 of year 2008 for a period of 24 hours. Although the solution is computed every 10 seconds, Figure 3.4 shows the PDOP and number of tracked GPS satellites sampled at 60-second intervals, after the data has been filtered through quality control. Due to the unprocessed epochs, the gaps in the PDOP and number of tracked GPS satellites are quite apparent in Figure 3.4. The number of tracked GPS satellites ranges between 5 and 10. In order to ensure only the best quality data are used, any epoch with fewer than 5 observed satellites is discarded and not processed, which was determined empirically. Thus the results in Figure 3.4 represent the filtered results for epochs with 5 or greater tracked GPS satellites. Although it is possible to calculate the position of the receiver with only 4 tracked GPS satellites, the weak geometry causes large degradations in solution accuracy. The average number of tracked GPS satellites is 8. With a close look at Figure 3.4, one concludes, as is expected, that as the number of tracked GPS satellites drops, the PDOP increases.

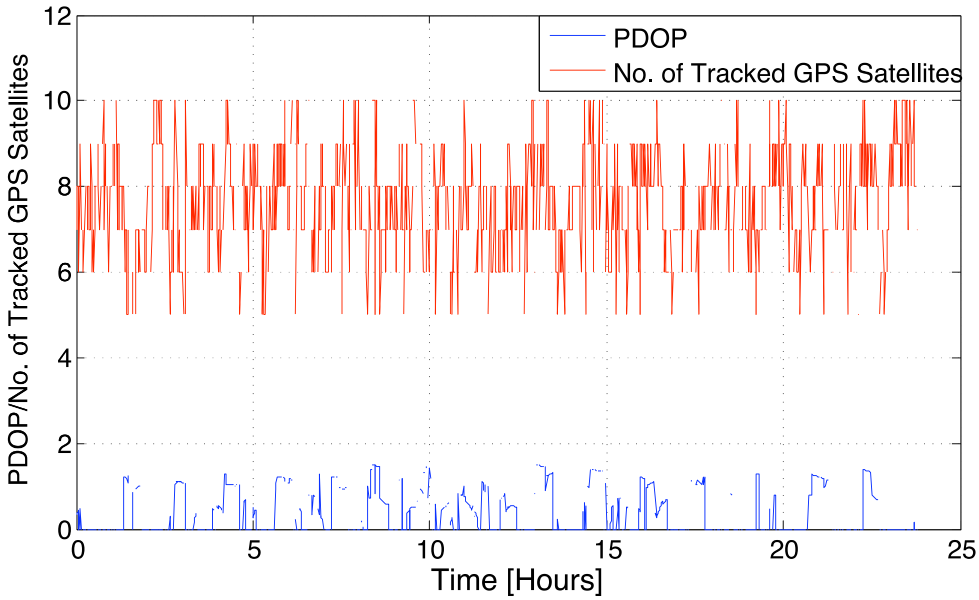


Figure 3.4 PDOP and number of tracked GPS satellites for a 24-hour interval for 119th day of year 2008 by post-processing dual-frequency data using only GPS measurements at 60-second intervals

In the least-squares formulation, the receiver clock bias is also estimated along with the position. Figure 3.5 shows the CHAMP receiver clock bias for the 119th day of the year 2008. The residuals of the undifferenced pseudorange and carrier-phase measurements are shown in Figure 3.6 and Figure 3.7, respectively. The figures consist of the measurement residuals calculated during the backward run after smoothing for all used satellites observed on day 119 of the year 2008. Once the state for the current epoch is computed, any satellites yielding large residual values for the pseudorange or carrier-phase measurements are rejected and the state for the current epoch is re-computed. The cutoff residual values, which were chosen empirically, for the pseudorange and carrier-phase measurements are chosen to be 4.47 m and 4.6 cm, respectively (NRCan, 2007). These cutoff values are in line with the fact that the carrier-phase measurements are about two orders of magnitude more precise than the pseudorange measurements.

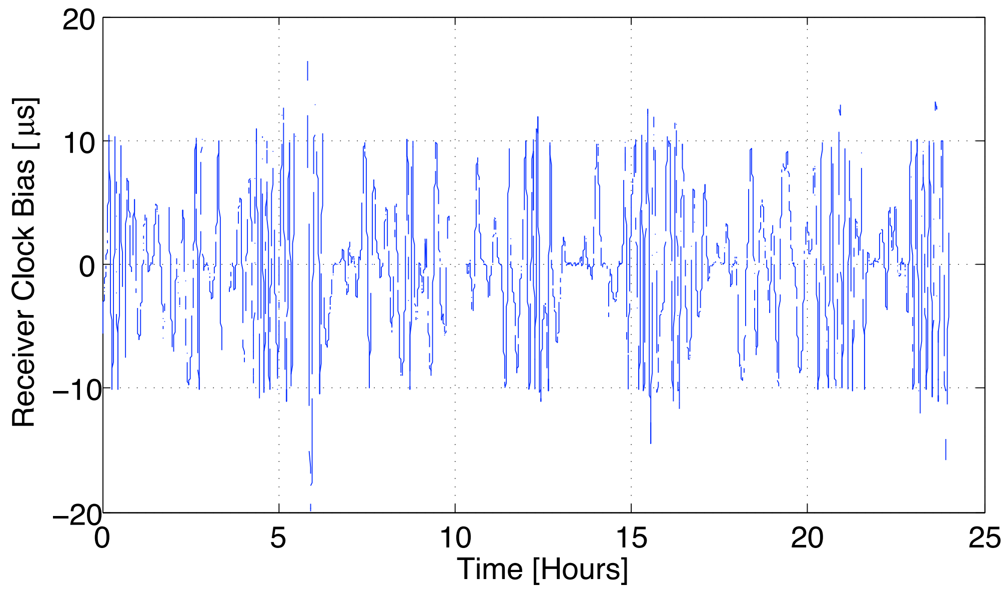


Figure 3.5 CHAMP receiver clock bias for a 24-hour interval for 119$^{th}$ day of year 2008 by post-processing dual-frequency data using only GPS measurements

For the pseudorange measurement residuals, there exists an offset of 11 cm from zero with an rms of 67 cm. For the carrier-phase measurement residuals, there exists practically no offset from zero with an rms of 1.0 cm. These are reasonable results, as confirmed by Jaggi et al. (2007). The fact that the carrier-phase residuals are two orders of magnitude smaller than pseudorange residuals and the fact that the pseudorange residuals are offset from zero is expected, since the noisy pseudorange measurements may carry some bias with them, unlike the carrier-phase measurements (Jaggi et al., 2007).

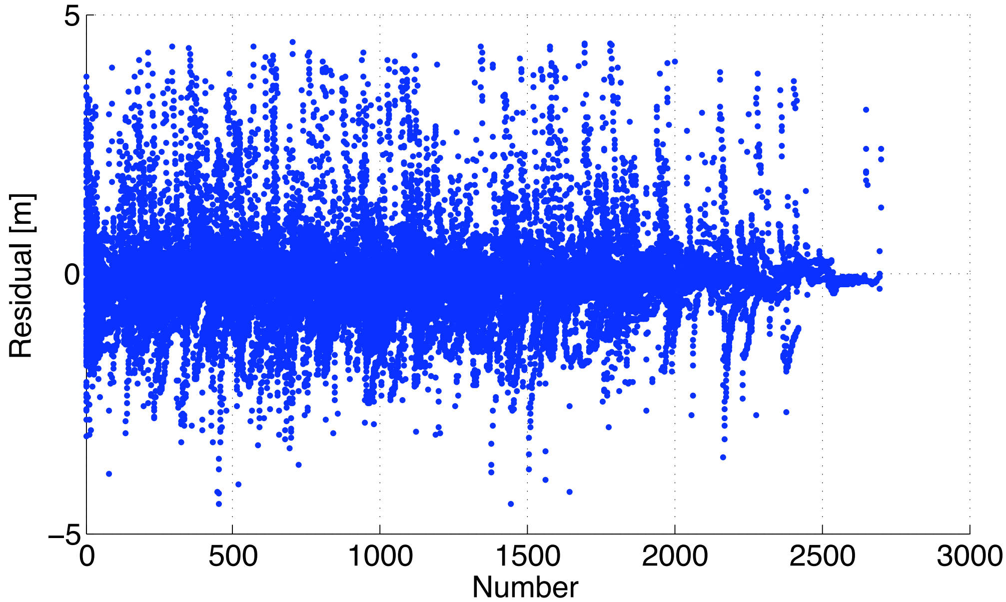


Figure 3.6 Pseudorange measurement residuals for a 24-hour interval for 119$^{th}$ day of year 2008 by post-processing dual-frequency data using only GPS measurements

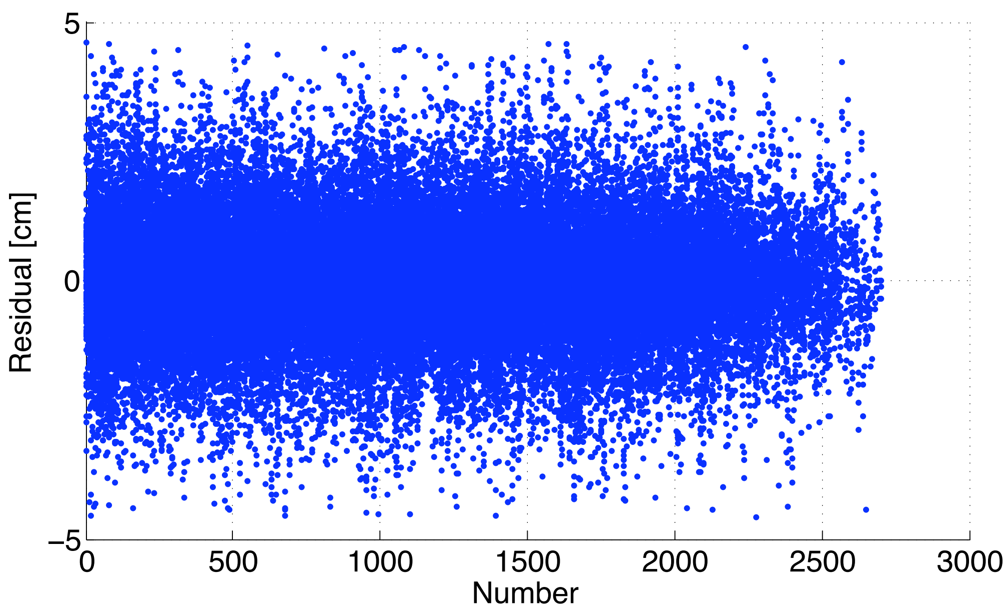


Figure 3.7 Carrier-phase measurement residuals for a 24-hour interval for 119$^{th}$ day of year 2008 by post-processing dual-frequency data using only GPS measurements

When utilizing the reduced dynamic technique, orbits accurate to 3D rms of 10 cm have been demonstrated, such as in Montenbruck et al. (2005). Since the dynamics are not available to aid the GPS measurements in the kinematic-only orbit, it is expected that the results will be inferior in the kinematic-only orbit as compared to the reduced dynamic orbit. A 3D rms error value of 29 cm is therefore accurate in the kinematic-only orbit.

# Chapter 4

## 4 Reduced Dynamic Orbit

There exist many limitations to kinematic tracking, including the fact that its performance is heavily dependent on GPS satellite geometry when the measurements are recorded. If there is a loss of signal by the receiver, the solution quickly degrades and if there is not enough information available, a solution cannot be produced at all. Introducing the dynamic models compensates for the degradations in accuracy or the complete unavailability of a solution. The dynamic models can be appropriately weighted, as prescribed by their quality, and the kinematic solution can thus be preserved. The dynamics thus aid in maintaining an accurate solution through geometric weak spots in addition to providing more stability throughout. The reduced dynamic technique, developed by Yunck et al. (1990) uses the dynamic formulation and utilizes the kinematic component with the use of a process noise describing the quality of the force models. Thus, by adjusting the parameters in the process noise, the orbit solution can range from fully dynamic to fully kinematic. The idea is to carefully tune the parameters in the process noise so that the solution is fully optimized to produce the most accurate solution. The reduced dynamic technique uses the Kalman filter in its formulation. This chapter discusses the implementation and results of the reduced dynamic orbit, beginning with a discussion of the theoretical background of the Extended Kalman Filter (EKF). The significance of the process and measurement noise matrices is then discussed. This chapter also provides a discussion on the tuning of the EKF and concludes with the results of the reduced dynamic orbit.

## 4.1 Extended Kalman Filter

Measurements collected by the GPS receiver in a LEO are typically noisier than the measurements collected by a GPS receiver on the ground, due to the high speed of the LEO and the rapidly changing GPS satellite constellation that the receiver faces. Therefore, relying solely on GPS measurements to determine the orbit of a LEO can prove to be quite challenging. The dynamic models for the LEO utilize the position and velocity of the LEO to determine the force that the LEO experiences. The dynamic models then allow the processor to propagate the position and velocity state forward, aiding the GPS solution. The GPS measurements and the dynamic information are combined via an EKF.

The first part of the EKF, known as the time update propagates the previous estimate $\boldsymbol{x}_{i-1}^{+}$ from $t_{i-1}$ to $t_i$ along with the associated covariance matrix $P_i^-$ (Yamaguchi and Tanaka, 2006):

$$\boldsymbol{x}_i^- = \boldsymbol{x}_{i-1}^{+} + \int_{t_{k-1}}^{t_k} \boldsymbol{f}(\boldsymbol{x}, t)dt \tag{4.1}$$

$$\boldsymbol{P}_i^- = \boldsymbol{\phi}_i \boldsymbol{P}_{i-1}^{+} \boldsymbol{\phi}_i^T + \boldsymbol{Q}_i \tag{4.2}$$

where

$\boldsymbol{x}_i^-$ = predicted a priori state vector

$\boldsymbol{x}_{i-1}^+$ = state estimate from previous epoch

$\boldsymbol{f}(\boldsymbol{x},t)$ = force model to propagate state

$\boldsymbol{P}_i^-$ = propagated covariance matrix

$\boldsymbol{\phi}_i$ = state transition matrix

$\boldsymbol{P}_{i-1}^+$ = covariance associated with state $\boldsymbol{x}_{i-1}^+$

$\boldsymbol{Q}_i$ = process noise matrix

The state vector that is utilized in this study is as follows:

$$\boldsymbol{x} = (\boldsymbol{r}; \boldsymbol{v}; \delta; \boldsymbol{A}) \tag{4.3}$$

where $\boldsymbol{x}$ is the state vector, $\boldsymbol{r}$ is the position vector, $\boldsymbol{v}$ is the velocity vector, $\delta$ is the GPS receiver clock bias and $\boldsymbol{A}$ is the ambiguity estimates vector corresponding to the carrier-phase measurements. The differential equation for the state transition matrix is (Erdogan and Karsioglu, 2009):

$$\frac{d}{dt}\boldsymbol{\phi}(t_{\boldsymbol{k}}, t_{\boldsymbol{k}-1}) = \frac{\partial \boldsymbol{f}(\boldsymbol{x}(t_k), t_k)}{\partial \boldsymbol{x}(t_k)}\boldsymbol{\phi}(t_{\boldsymbol{k}}, t_{\boldsymbol{k}-1}) \tag{4.4}$$

In this case, $\boldsymbol{\phi}(t_{\boldsymbol{k}}, t_{\boldsymbol{k}-1})$ represents the state transition matrix required to propagate a state from time $t_{\boldsymbol{k}-1}$ to $t_{\boldsymbol{k}}$.

The next step of the EKF is the measurement update:

$$\boldsymbol{K}_i = \boldsymbol{P}_i^- \boldsymbol{G}_i^T (\boldsymbol{W}_i^{-1} + \boldsymbol{G}_i \boldsymbol{P}_i^- \boldsymbol{G}_i^T)^{-1} \tag{4.5}$$

$$\boldsymbol{x}_i^+ = \boldsymbol{x}_i^- + \boldsymbol{K}_i (z_i - g_i(x_i^-)) \tag{4.6}$$

$$\boldsymbol{P}_i^+ = (\boldsymbol{I} - \boldsymbol{K}_i \boldsymbol{G}_i)\, \boldsymbol{P}_i^- \tag{4.7}$$

where

$\boldsymbol{K}_i$ = Kalman gain

$\boldsymbol{G}_i$ = Jacobian of partial derivatives of modelled observations w.r.t. state vector

$\boldsymbol{W}_i$ = measurement noise matrix

$z_i$ = (actual) observations vector

$g_i(x_i^-)$ = observations vector predicted from propagation of state vector

The EKF steps are summarized in Figure 4.1 (Montenbruck and Ramos-Bosch, 2007). The use of the EKF over the traditional Kalman filter eliminates any restrictions associated with sequential estimation. When applying the basic Kalman filter, the deviations between the reference state and the estimated state must be small enough to neglect any non-linearities in the dynamic and measurement models. The EKF overcomes this restriction by resetting the reference state to the estimated state at the start of each epoch. Basically, the EKF is the nonlinear version of the Kalman Filter that linearizes about the current mean and covariance (Brown and Hwang, 1997). A summary of the force models $\boldsymbol{f}(\boldsymbol{x}, t)$ used in propagating the state forward as well as in in the calculation of the state transition matrix $\boldsymbol{\phi}(t_{\boldsymbol{k}}, t_{\boldsymbol{k}-1})$ can be found in Table 4.1.

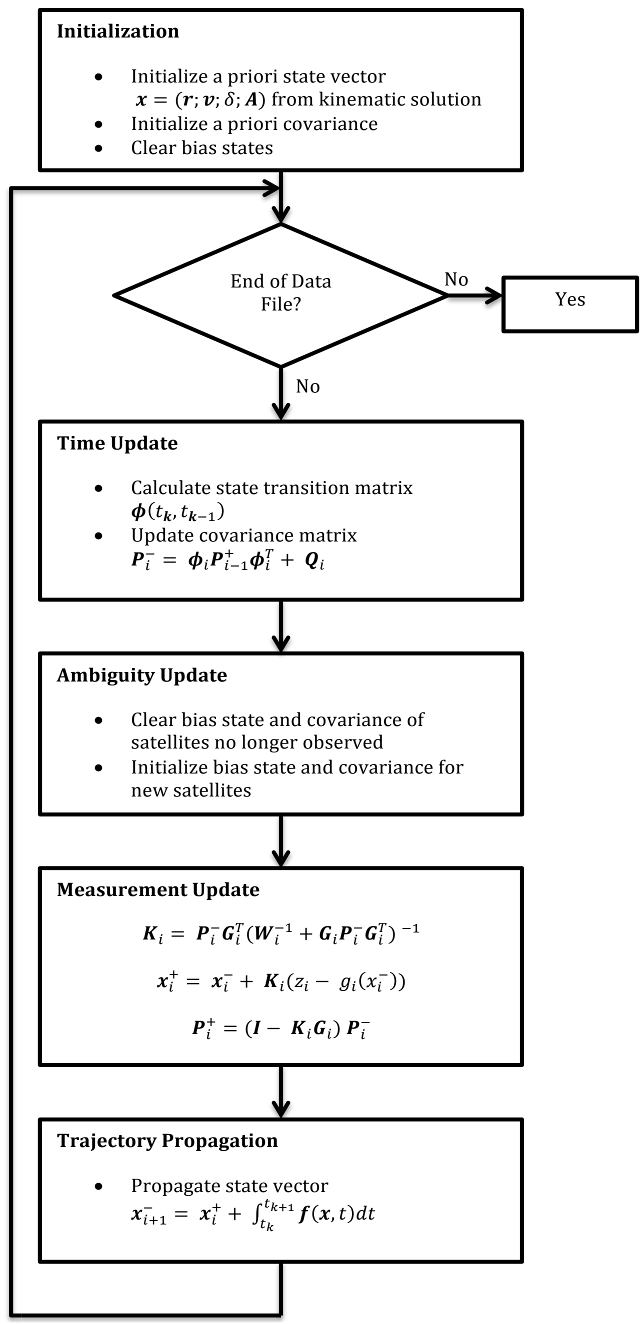


Figure 4.1 Summary of EKF steps

The EKF is initialized with the following covariance matrix:

$$\boldsymbol{P_0} = \begin{pmatrix} 10^1 & 0 & 0 & 0 & 0 & 0 & 0 & 0 & 0 & 0 \\ 0 & 10^1 & 0 & 0 & 0 & 0 & 0 & 0 & 0 & 0 \\ 0 & 0 & 10^1 & 0 & 0 & 0 & 0 & 0 & 0 & 0 \\ 0 & 0 & 0 & 10^1 & 0 & 0 & 0 & 0 & 0 & 0 \\ 0 & 0 & 0 & 0 & 10^1 & 0 & 0 & 0 & 0 & 0 \\ 0 & 0 & 0 & 0 & 0 & 10^1 & 0 & 0 & 0 & 0 \\ 0 & 0 & 0 & 0 & 0 & 0 & 10^4 & 0 & 0 & 0 \\ 0 & 0 & 0 & 0 & 0 & 0 & 0 & 10^{10} & 0 & 0 \\ 0 & 0 & 0 & 0 & 0 & 0 & 0 & 0 & \ddots & 0 \\ 0 & 0 & 0 & 0 & 0 & 0 & 0 & 0 & 0 & 10^{10} \end{pmatrix} \tag{4.8}$$

The values in the initial covariance matrix represent the accuracy of the initial state. Although the state is initialized from the kinematic GPS solution, a 100 $m^2$ covariance is assigned to the position and velocity states (first 6 elements) in case of inaccurate initializations. Although the possibility of the initial state being worse exists, it rarely is the case. The 7$^{th}$ element corresponds to the receiver clock bias, which is assigned a large covariance due to the fact that the clock bias is not modelled in the EKF. Elements 8 and beyond represent the uncertainty in the ambiguities of the carrier-phase measurements, which are completely unknown initially.

## 4.2 Process and Measurement Noise

Since the dynamic models are not perfect, a stochastic component is required in the estimation of the state. The stochastic component is included in the process noise matrix $\boldsymbol{Q}_i$. In order to assign the process noise, some prior knowledge must be known about the quality of the dynamic models. The filter compensates for the incompleteness of the dynamics by using the observed data to make the appropriate corrections to the dynamics. The filter is presented with an estimate of the state from the dynamics and the measurements. The filter then generates a correction to the state predicted by the dynamics that reduces the disagreement between the state predicted by the dynamics and the state according to the measurements. Over time, as the corrections to the dynamic state are generated, the difference between state predicted by the dynamics and the state determined from the observations becomes smaller (Brown and Hwang, 1997).

The measurements are also not perfect, thus a better agreement between the dynamic solution and the observations does not necessarily indicate better accuracy. In order to take measurement noise into consideration, a measurement noise matrix must also be introduced. A very crucial aspect in the implementation of an EKF for LEO orbit determination is to achieve a balance between the available dynamic and geometric information. In the ideal case, the relative weight between the dynamics and measurements will shift back and forth depending on the quality of the observations. When the measurements are noisy, the state solution will exhibit results closer to those predicted by the dynamics.

Achieving a fine balance with the process and measurement noise matrices, also known as tuning, plays a central role in the accuracy of the solution. In the implementation of the processor used in this study, the process noise matrix is set as follows:

$$\boldsymbol{Q} = \begin{pmatrix} 10^{-5} & 0 & 0 & 0 & 0 & 0 & 0 & 0 & 0 & 0 \\ 0 & 10^{-5} & 0 & 0 & 0 & 0 & 0 & 0 & 0 & 0 \\ 0 & 0 & 10^{-5} & 0 & 0 & 0 & 0 & 0 & 0 & 0 \\ 0 & 0 & 0 & 10^{-5} & 0 & 0 & 0 & 0 & 0 & 0 \\ 0 & 0 & 0 & 0 & 10^{-5} & 0 & 0 & 0 & 0 & 0 \\ 0 & 0 & 0 & 0 & 0 & 10^{-5} & 0 & 0 & 0 & 0 \\ 0 & 0 & 0 & 0 & 0 & 0 & 10^{4} & 0 & 0 & 0 \\ 0 & 0 & 0 & 0 & 0 & 0 & 0 & 10^{-4} & 0 & 0 \\ 0 & 0 & 0 & 0 & 0 & 0 & 0 & 0 & \ddots & 0 \\ 0 & 0 & 0 & 0 & 0 & 0 & 0 & 0 & 0 & 10^{-4} \end{pmatrix} \tag{4.9}$$

The first 6 elements correspond to the position and velocity of the state. This means that the process noise matrix is suggesting that the dynamic models are able to propagate the position and velocity state with an accuracy of 0.1 mm. Although the dynamic models are not this accurate, heavy weighting is given to the dynamic modelling due to the noisy measurements collected by the spaceborne receiver. The $7^{th}$ element corresponds to the receiver clock bias. The large value in the process noise matrix indicates that the clock bias is not being modelled and will take on the value as determined by the measurements. The $8^{th}$ element and those beyond represent the process noise for the float ambiguity states. Since the ambiguity for a particular satellite will remain constant, the value of the ambiguity is not expected to change. Because the ambiguities for each satellite cannot be determined exactly, a process noise of 1 mm is thus assigned. Although a process noise of 1 mm may sound highly optimistic, the covariance of the state becomes very large in just a few epochs if only the dynamics are used to propagate the state due to the law of error propagation. The values in the process noise matrix corresponding to the position and velocity states are decreased when a new satellite is introduced. This means that for an epoch when a new satellite is introduced, the solution will be weighted towards the dynamic solution. Putting the weighting towards the dynamics helps reduce the degradation in accuracy caused by the initial estimation of the ambiguity in the carrier-phase measurements from the new satellite. When the GPS measurements are not available and the solution is based solely on the dynamics, the process noise for the positioning and velocity states are raised by a factor of 10. The first 6 elements take on the value of 1 mm and the $7^{th}$ element corresponding to the clock bias remains at $10^4$ m.

The measurement noise matrix is set as follows:

$$\boldsymbol{W} = \begin{pmatrix} 5 & 0 & 0 & 0 & 0 & 0 & 0 & 0 & 0 & 0 \\ 0 & 5 & 0 & 0 & 0 & 0 & 0 & 0 & 0 & 0 \\ 0 & 0 & 5 & 0 & 0 & 0 & 0 & 0 & 0 & 0 \\ 0 & 0 & 0 & \ddots & 0 & 0 & 0 & 0 & 0 & 0 \\ 0 & 0 & 0 & 0 & 5 & 0 & 0 & 0 & 0 & 0 \\ 0 & 0 & 0 & 0 & 0 & 10^{-4} & 0 & 0 & 0 & 0 \\ 0 & 0 & 0 & 0 & 0 & 0 & 10^{-4} & 0 & 0 & 0 \\ 0 & 0 & 0 & 0 & 0 & 0 & 0 & 10^{-4} & 0 & 0 \\ 0 & 0 & 0 & 0 & 0 & 0 & 0 & 0 & \ddots & 0 \\ 0 & 0 & 0 & 0 & 0 & 0 & 0 & 0 & 0 & 10^{-4} \end{pmatrix} \tag{4.10}$$

The first half of the elements represent the measurement noise corresponding to the pseudorange measurements and the second half of the elements represent the measurement noise corresponding to the carrier-phase measurements. The value of the elements represents the uncertainty in the measurements. Since the data used in this study are collected by a spaceborne receiver, the pseudorange measurements are expected to be accurate to within 5 m. A value of 5 m was chosen because the pseudorange measurements are quite noisy from various contributors such as multipath. Since the carrier-phase measurements are more precise than the pseudorange measurements, the carrier-phase measurement noise is set to 1 mm. When a new satellite is introduced, the measurement noise matrix is increased that puts more weighting on the dynamics. This prevents the initialization of the ambiguity of the new satellite from causing any large degradation in the solution accuracy. The tuning of the EKF in this manner produces the most accurate solution, as verified by the JPL reference solution.

## 4.3 Reduced Dynamic Orbit Results

The merits of PPP are combined with the dynamical models in the formulation of an EKF in what is known as the reduced dynamic technique in order to increase the accuracy of the state. The utilization of the reduced dynamic technique allows for a more accurate solution. The state is estimated using undifferenced pseudorange and carrier-phase GPS measurements. A state obtained from the use of the GPS measurements is used to initialize the EKF. The information on the employed dynamical models, parameter sets and reference system conventions are summarized in Table 4.1, which are fairly standard when producing a reduced dynamic orbit (Montenbruck et al., 2005).

| Item | Description |
|---|---|
| Static gravity field | EIGEN 100x100 |
| Luni-solar gravitation | Analytical series expansions of luni-solar coordinates<br>Point mass approximation |
| Radiation Pressure | Solar radiation pressure (cannon-ball model) |
| Atmospheric Drag | Harris-Priester Model |
| Terrestrial reference system | ITRS2000 |
| Inertial reference system | ICRS |
| Earth Orientation | IAU 1976 precession<br>IAU 1980 nutation<br>IAU 1982 sidereal time<br>IERS polar motion<br>IERS UT1-GPS |

Table 4.1 Overview of dynamical models and reference system transformations employed for CHAMP orbit determination utilizing the reduced dynamic technique

The results for the daily rms of days 115 – 121 in the year 2008 processed using the reduced dynamic technique are displayed in Figure 4.2 along with the associated statistics summarized in Table 4.2. The mean daily rms for the 7 days is 21 cm, with a minimum of 19 cm and a maximum of 24 cm. The standard deviation is 2.2 cm, which is significantly smaller than the kinematic orbit, as discussed in Section 3.5, indicating improved solution repeatability. In terms of the rms error, the reduced dynamic technique provides an increase of 8 cm, or 38% in accuracy when compared to the kinematic-only approach. Other than the improvement in accuracy, one large advantage of the reduced dynamic approach as compared to the kinematic-only approach is that the reduced dynamic approach provides a state solution for every epoch. In the kinematic-only formulation, when there are not enough tracked GPS satellites, the state solution for that epoch is not available. In the reduced dynamic technique however, when there are not sufficient GPS data available, the dynamics are able to propagate the state forward using the information from the previous epoch. Previous studies such as Montenbruck et al. (2005) have been able to achieve orbits as accurate as 10 cm (3D rms). The fact that the results obtained in this study are inferior to 10 cm is due to the fact that the GPS quality control techniques have not been perfected and certain perturbations in the dynamic models such as Solid Earth tides, Ocean tides and empirical accelerations have been neglected due to MATLAB processing time considerations and time constraints.

Figure 4.3 shows a time series of the 3D difference for a 24-hour period for the 117$^{th}$ day of the year 2008. The reason for choosing this day is because the rms of this day corresponds to the average of the 7-day daily rms values. There exist two major differences between the kinematic-only solution and the solution produced by the reduced dynamic technique. The accuracy of the reduced dynamic approach is better than the accuracy of the kinematic-only solution that utilizes only the GPS measurement without any dynamical aiding. In addition, there exist no gaps in the solution produced with the reduced dynamic technique, which is not the case with kinematic-only orbit. These two major advantages of the reduced dynamic approach make the technique very attractive to those interested in decimetre-level 3D differences while producing a solution for all epochs. The majority of the error values above or below 50 cm are either due to initializations after re-acquiring the GPS satellites or the dynamic models receiving an inaccurate initial state prior to long GPS data gaps. Before a GPS data outage occurs, the number of tracked GPS satellites typically drops and/or the GPS satellite geometry is non-ideal. Although the EKF shifts the weighting towards the dynamics when the GPS data is noisy, there still exist slight chances of initializing the dynamics with a state that has slightly degraded accuracy. Nonetheless, the EKF implementation combining the dynamics and the GPS measurements is able to filter out noisy measurements and produce errors at the decimetre level.

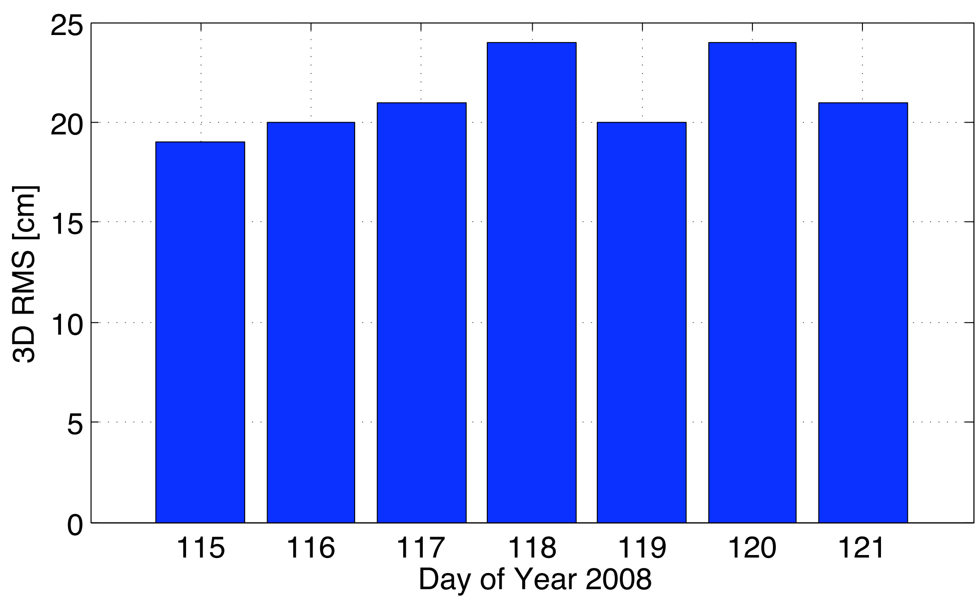


Figure 4.2 3D rms of 24-hour intervals for days 115 – 121 of year 2008 by post-processing dual-frequency data using the reduced dynamic technique

| Mean | Std. Dev. | Maximum | Minimum |
|---|---|---|---|
| 21 cm | 2.2 cm | 24 cm | 19 cm |

Table 4.2 Summary statistics of 3D rms of 24-hour intervals for days 115 – 121 of year 2008 by post-processing dual-frequency data using the reduced dynamic technique

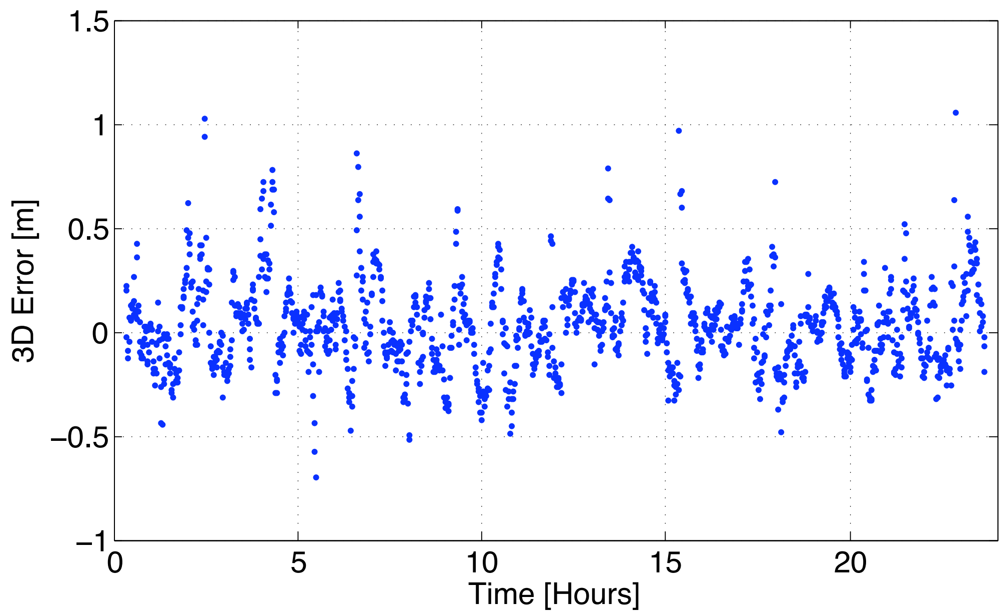


Figure 4.3 Time series of 3D error of a 24-hour interval for 117th day of year 2008 by post-processing dual-frequency data using the reduced dynamic technique comparing at 60-second intervals

It is also useful to look at the 3D standard deviation of the position state generated with the reduced dynamic technique. Figure 4.4 shows the 3D standard deviation obtained from the first 3 diagonal elements of the covariance matrix in the EKF implementation. As was the case with the position error, the 3D standard deviation also displays quite different trends from the ones produced by processing only the GPS measurements without any dynamical aiding. The values of the 3D standard deviation going as high as a few metres arise from the dynamics in cases where GPS data are not available for long periods of time and the covariance matrix is propagated forward using the law of error propagation.

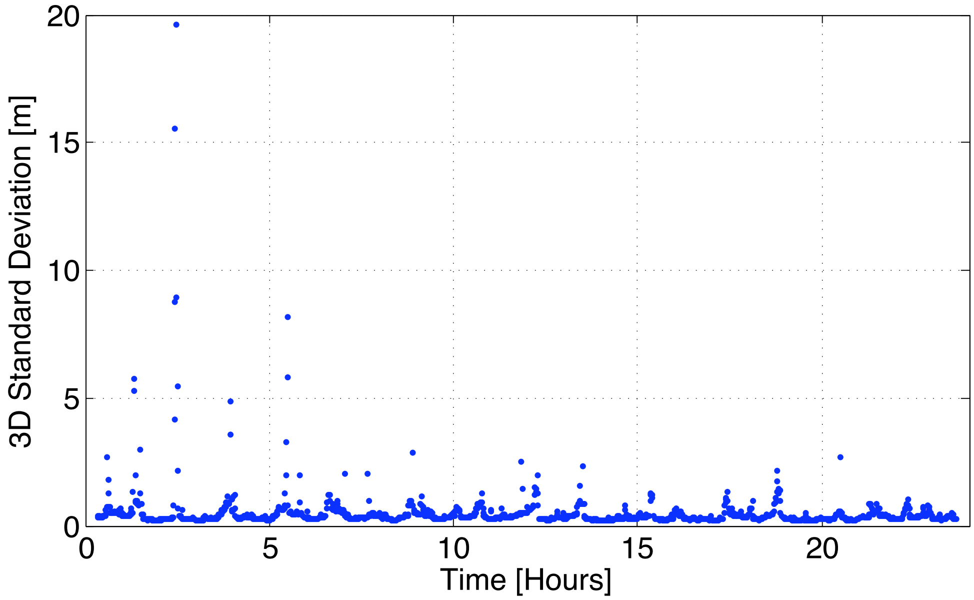


Figure 4.4 3D standard deviation of a 24-hour interval for 117th day of year 2008 by post-processing dual-frequency data using the reduced dynamic technique at 60-second intervals

Without any GPS data however, the measurement update cannot be applied. Applying only the time update increases the covariance, as there exists uncertainty in the propagated state as by the law of error propagation. The longer the GPS data gap, the larger will be the uncertainty of the propagated state, hence a larger covariance. The EKF is tuned in such a manner that when the state is propagated using only the dynamic models, the process noise is set to produce the covariance values observed in Figure 4.4. The advantage of tuning the filter in this manner is that when the GPS data becomes available again, the solution will quickly converge to the correct state. In order to ensure that inaccurate initializations do not affect the overall accuracy of the state, a 3D standard deviation cutoff of 10 m is implemented. The covariance of the ambiguity states is also computed and a cutoff of 3 m is implemented. The cutoff allows the solution to be based on just the dynamics if the GPS data are producing a highly inaccurate state.

In order to gain a greater understanding of the behaviour of the 3D standard deviation, a close-up of Figure 4.4 for a few hours is shown in Figure 4.5. A close-up of any interval for any of the 7 days looks very similar to that in Figure 4.5, except for rare cases. The minimum value that the standard deviation can reach is defined by the process noise matrix $\boldsymbol{Q}_i$. If the quality of the GPS measurements is undesirable or there is no availability of the GPS data, the 3D standard deviation becomes larger, indicating a rising uncertainty in the state. When the GPS measurements are reliable, the 3D standard deviation hovers around 30 cm. The validity of the use of the 3D standard deviation to assess the accuracy of the solution is thus verified with the use of external means to determine the accuracy of the state.

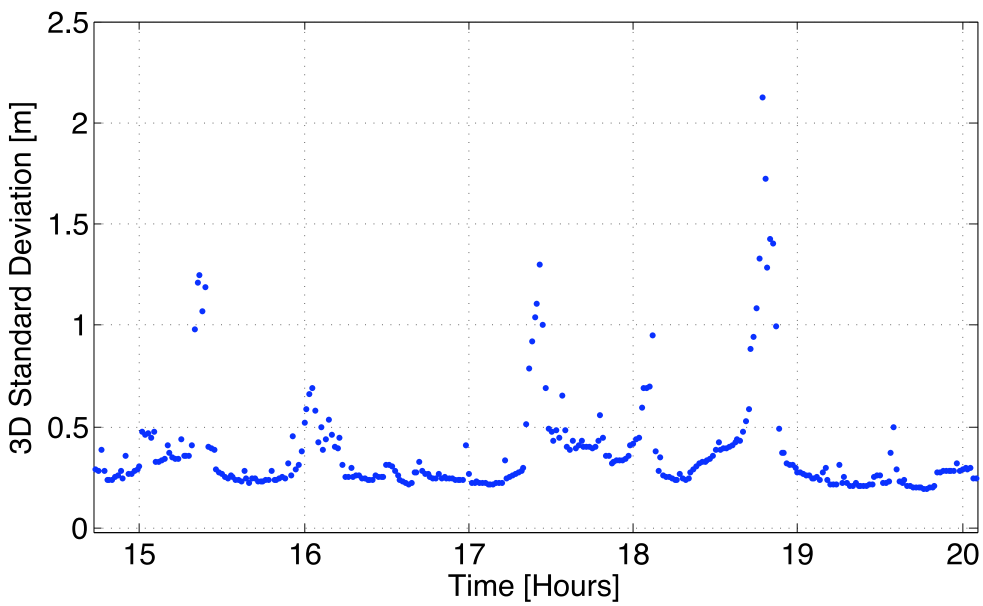


Figure 4.5 3D standard deviation of a 5-hour interval for 117th day of year 2008 by post-processing dual-frequency data using the reduced dynamic technique at 60-second intervals

# Chapter 5

## 5 Constrained Orbit Solution Experiments

In order to investigate the degradation in position accuracy with various constraints, 6 hour data arcs are analyzed. Since the orbit period of CHAMP is about 94 minutes, a 6-hour data arc corresponds to slightly fewer than 4 orbits. For each day, a 6-hour period with the lowest rms value is selected so that the solutions are not tainted with any outliers. A 6-hour period for the 7 days, which contains 25% of the data of a daily RINEX file for each day, is sufficient to draw reliable conclusions. For most of the scenarios, an 8-hour period is processed, but the solution for the first and last hour is truncated, as not used in the calculation of the rms to help ensure that the results are not skewed by convergence periods. In addition, the EKF gives the opportunity to build momentum and generate results in the proximity of the reference solution. The results from the various experiments in this chapter are presented in the following manner. Firstly, the reference solution for each scenario is presented. The scenarios investigated in this study are: 1) the post-processed dual-frequency solution, 2) the real-time dual-frequency solution, 3) the post-processed single-frequency solution and 4) the real-time single-frequency solution. For each of the scenarios, various constraints are applied and the same data are processed once again. The first constraint is a simulation of a 50% duty cycle of the GPS receiver. The receiver is simulated to be switched on for 15 minutes and switched off for 15 minutes. During the 15-minute GPS data gap, the dynamic models propagate the state forward, thereby providing a continuous solution. In addition, a 25% duty cycle is also simulated with the receiver turned on for 5 minutes and turned off for 15 minutes. As with the case of the 50% duty cycle, the dynamics fill in for the GPS data gaps and a solution is continuously maintained. Another constraint that is placed on the various scenarios is that the receiver is simulated to be switched on for one orbit and switched off for one orbit. The difference here is that during the time that the receiver is simulated to be switched off, a solution is not produced. This situation is acceptable when a continuous solution is not necessary and when the onboard resources are highly limited. Another similar constraint tested is that the receiver is simulated to be switched on for two orbits and switched off for two orbits. Once again, a solution is not produced during the times that the receiver is simulated to be switched off.

## 5.1 Post-Processed Dual-Frequency Solution

The major advantages of post-processing the GPS data are that precise GPS satellite orbit and clock information can be used and the solution can be smoothed, as explained in Chapter 3, thus providing much more accurate results. This section discusses the results of post-processed dual-frequency reference solution (100% duty cycle, 4 orbits) followed by the constrained solution results.

### 5.1.1 Post-Processed Dual-Frequency Reference Solution

The 3D rms error values of the post-processed dual-frequency solution for each of the 7 days for 6-hour periods are displayed in Figure 5.1. The associated statistics are presented in Table 5.1. Post-processing of dual-frequency data is the best scenario for achieving the most accurate results. The results in Figure 5.1 are generated by utilizing the precise GPS satellite orbits and clocks and smoothing all available data in the 6-hour intervals for each day. Previous studies such as Montenbruck and Ramos-Bosch (2007) have achieved 3D rms values of 17 cm with data from CHAMP utilizing the forward-only EKF. Thus a 3D rms of 15 cm obtained by the software developed for this study is sufficient to produce trustworthy results of the experiments.

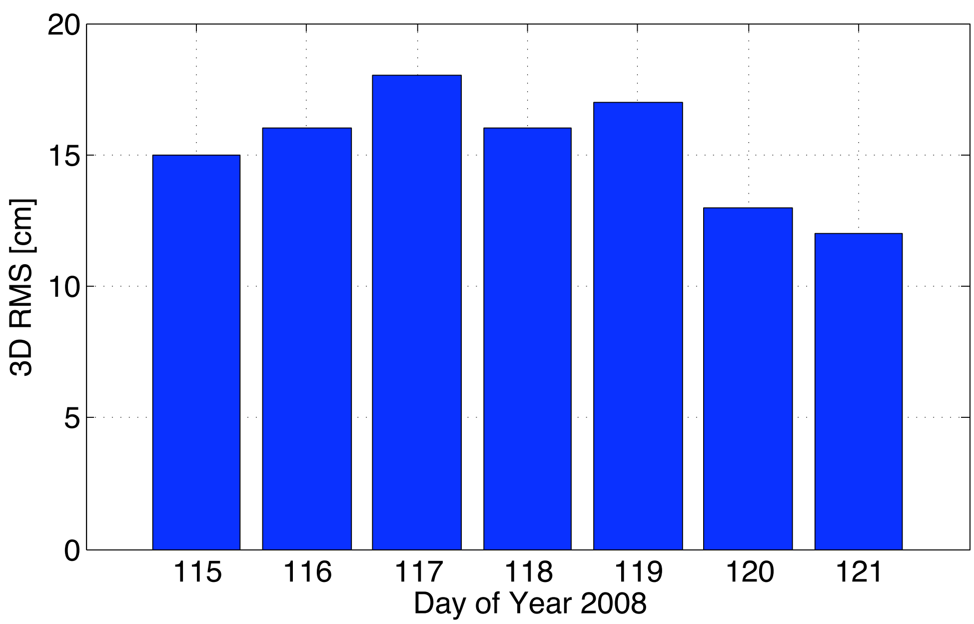


Figure 5.1 3D rms of 6-hour intervals for days 115 – 121 of year 2008 by post-processing dual-frequency data using the reduced dynamic technique

| Mean | Std. Dev. | Maximum | Minimum |
|---|---|---|---|
| 15 cm | 2.1 cm | 18 cm | 12 cm |

Table 5.1 Summary statistics of 3D rms of 6-hour intervals for days 115 – 121 of year 2008 by post-processing dual-frequency data using the reduced dynamic technique

A time series of the 3D difference between the calculated smoothed solution and that of JPL for the 115$^{th}$ day of 2008 is shown in Figure 5.2. The reason for choosing the 115$^{th}$ day is because the 3D rms of this particular day is the closest to the average 3D rms of the 7 days. One apparent characteristic of the time series in Figure 5.2 is the sinusoidal pattern. This pattern can be caused by various factors such as the dynamic modelling and the momentum shifts in the weighting between the dynamics and GPS measurements in the EKF. However, the most likely cause of the sinusoidal pattern is due to differences in the processing techniques of the two compared solutions. Aside from the presence of some outliers around 7.5 hours, the 3D difference is at the few decimetre-level and within an acceptable range. The 3D error plots for the remaining 6 six days look very similar to that in Figure 5.2.

Figure 5.3 shows the 3D difference between a solution produced by JPL and a solution produced by COSMIC Data Analysis and Archive Centre (CDAAC) for the 115$^{th}$ day of the year 2008. Once again, a slight sinusoidal pattern is observed in the time series of the difference between the solution produced by JPL and CDAAC, which can most likely be attributed to the differences in processing methods by the two institutions.

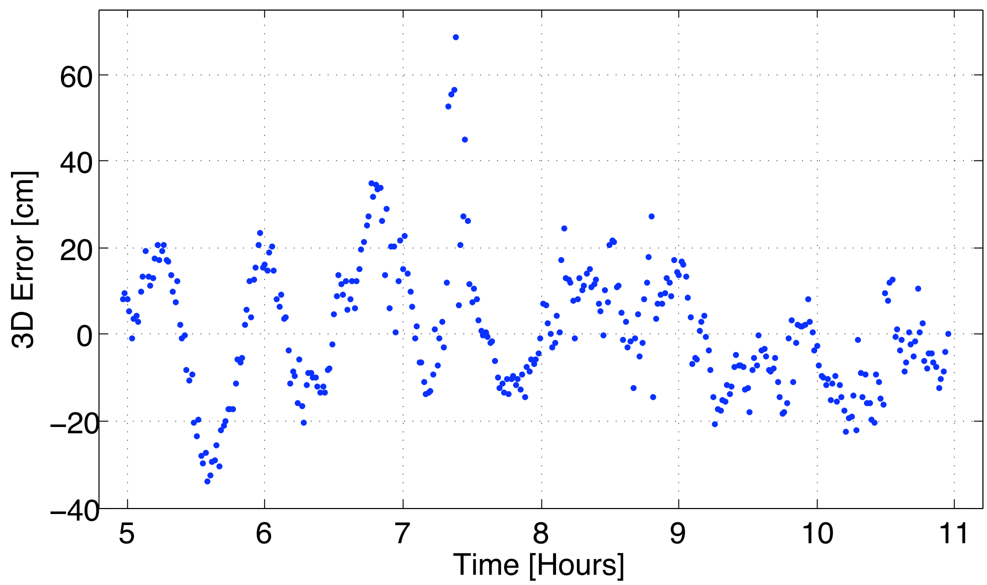


Figure 5.2 Time series of 3D difference of a 6-hour interval for 115th day of year 2008 by post-processing dual-frequency data using the reduced dynamic technique comparing at 60-second intervals

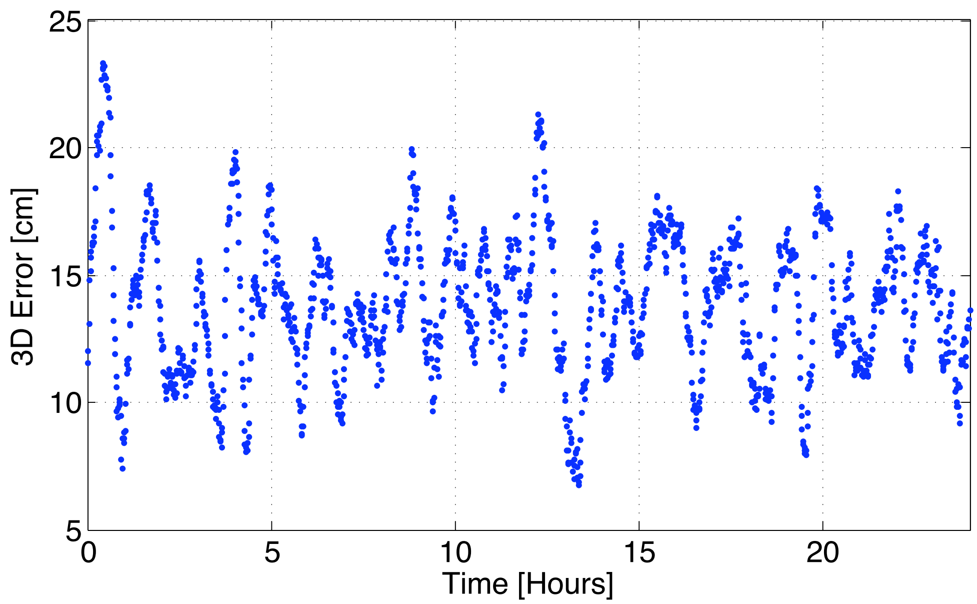


Figure 5.3 Time series of the 3D difference between solutions produced by JPL and CDAAC for a 24-hour interval for 115th day of year 2008 comparing at 60-second intervals

The 3D rms for the 115$^{th}$ day when comparing the JPL solution to the CDAAC solution is 14 cm. This difference indicates that the solutions produced by different institutions do not exactly agree and therefore justifies the 15 cm 3D rms error achieved by the processor used in this study. This provides reassurance to the fact that the processing techniques used in this study are accurate and will thus provide reliable conclusions for the constrained cases.

The 3D standard deviation for the 6-hour interval for day 115 of year 2008 is displayed in Figure 5.4. The 3D standard deviation hovers between 18 cm and 1.4 m. The large increase in the 3D standard deviation observed at the 7.5 hour mark represents a large GPS data gap where the dynamic models are used to propagate the solution without the use of any GPS measurements.

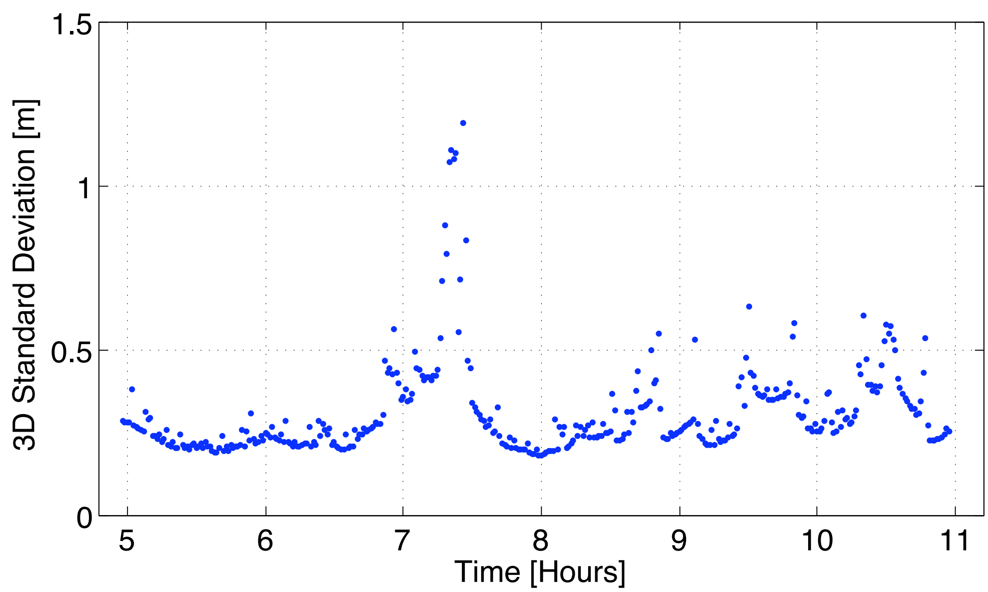


Figure 5.4 3D standard deviation of a 6-hour interval for 115th day of year 2008 by post-processing dual-frequency data using the reduced dynamic technique at 60-second intervals

Since the 3D standard deviation increases around the 7.5 hour mark, a degradation in position accuracy is also observed at the same time, shown in Figure 5.2. Thus, the 3D standard deviation output from the EKF provides realistic values that describe the accuracy of the position solution fairly well.

### 5.1.2 Post-Processed Dual-Frequency Constrained Solution

This section discusses the results of the post-processed dual-frequency solution when the GPS receiver is in non-continuous operation. The scenario of the 50% duty cycle is created by simulating the receiver to be switched on 15 minutes and switched off for 15 minutes. Simulating the receiver off time is accomplished by directly deleting the information related to the off time measurements from the RINEX file once the file has been read by MATLAB. It is thus important to keep in mind that the time that the receiver is on represents the time that the receiver is collecting data. For receiver on-off times of 15 minutes, the following results may not apply to receivers undergoing a cold start. However, simulations have shown that a 'hot start' of the receiver can achieve a time to first fix to better than 20 seconds with minimal power consumption. The difference between a cold start and a 'hot start' is that in a 'hot start' the GPS receiver stores its last calculated position, the almanac, UTC time and the GPS satellite constellation that was in view. When the receiver is turned on, it is able to acquire lock on these GPS satellites and compute a position fairly quickly. In a cold start however, the GPS receiver deletes all past information and takes longer to compute the position since no previous information about the receiver or the GPS satellites is known (Leung et al., 2001). The 25% duty cycle is created by simulating the receiver to be switched on for 5 minutes and switched off for 15 minutes. The results of the 50% and 25% duty cycle are compared with the JPL reference solution in Figure 5.5. During the 6-hour intervals, the position, velocity and receiver clock bias are calculated continuously with the dynamic models filling in for the GPS measurement gaps that occur naturally and when the receiver is switched off. As expected, the error in the position grows larger as the duty cycle of the GPS receiver decreases. Also, the variability in solution accuracy grows as well. The amount of improvement in the solution accuracy seen by increasing the duty cycle varies from day to day. The amount of improvement depends heavily on the quality of the data. Large naturally occurring data gaps during receiver on times, inaccurate initializations when the receiver is switched on, and long initialization periods when the receiver is turned on can all contribute large degradations in accuracy, hence producing large 3D rms values. Nonetheless, the trend is quite visible.

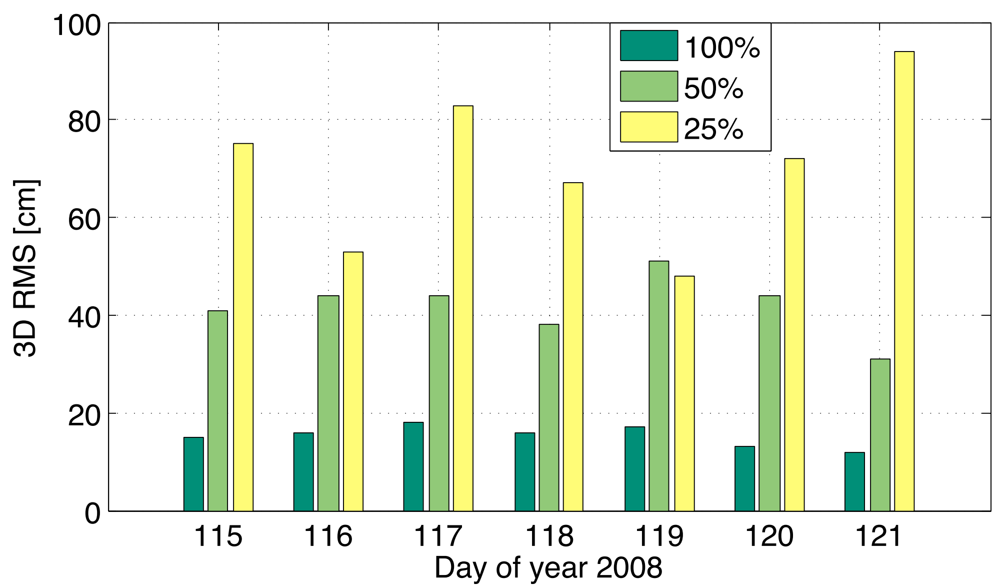


Figure 5.5 3D rms of 6-hour intervals for days 115 – 121 of year 2008 by post-processing dual-frequency data using the reduced dynamic technique for a 100%, 50% and 25% duty cycle

A summary of the statistics of the 7 days associated with Figure 5.5 is displayed in Table 5.2. By transitioning from the 100% duty cycle to the 50% duty cycle, the 3D rms error increases from 15 cm to 42 cm, which corresponds to a 180% decrease in accuracy. By transitioning from the 100% duty cycle to the 25% duty cycle, the 3D rms rises from 15 cm to 71 cm, which is a 370% decrease in accuracy. For an application requiring a solution with $1\sigma$ better than half a metre, the 50% duty cycle would be ideal, thus reserving power onboard the LEO for other equipment. The 25% duty cycle is ideal for an application requiring a solution with a $1\sigma$ value to be better than 1 m.

| | **100% Duty Cycle** | **50% Duty Cycle** | **25% Duty Cycle** |
|---|---|---|---|
| **3D rms** | 15 cm | 42 cm | 71 cm |
| **% Increase** | -- | 180 % | 370 % |

Table 5.2 Summary statistics of 3D rms of 6-hour intervals for days 115 – 121 of year 2008 by post-processing dual-frequency data using the reduced dynamic technique for a 100%, 50% and 25% duty cycle

The average 3D rms error values for the 7 days are not to be confused with the maximum 3D difference one can expect. The maximum 3D differences in the smoothed solution for each day for the 50% and 25% duty cycle are shown in Table 5.3. The maximum error values for the 50% duty cycle are quite consistent and have a range of 70 cm. This however, is not the case for the 25% duty cycle. The longer data gaps and shorter receiver on times produce erratic behaviour. The larger maximum 3D differences observed on days 117 and 121 are caused by two different reasons. On day 117, an inaccurate initialization occurs once the receiver is switched on in the middle of the 6-hour interval. On day 121, an inaccurate initialization is made to the dynamic models, hence producing a relatively large divergence from the true position during the receiver off time. What this means is that as the duty cycle of the GPS receiver decreases, there arise many potential sources of error that can affect solution accuracy.

| | **Day 115** | **Day 116** | **Day 117** | **Day 118** | **Day 119** | **Day 120** | **Day 121** |
|---|---|---|---|---|---|---|---|
| **50%** | 1.6 m | 2.1 m | 2.2 m | 1.7 m | 1.6 m | 1.9 m | 1.5 m |
| **25%** | 3.9 m | 3.1 m | 6.0 m | 3.7 m | 1.6 m | 3.7 m | 5.9 m |

Table 5.3 Summary statistics of maximum 3D difference of 6-hour intervals for days 115 – 121 of year 2008 by post-processing dual-frequency data using the reduced dynamic technique for a 50% and 25% duty cycle

In order to gain more insight into the quality of the solution, a time series of the 3D difference for day 115 of 2008 for the case of the 50% duty cycle is displayed in Figure 5.6, which shows the 3D difference for the forward run, backward run and the smoothed solution. The receiver off periods are clearly seen, along with the divergence from the reference LEO orbit. This is evident in both the forward and backward runs. The smoothing technique for a situation such as this proves to be very helpful in reducing the position error. The amount of divergence from the reference solution during the receiver off times depends on the quality of the GPS data prior to the receiver being switched off, hence the accuracy of the initialization state to the dynamic models. The case of the 25% duty cycle is quite similar, except that the data gaps are more frequent due to the fact that the receiver is switched on for a shorter time period. The shorter on-times of the receiver cause the overall accuracy of the solution to degrade since there is significantly less reliance on the GPS measurements in the case of the 25% duty cycle as compared to the 50% duty cycle.

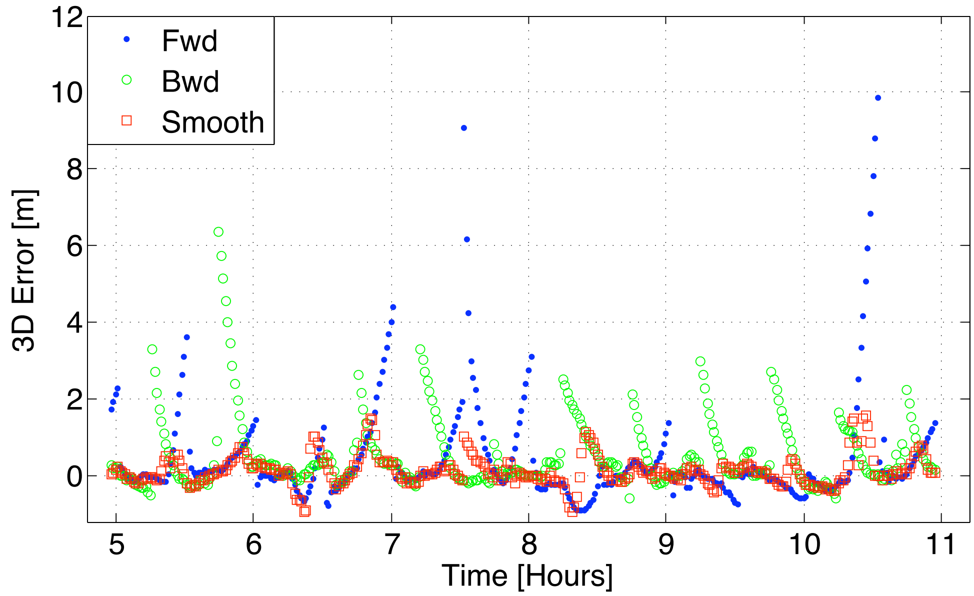


Figure 5.6 Time series of 3D error of a 6-hour interval for 115th day of year 2008 by post-processing dual-frequency data using the reduced dynamic technique comparing at 60-second intervals for a 50% duty cycle

Figure 5.7 shows the 3D standard deviation for the 115th day of year 2008. As soon as a GPS data gap is encountered, the dynamics take over and the 3D standard deviation increases as dictated by the law of error propagation. Thus, the periodic increases of the 3D standard deviation in the forward and backward run are due to the dynamics propagating the state without the availability of any GPS measurements. The uncertainty of the smoothed solution is smaller than the forward and backward runs. The 3D standard deviation of the smoothed solution indicates an error of almost 10 m at some epochs. This is much larger than the errors that occur in reality. Tuning the EKF can alter the maximum and minimum values of the 3D standard deviation. Allowing the EKF to be pessimistic about the accuracy of the solution allows rapid re-initializations of the GPS solution. The problem with allowing the EKF to be too pessimistic about the accuracy is that if the GPS solution re-initialization is inaccurate, the accuracy of the overall solution will suffer. The EKF is therefore tuned in such a manner that the solution will begin to follow the GPS measurements relatively quickly after the receiver has been turned on, but not too quickly so that the accuracy will suffer if re-initialization produces an inaccurate solution.

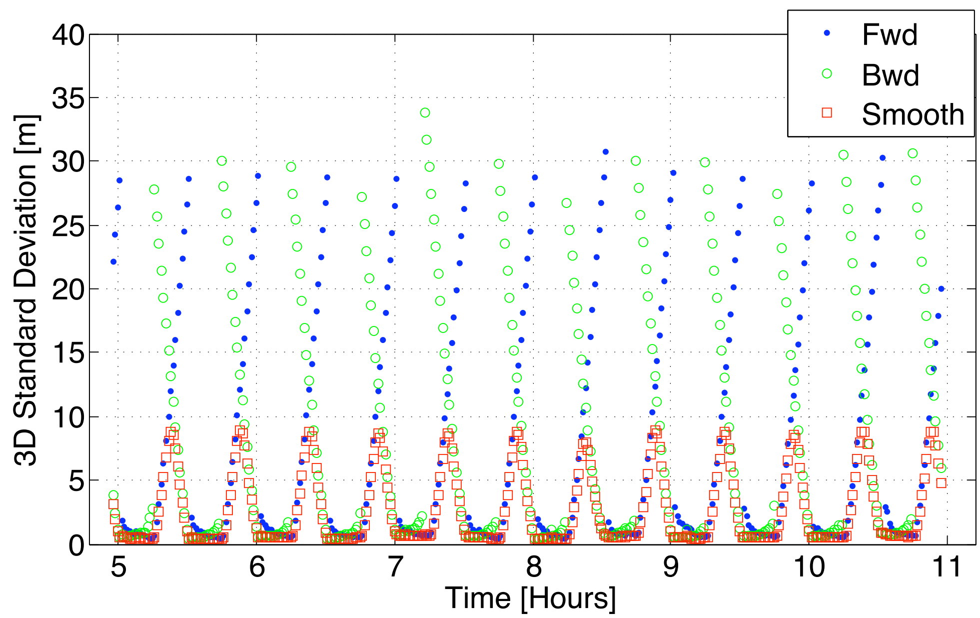


Figure 5.7 3D standard deviation of a 6-hour interval for 115th day of year 2008 by post-processing dual-frequency data using the reduced dynamic technique at 60-second intervals for a 50% duty cycle

In order to demonstrate the merits of smoothing the data, which can only be accomplished if the data are post-processed, Figure 5.8 displays, in large scale, a section of the time series from Figure 5.6. Once the receiver is switched off, the solutions in both the forward and backward direction begin to diverge from the reference solution, depending primarily on the accuracy initial state required to propagate the solution using the dynamic models. The smoothed solution then produces a state that is more accurate than the forward and backward run.

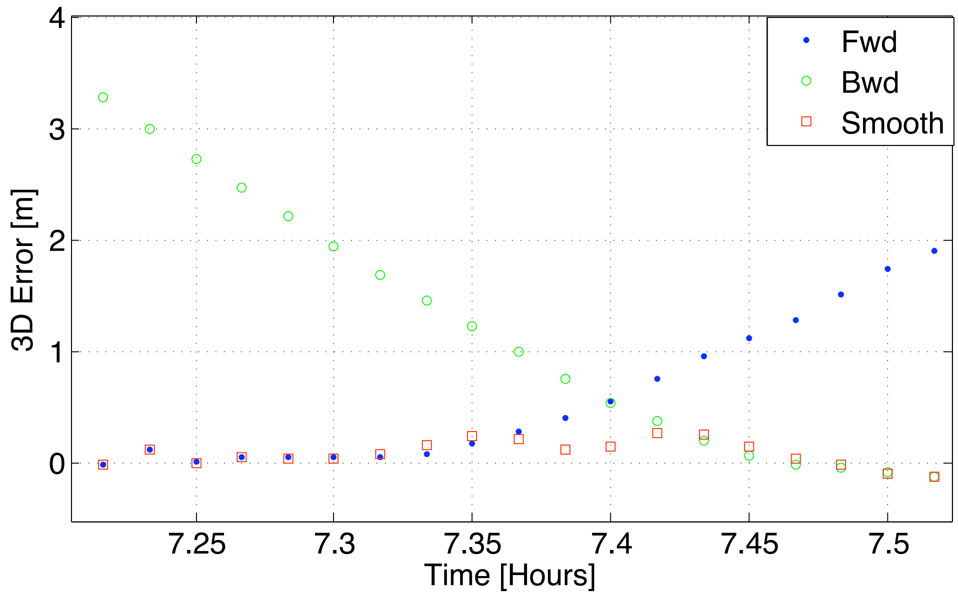


Figure 5.8 Time series of 3D error of a 25-minute interval for 115th day of year 2008 by post-processing dual-frequency data using the reduced dynamic technique comparing at 60-second intervals for a 50% duty cycle

A similar pattern is observed in the 3D standard deviation, as shown in Figure 5.9. Once again, although the position accuracy does not reduce to close to 10 m, tuning the EKF in such a way produces the most accurate overall solution when compared to an external source. The smoothed solution produces an uncertainty that is smaller than either the forward or the backward run, thus producing a more accurate state with a smaller uncertainty. A possible avenue for future research would be to tune the EKF so that more realistic filter/smoother standard deviations are generated.

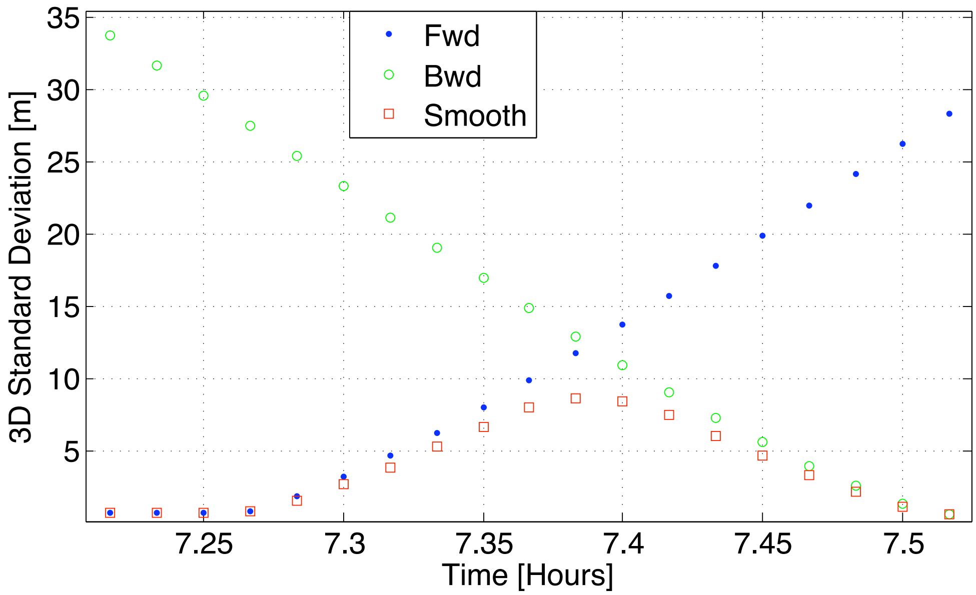


Figure 5.9 3D standard deviation of a 25-min interval for 115$^{th}$ day of year 2008 by post-processing dual-frequency data using the reduced dynamic technique at 60-second intervals for a 50% duty cycle

The results of the post-processed, dual-frequency, non-continuous solution are now presented. There are two cases that are investigated: the receiver is switched on for two orbits and switched off for two orbits; and the receiver is switched on for one orbit and switched off for one orbit. During the times that the receiver is not on, positioning and velocity information is not available. The dynamic modelling helps fill in the naturally occurring data gaps that arise when the receiver is switched on, but does not fill in the long data gaps that occur when the receiver is switched off. The 3D rms results for the 7 days are displayed in Figure 5.10. The first and last 10 minutes of the orbit solution are not included in the calculation of the statistics, in order to ensure that the convergence period does not impact the overall solution. Unlike the continuous solution, a definite pattern is not observed. Generally, the accuracy of the solution decreases when decreasing the amount of time the receiver remains on. The difference in accuracies between 2 orbits on / 2 orbits off and 1 orbit on / 1 orbit off is minimal. In the design of a mission, one can choose either of these scenarios and expect similar accuracy results. It is however preferable to have the receiver switched on for long periods of time, as indicated by the superiority in accuracy of 4 orbits over the other two scenarios. In transitioning from 4 orbits to 2 orbits, a slight improvement in accuracy is seen in some of the days. Thus going from 4 orbits to 2 orbits does not always cause a large variation in accuracy, just as going from 2 orbits on / 2 orbits off to 1 orbit on / 1 orbit off does not cause a large variation in accuracy. It is by going from 4 orbits on to 1 orbit on / 1 orbit off that a significant degradation of 33% in accuracy is observed.

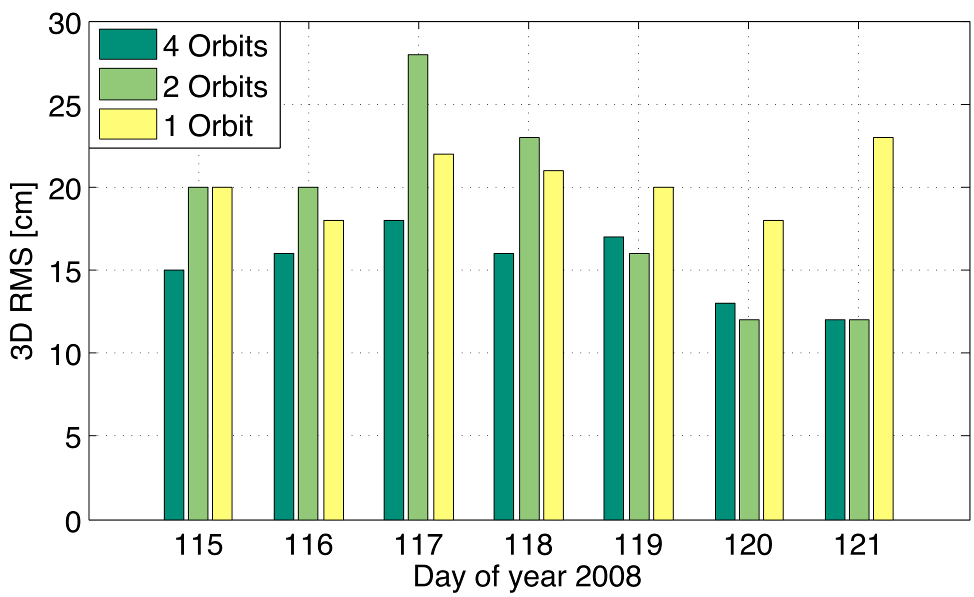


Figure 5.10 3D rms of 6-hour intervals for days 115 – 121 of year 2008 by post-processing dual-frequency data using the reduced dynamic technique for a 4 orbits, 2 orbits and 1 orbit on/1 orbit off

## 5.2 Real-Time Dual-Frequency Solution

The two major differences between the post-processed solution and the real-time solution are that in real-time: 1) the data cannot be smoothed; and 2) the lower accuracy GPS satellite broadcast ephemeris and clocks must be utilized. In most cases requiring a real-time solution, the processing time must be short. The best way to minimize the processing time in the reduced dynamic technique is to limit the complexity of the dynamic models, which contribute a significant amount to the overall processing time. In this study, two different methods for real-time processing are investigated: real-time processing with full dynamics and real-time processing with limited dynamics. In the case of full dynamics, a 100x100 gravitational model is utilized as well as third-body perturbations from the Sun and the Moon, air drag and solar radiation pressure. In the case of limited dynamics, only the $J_2$ gravitational model is utilized and all other perturbations are not modelled. In transitioning from full dynamics to limited dynamics, a 46% decrease in processing time is observed, which is quite significant for constrained LEO missions in which a shorter processing time may take priority over accuracy.

### 5.2.1 Real-Time Dual-Frequency Reference Solution

The results for 3D rms values of the 7 days for the full and limited dynamics cases are displayed in Figure 5.11. Generally speaking, the results for the limited dynamics case are less accurate than their full dynamics counterparts. This degradation in accuracy is subtle for most cases. On some of the days, the limited dynamics marginally out perform the full dynamics cases, because other changes, such as the residual and standard deviation cutoff values have also been made in the processor when going from full dynamics to limited dynamics. A future task that can enhance the quality of the results is making the processor more robust and less data dependent, thereby producing more uniform results for all datasets. This can be accomplished by improving the algorithms associated with outlier detection. The residual cutoffs for the GPS measurements along with the covariance cutoffs have been increased in the limited dynamics case, because of the decreased accuracy of the dynamic models, hence the reduced dynamic solution. The change in accuracy from the full dynamics to the limited dynamics is due to the combination of changing the dynamic models, as well as the residual and covariance cutoff values. The residual and covariance cutoff values are optimized in both cases to produce the most accurate solutions, as confirmed by external sources.

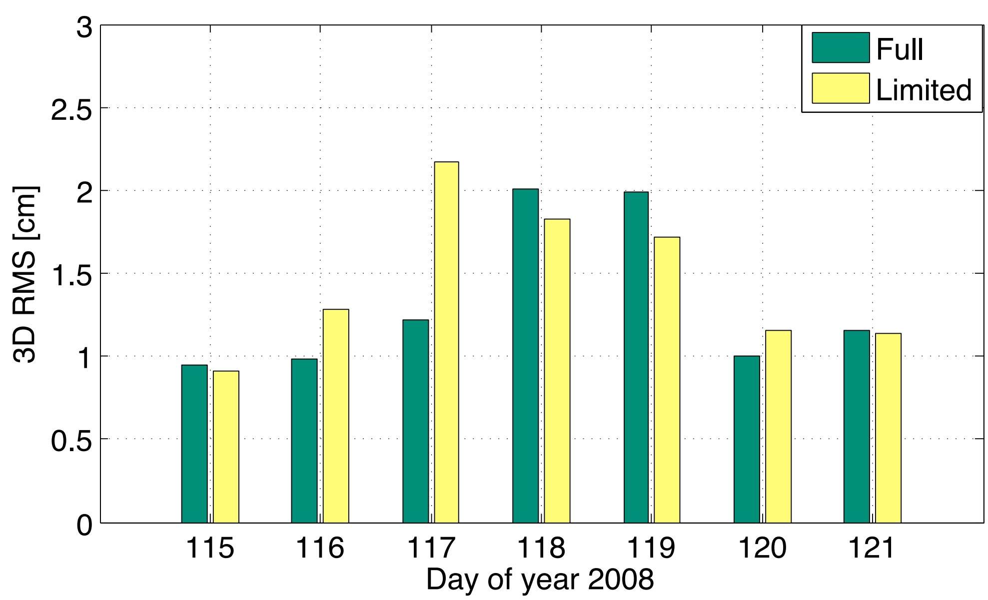


Figure 5.11 3D rms of 6-hour intervals for days 115 – 121 of year 2008 processing dual-frequency data in real time using the reduced dynamic technique with full dynamics and limited dynamics

A summary of the statistics associated with Figure 5.11 is displayed in Table 5.4. Unlike in the case of post-processing, the range between the minimum and maximum 3D rms values for the real-time case for the 7 days is much larger. The mean 3D rms for the full dynamics case increases from 15 cm to 1.3 m, or 770% in the real-time scenario when comparing to the post-processed solution. This significant degradation is expected, as there exist more error sources in real-time processing such as the utilization of the less accurate GPS satellite clocks and orbits. Previous studies such as Montenbruck and Ramos-Bosch (2007) have achieved accuracies as high as 69 cm with CHAMP data with real-time processing. The results obtained in obtained in this study are slightly are inferior due to imperfections in outlier detection techniques, as well as exclusions of parameters such as empirical accelerations associated with the dynamic modelling in the EKF states. Nonetheless, a 3D rms value of 1.3 m for the full dynamics case is accurate enough to provide reliable constrained experimented results. The inability to smooth the data also allows for the presence of outliers that have major effects in the determination of the 3D rms. Once again, the fact that the result for the minimum 3D rms is better in the limited dynamics case is due to the alteration of the residual and covariance cutoffs. Even though the alteration in the cutoff values may prove to be helpful in one data set, this does not apply when taking the average over many data sets.

| | **Mean** | **Std. Dev.** | **Maximum** | **Minimum** |
|---|---|---|---|---|
| **Full Dynamics** | 1.3 m | 0.47 m | 2.0 m | 0.95 m |
| **Limited Dynamics** | 1.5 m | 0.45 m | 2.2 m | 0.91 m |

Table 5.4 Summary statistics of 3D rms of 6-hour intervals for days 115 – 121 of year 2008 by processing dual-frequency data in real-time using the reduced dynamic technique with full dynamics and limited dynamics

In order gain a better understanding of the real-time solution, a time series of the 3D difference for the full dynamics case is presented in Figure 5.12. The difference in the real-time 3D difference time series as compared to the post-processed 3D error time series is that the data are only filtered and not smoothed and the GPS satellite orbit and clock errors are much larger in the real-time case.

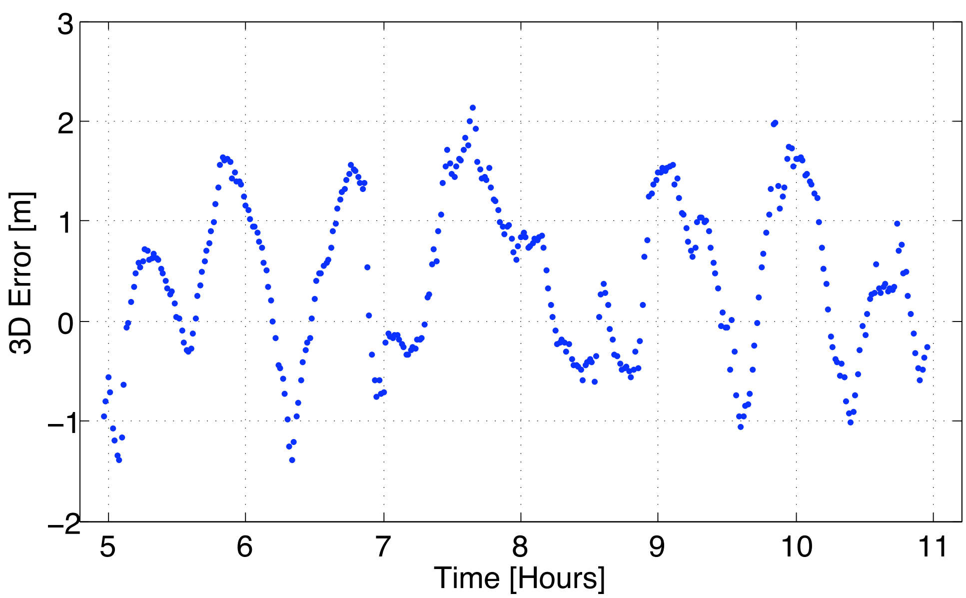


Figure 5.12 Time series of 3D error of a 6-hour interval for 115th day of year 2008 by processing dual-frequency data in real-time using the reduced dynamic technique comparing at 60-second intervals with full dynamics

The 3D standard deviation of the same time interval is plotted in Figure 5.13. The pattern observed in the 3D standard deviation in real-time processing is quite different from the pattern observed in the 3D standard deviation when the data are post-processed. The difference is primarily due to the fact that the data are not smoothed in real-time processing. At the beginning of the interval, the 3D standard deviation starts off as a large value and gradually decreases. The initial large 3D standard deviation values indicate that the solution has been initialized and is converging to the reference state. This re-initialization of the state and gradual convergence is seen many times during the 6-hour interval, occurring after GPS data gaps. When GPS data are available after the data gap, the uncertainty of the solution is large and eventually “settles down” as the real-valued ambiguities are determined and the GPS measurements and dynamics are balanced in the EKF and are in good agreement with each other.

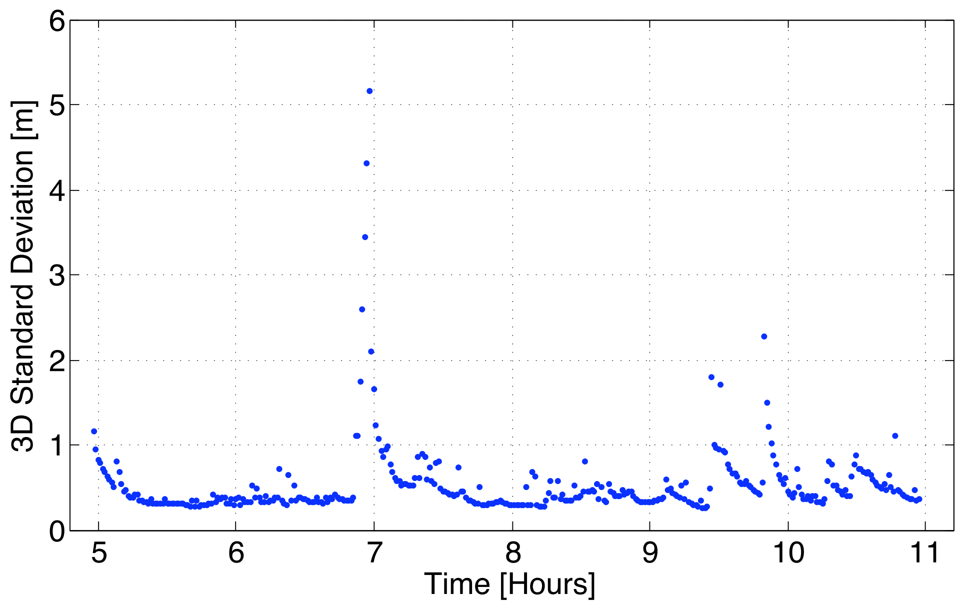


Figure 5.13 3D standard deviation of a 6-hour interval for 115th day of year 2008 by processing dual-frequency data in real-time using the reduced dynamic technique at 60-second intervals with full dynamics

### 5.2.2 Real-Time Dual-Frequency Constrained Solution

This section discusses the results of the real-time dual-frequency solution with a 50% and 25% GPS receiver duty cycle as well as the results of the non-continuous solution for the cases of full dynamics and limited dynamics.

#### *5.2.2.1 Full Dynamics*

With the 100% duty cycle being the reference solution, the results of the constrained continuous solution for the full dynamics case are displayed in Figure 5.14. Except for one out of the 7 days, the pattern is as one would expect. A decrease in the GPS receiver duty cycle suggests a decrease in solution accuracy. The overall accuracy once again is very sensitive to the data quality. A summary of the statistics associated with Figure 5.14 is displayed in Table 5.5. When transitioning from the 100% duty cycle to the 50% duty cycle, a decrease in accuracy of 150% is observed, with an average decrease of 2.0 m. When transitioning from the 100% duty cycle to the 25% duty cycle, a decrease in accuracy of 280% is observed. The real-time, dual-frequency, continuous solution has less of a relative increase in 3D rms in transitioning from the 100% to the 50% and 25% duty cycle with comparison to the post-processed dual-frequency solution. Although the range of the 3D rms is much larger, the real-time dual-frequency 50% and 25% duty cycle cases are suitable for missions that require few metre level accuracy, continuous positioning and do not have the power capacity to have the GPS receiver switched on at all times.

The maximum 3D difference values are shown in Table 5.6. The first point to note is that the maximum values have a much larger range as compared to the post-processing case, because the errors from the GPS satellite orbits and clocks contribute to the erratic behaviour in the presence of the long data gaps. Also, a large role is played by the ability to smooth the data in the post-processing case, which cannot be done in real-time. Thus the amount of divergence from the true position at the end of large data gaps becomes difficult to predict in the real-time case. One calculating a solution in real-time with the 50% or 25% duty cycle can expect 3D differences as large as tens of metres, typically at the end of the large GPS data gaps.

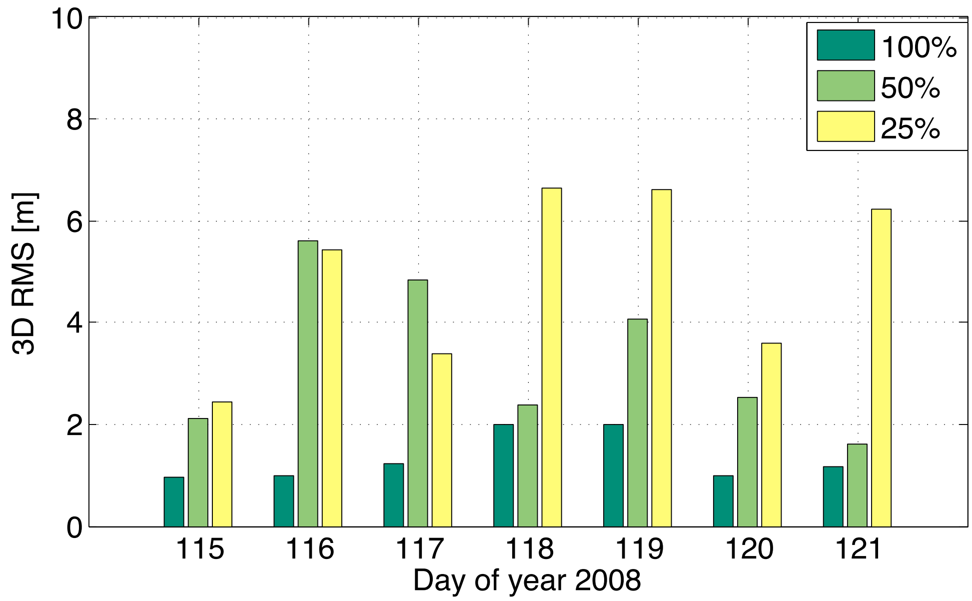


Figure 5.14 3D rms of 6-hour intervals for days 115 – 121 of year 2008 by processing dual-frequency data in real-time using the reduced dynamic technique for a 100%, 50% and 25% duty cycle with full dynamics

| | **100% Duty Cycle** | **50% Duty Cycle** | **25% Duty Cycle** |
|---|---|---|---|
| **3D rms** | 1.3 m | 3.3 m | 4.9 m |
| **% Increase** | -- | 150 % | 280 % |

Table 5.5 Summary statistics of 3D rms of 6-hour intervals for days 115 – 121 of year 2008 by processing dual-frequency data in real-time using the reduced dynamic technique for a 100%, 50% and 25% duty cycle with full dynamics

| | **Day 115** | **Day 116** | **Day 117** | **Day 118** | **Day 119** | **Day 120** | **Day 121** |
|---|---|---|---|---|---|---|---|
| **50%** | 7.8 m | 20 m | 21 m | 8.7 m | 13 m | 13 m | 5.8 m |
| **25%** | 9.5 m | 25 m | 20 m | 28 m | 34 m | 17 m | 39 m |

Table 5.6 Summary statistics of maximum 3D difference of 6-hour intervals for days 115 – 121 of year 2008 by processing dual-frequency data in real-time using the reduced dynamic technique for a 50% and 25% duty cycle with full dynamics

A time series of the real-time dual-frequency solution for the 50% duty cycle case with full dynamics for the 115$^{th}$ of 2008 is presented in Figure 5.15. The beginning and end of the manually created GPS data gaps are clearly visible. Although the full dynamics are being utilized, the large divergences occur because the initial states fed into the dynamic models contain errors associated with the real-time processing.

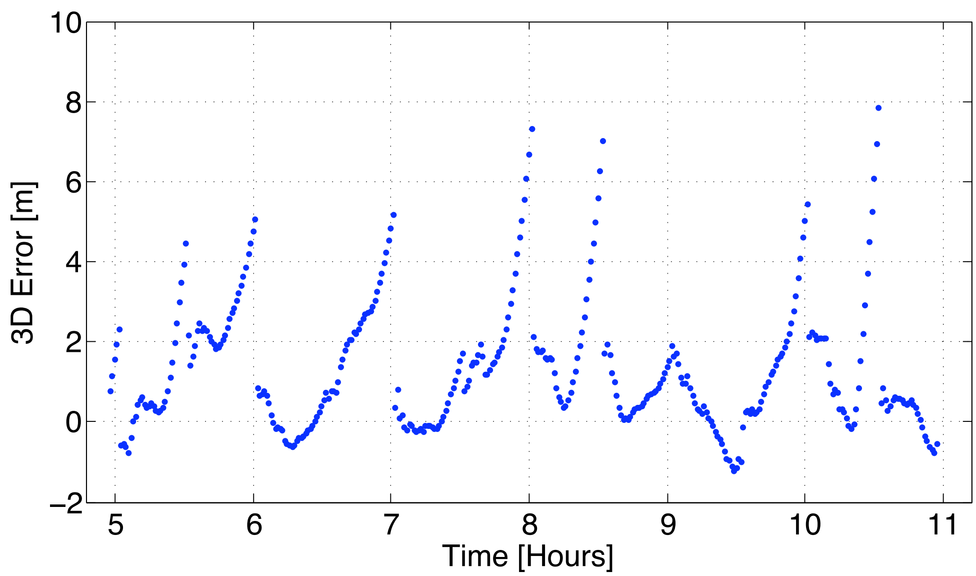


Figure 5.15 Time series of 3D error of a 6-hour interval for 115$^{th}$ day of year 2008 by processing dual-frequency data in real-time using the reduced dynamic technique comparing at 60-second intervals for a 50% duty cycle with full dynamics

The 3D standard deviation of the data set for the same interval is displayed in Figure 5.16. The 3D standard deviation for real-time looks very similar to the individual forward and backward runs in the post-processing case. The values of the 3D standard deviation come out as such when the EKF is tuned to produce the most accurate solution. The large 3D standard deviation indicates the receiver off-times, whereas the lower 3D standard deviation values indicate the receiver on-times. The values observed in the 3D standard deviation are consistent with the position accuracy of the solution.

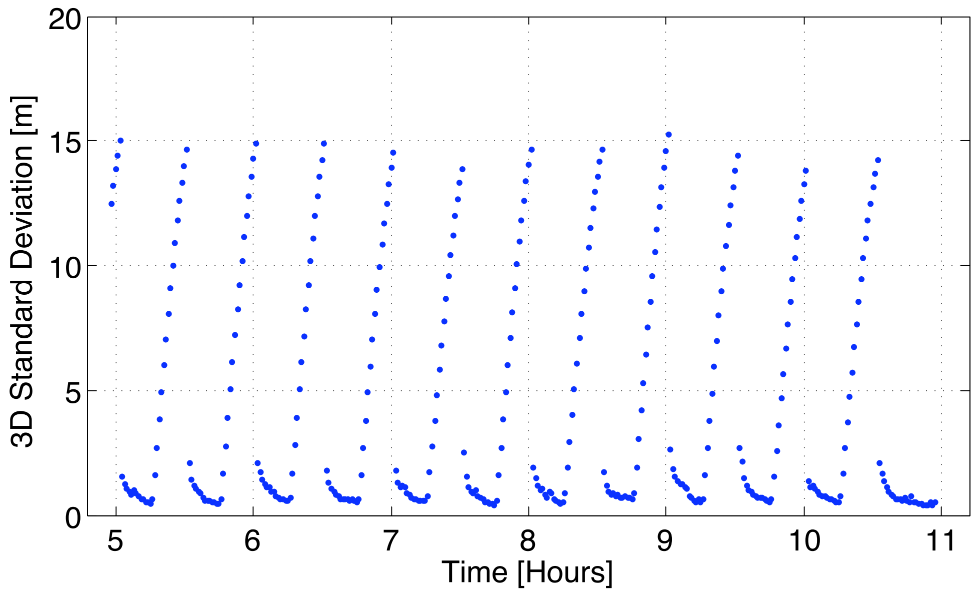


Figure 5.16 3D standard deviation of a 6-hour interval for 115th day of year 2008 by processing dual-frequency data in real-time using the reduced dynamic technique at 60-second intervals for a 50% duty cycle with full dynamics

The results for the real-time, dual-frequency, non-continuous solution are presented in Figure 5.17. In the real-time case, a definite pattern is not present when transitioning from 4 orbits on to 2 orbits on / 2 orbits off to 1 orbit on / 1 orbit off. The 3D rms for the 3 cases is more or less the same. This suggests that leaving the receiver on for longer periods of time when processing in real-time does not guarantee a more accurate convergence to the reference solution. The solution convergence times in real-time are fairly quick, since only a certain degree of accuracy is achieved. The solution thus produces similar accuracy if the receiver is switched on for 4 orbits or switched on for only 1 orbit.

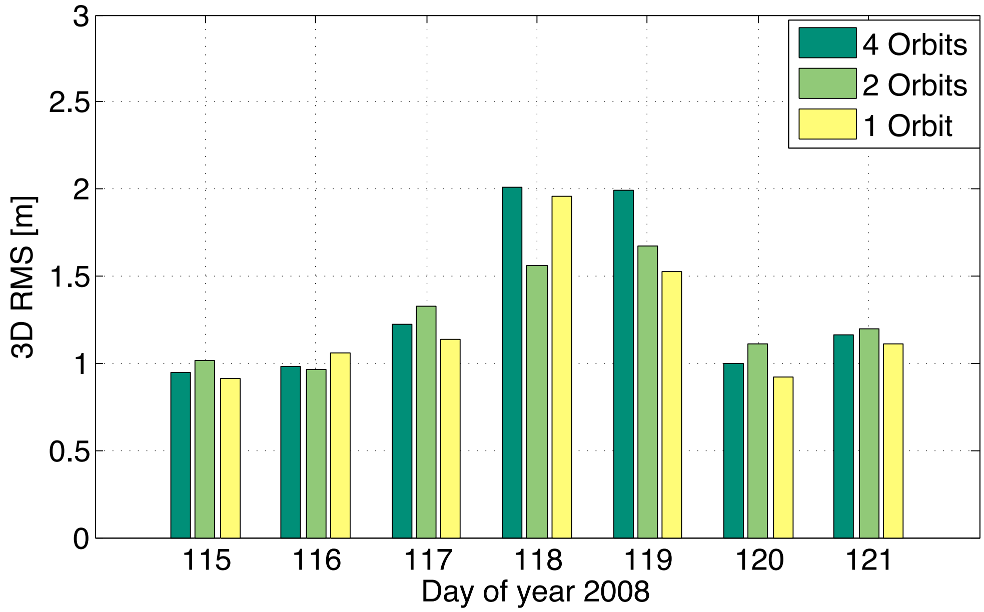


Figure 5.17 3D rms of 6-hour intervals for days 115 – 121 of year 2008 by processing dual-frequency data in real-time using the reduced dynamic technique for a 4 orbits, 2 orbits and 1 orbit on/1 orbit off with full dynamics

#### *5.2.2.2 Limited Dynamics*

The results for the same scenario as above with limited dynamics are displayed in Figure 5.18, with a summary of the statistics associated presented in Table 5.7. The importance of having accurate dynamic models when regularly occurring GPS data gaps of up to 15 minutes are present in the data becomes very apparent. The results for the continuous solution with the 50% and 25% duty cycle show considerable degradations in accuracy in the limited dynamics case when compared to the full dynamics case. The decrease in accuracy when transitioning from the 100% duty cycle to the 50% duty cycle is very large, which is expected because utilizing only the $J_2$ gravitational model to fill in the 15-minute GPS data gaps will cause the solution to diverge very quickly from the reference solution. The $J_2$ gravitational model entails the use of a 2x0 gravity model. The increase from the 50% cycle to the 25% duty is not as large.

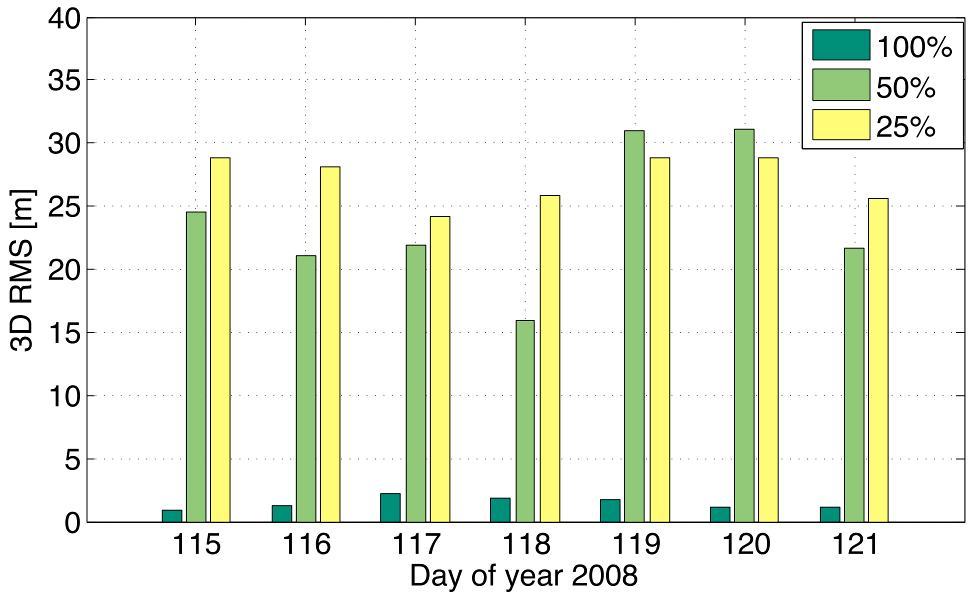


Figure 5.18 3D rms of 6-hour intervals for days 115 – 121 of year 2008 by processing dual-frequency data in real-time using the reduced dynamic technique for a 100%, 50% and 25% duty cycle with limited dynamics

| | **100% Duty Cycle** | **50% Duty Cycle** | **25% Duty Cycle** |
|---|---|---|---|
| **3D rms** | 1.5 m | 24 m | 27 m |
| **% Increase** | -- | 1500 % | 1700 % |

Table 5.7 Summary statistics of 3D rms of 6-hour intervals for days 115 – 121 of year 2008 by processing dual-frequency data in real-time using the reduced dynamic technique for a 100%, 50% and 25% duty cycle with limited dynamics

The maximum values of the 3D difference are displayed in Table 5.8. The maximum error values for the limited dynamics are much higher than the full dynamics case. When utilizing a receiver with the 50% or 25% duty cycle, one can expect 3D errors as large as a couple hundred metres within 15 minutes of a GPS data gap. On average, the maximum error for the 50% and 25% duty is the same. This is expected since the largest error occurs at the end of the 15 minute gaps, which are present in both cases. If the length of the data gap is increased, the maximum 3D error values will be larger.

| | **Day 115** | **Day 116** | **Day 117** | **Day 118** | **Day 119** | **Day 120** | **Day 121** |
|---|---|---|---|---|---|---|---|
| **50%** | 110 m | 86 m | 78 m | 70 m | 190 m | 150 m | 120 m |
| **25%** | 110 m | 120 m | 120 m | 130 m | 130 m | 100 m | 93 m |

Table 5.8 Summary statistics of maximum 3D difference of 6-hour intervals for days 115 – 121 of year 2008 by processing dual-frequency data in real-time using the reduced dynamic technique for a 50% and 25% duty cycle with limited dynamics

The results for the limited dynamics case of the real-time, dual-frequency, non-continuous solution are presented in Figure 5.19. As with the other cases, a definite pattern does not emerge. It can safely be said that the 3D rms for the case of 4 orbits, 2 orbits and 1 orbit is practically the same. Once again, leaving the receiver switched on for many orbits does not prove to provide better accuracy than leaving it on for only one orbit.

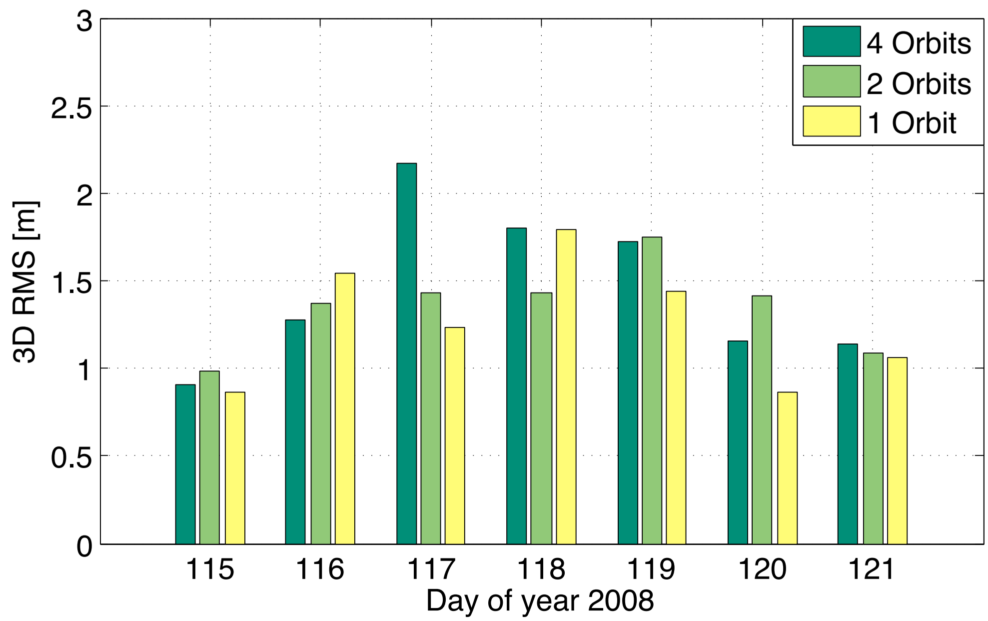


Figure 5.19 3D rms of 6-hour intervals for days 115 – 121 of year 2008 by processing dual-frequency data in real-time using the reduced dynamic technique for a 4 orbits, 2 orbits and 1 orbit on/1 orbit off with limited dynamics

## 5.3 Post-Processed Single-Frequency Solution

The post-processed, single-frequency solution using the GRAPHIC technique is investigated in this section. The availability of only a single-frequency (L1) GPS receiver is simulated by disregarding the L2 measurements from the dual-frequency CHAMP data sets. The results for the reference solution are first presented followed by the various constrained solution results.

### 5.3.1 Post-Processed Single-Frequency Reference Solution

As expected, the single-frequency constrained solution degrades in accuracy when compared to the dual-frequency solution, as shown in Figure 5.20, with the summary statistics displayed in Table 5.9. The results for the single-frequency solution show somewhat less consistency when compared to the dual-frequency solution. This is due to the fact that the GPS solution is based only on the L1 frequency data. It is also much more difficult to determine the float carrier-phase ambiguities with measurements from only one frequency as compared to measurements from two frequencies. The 3D rms of the 7 days for the single-frequency post-processed solution increases from 15 cm to 68 cm, which a decrease of 350% in accuracy as compared to the dual-frequency, post-processed solution. When investigating the 7 days, a range of 29 cm between the minimum and maximum 3D rms values is observed. In the Bock et al. (2008) study, in order to assess the accuracy of the single-frequency solution, the single-frequency results were compared against a dual-frequency solution from the same time period using the GRAPHIC technique with data from GRACE. They able to achieve 3D rms values of 10 cm for single-frequency reduced dynamic orbits with data from the GRACE mission, thus verifying that the GRAPHIC technique is very effective. The solution accuracy of the CHAMP orbit however, tends to be inferior when compared to it GRACE, which is mainly attributed to the lower altitude and large multipath of CHAMP, as well as lower quality GPS measurements. Studies have shown that purely kinematic solutions utilizing GRAPHIC produce 3D rms values of around 1 m using data from CHAMP (Montenbruck, 2003). Due to dynamical aiding, the single-frequency solution determined in this study produces a 3D rms value of 68 cm.

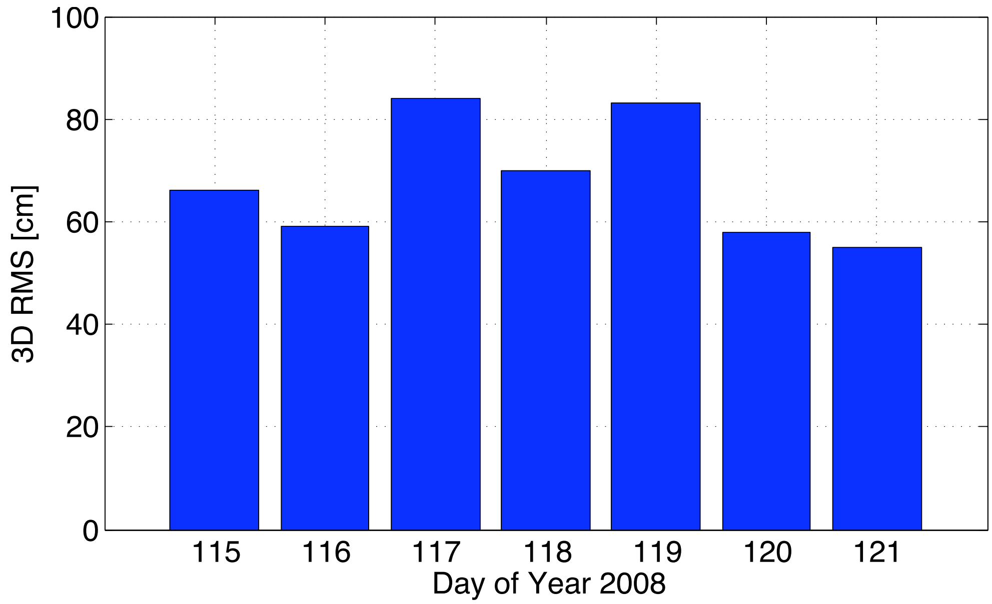


Figure 5.20 3D rms of 6-hour intervals for days 115 – 121 of year 2008 by post-processing single-frequency data using the reduced dynamic technique

| Mean | Std. Dev. | Maximum | Minimum |
|---|---|---|---|
| 68 cm | 12 cm | 84 cm | 55 cm |

Table 5.9 Summary statistics of 3D rms of 6-hour intervals for days 115 – 121 of year 2008 by post-processing single-frequency data using the reduced dynamic technique

There are many reasons why the degradation in accuracy exists in the single-frequency solution when comparing to the dual-frequency solution. If the resolution of the ambiguities is not correct, then the error due to the ionospheric effect will not be fully eliminated. In addition, when GPS satellite geometry changes rapidly, the single-frequency solution quickly degrades. Dynamic modelling does not counteract this effect fully, as the ability to propagate the state accurately relies heavily on the accuracy of the initial state. Single-frequency solutions, in general, are less accurate than their dual-frequency counterparts, hence provide less accurate initial states to the dynamic models, which in turn cause larger divergences during data gaps. Nonetheless, the utilization of a single-frequency receiver allows for less hardware and thus lower power consumption, while maintaining the 3D rms to well within one metre.

### 5.3.2 Post-Processed Single-Frequency Constrained Solution

This section discusses the results of the post-processed single-frequency solution with a 50% and 25% LEO GPS receiver duty cycle, as well as the scenario of the post-processed, single-frequency, non-continuous solution. The reference solution consists of a 100% duty cycle. The 3D rms error results for the continuous solution are presented in Figure 5.21, with a summary of the statistics for the 7 days associated with Figure 5.21 shown in Table 5.10. The results once again are expected and the pattern is similar to that of the dual-frequency post-processed solution. By transitioning from a 100% duty cycle to a 50% duty cycle, the 3D rms increases from 68 cm to 2.9 m, corresponding to a 470% decrease in accuracy. By transitioning from a 100% duty cycle to a 25% duty cycle, the 3D rms increases from 68 cm to 5.5 m, which corresponds to a 710% decrease in accuracy. The degradations in accuracy in the single-frequency solution are much larger than the degradations in accuracy observed in the dual-frequency solution. This difference in accuracy degradation is due partly to the fact that the single-frequency solution produces less accurate initializations to the dynamic models before the GPS data gaps, which in turn causes larger divergences of the solution from the actual position of the LEO during the data gaps.

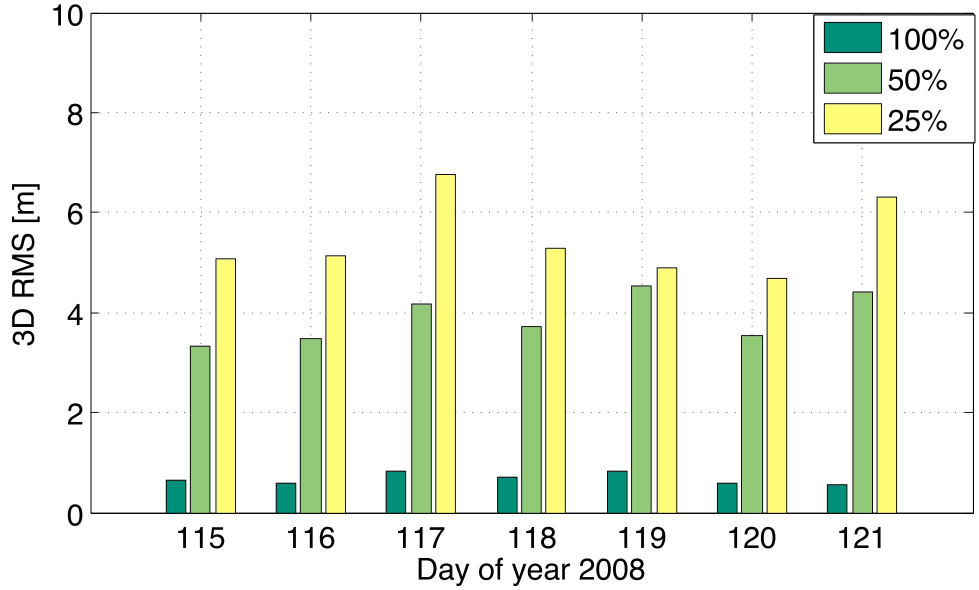


Figure 5.21 3D rms of 6-hour intervals for days 115 – 121 of year 2008 by post-processing single-frequency data using the reduced dynamic technique for a 100%, 50% and 25% duty cycle

| | 100% Duty Cycle | 50% Duty Cycle | 25% Duty Cycle |
|---|---|---|---|
| **3D rms** | 0.68 m | 3.9 m | 5.5 m |
| **% Increase** | -- | 470 % | 710 % |

Table 5.10 Summary statistics of 3D rms of 6-hour intervals for days 115 – 121 of year 2008 by post-processing single-frequency data using the reduced dynamic technique for a 100%, 50% and 25% duty cycle

The maximum 3D difference values are shown in Table 5.11. The range of the maximum values is not as large in the 50% duty cycle case as compared to the 25% duty cycle case, which is once again expected as noticed in the dual-frequency solution. The maximum 3D difference values themselves are however much larger when compared to the dual-frequency case. When using a GPS receiver with the 50% duty cycle that remains on for 15 minutes and off for 15 minutes, one can expect 3D differences as large as 20 m, typically at the end of the 15-minute GPS data gap. For the 25% duty cycle, where the receiver remains on for 5 minutes and remains off for 15 minutes, 3D differences as large as 29 m can arise. These situations are viable for LEO missions that do not require a great deal of accuracy and have a very low power budget.

| | Day 115 | Day 116 | Day 117 | Day 118 | Day 119 | Day 120 | Day 121 |
|---|---|---|---|---|---|---|---|
| **50%** | 15 m | 14 m | 16 m | 18 m | 16 m | 14 m | 20 m |
| **25%** | 26m | 24 m | 27 m | 29 m | 17 m | 17 m | 24 m |

Table 5.11 Summary statistics of maximum 3D difference of 6-hour intervals for days 115 – 121 of year 2008 by post-processing single-frequency data using the reduced dynamic technique for a 50% and 25% duty cycle

The results for post-processed, single-frequency non-continuous solutions for the cases of 4 orbits on, 2 orbits on / 2 orbit off and 1 orbit on / 1 orbit off are presented in Figure 5.22. Much like the dual-frequency case, a definite pattern is not present, meaning that the amount of time that the receiver remains on does not have a large effect on the accuracy of the solution. On average however, the results are analogous to the post-processed dual-frequency results with the 4 orbits accuracy slightly better than the other two cases. The difference between 2 orbits on / 2 orbits off and 1 orbit on / 1 orbit off is minimal. A decrease in accuracy of 8.8% is observed when transitioning from 4 orbits to 2 orbits. This again confirms that the accuracy is similar if the receiver is on for 1 orbit, 2 orbits or 4 orbits. It is useful for missions that have a low power budget. Leaving the receiver switched on for 1 orbit and switching it off for 1 orbit produces solutions almost as accurate as leaving the receiver on for periods as long as 4 orbits, as far as single-frequency receivers are concerned.

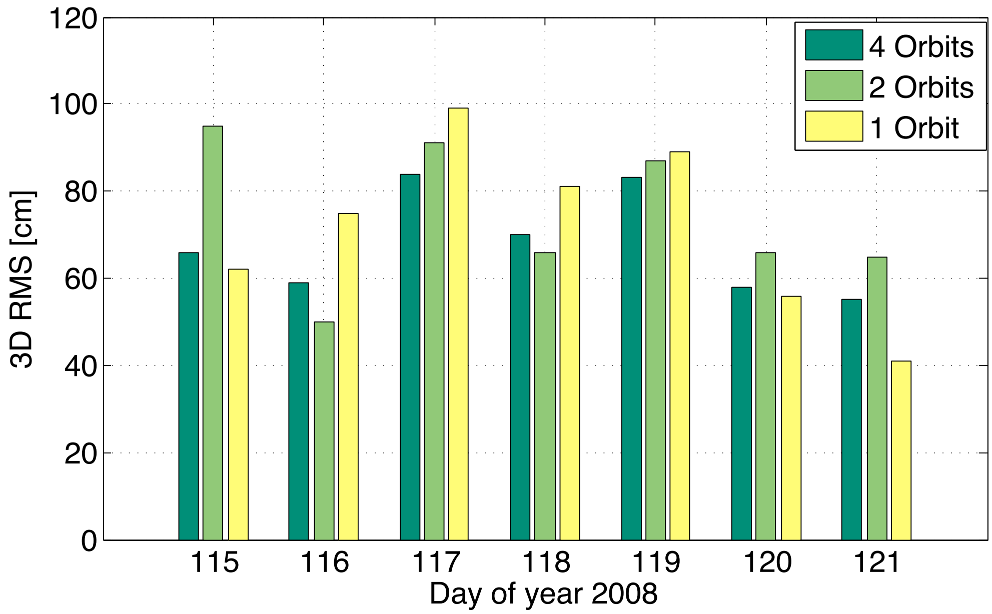


Figure 5.22 3D rms of 6-hour intervals for days 115 – 121 of year 2008 by post-processing single-frequency data using the reduced dynamic technique for a 4 orbits, 2 orbits and 1 orbit on/1 orbit off

## 5.4 Real-Time Single-Frequency Solution

This section discusses the results for the reference solution and the various constrained solutions for real-time, single-frequency processing with both full dynamics and limited dynamics.

### 5.4.1 Real-Time Single-Frequency Reference Solution

The results for the real-time single-frequency solution for both the full dynamics and limited dynamics cases are presented in Figure 5.23. The results for the full and limited dynamics cases are quite similar, suggesting that the improvements made by transitioning from limited to full dynamics are not as large as to offset the degradations in accuracy caused by using data from only one frequency. In other words, the errors introduced by the single-frequency solution cannot be offset by increasing the complexity of the dynamic models.

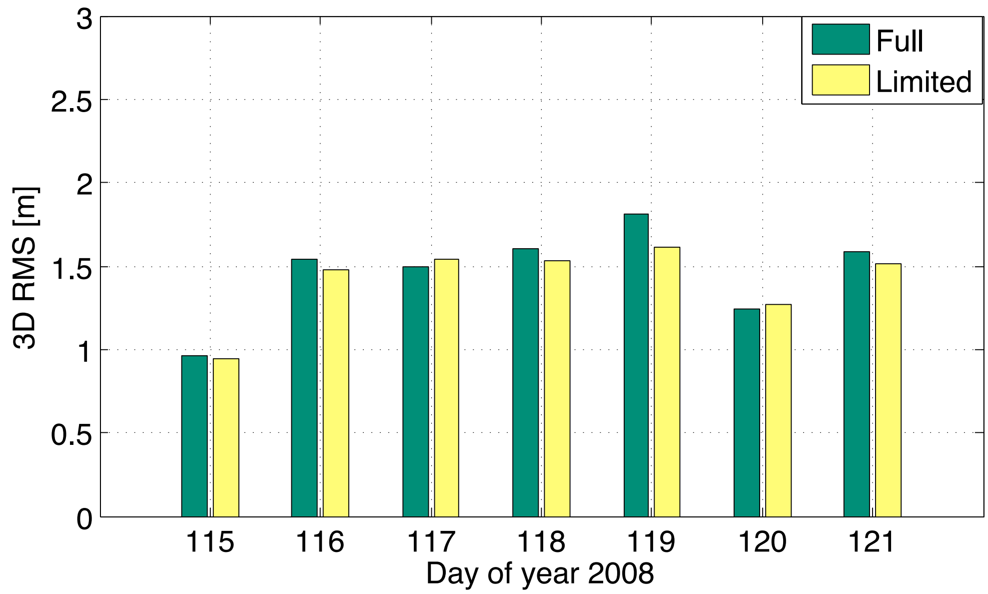


Figure 5.23 3D rms of 6-hour intervals for days 115 – 121 of year 2008 processing single-frequency data in real time using the reduced dynamic technique with full dynamics and limited dynamics

A summary of the statistics associated with Figure 5.23 is presented in Table 5.12. The results for the full and limited dynamics are practically the same. Slight improvements in the limited dynamics case are due to the change in the residual and covariance cutoff values. One can argue that if the cutoff values used in the limited dynamics case were to be applied to the full dynamics case, the full dynamics case would show better results. Although this may be the case, the cut off values in the full dynamics case are left unchanged, so that an accurate comparison with the dual-frequency case can be made. When looking at the full dynamics case, a decrease in accuracy of 15% is observed when transitioning from dual-frequency to single-frequency in real-time. This suggests that the degradation in accuracy when transitioning from dual-frequency to single-frequency in real-time is not as large as observed in the post-processing case.

| | Mean | Std. Dev. | Maximum | Minimum |
|---|---|---|---|---|
| **Full Dynamics** | 1.5 m | 0.28 m | 1.8 m | 0.96 m |
| **Limited Dynamics** | 1.4 m | 0.23 m | 1.6 m | 0.94 m |

Table 5.12 Summary statistics of 3D rms of 6-hour intervals for days 115 – 121 of year 2008 by processing single-frequency data in real-time using the reduced dynamic technique with full dynamics and limited dynamics

Thus, if a mission requires real-time processing, a single-frequency receiver would produce a solution with nearly the same accuracy as a solution using dual-frequency data. This once again leads to the fact that the increase in accuracy when transitioning from a single-frequency receiver to a dual-frequency receiver does not fully offset the errors associated with real-time processing.

### 5.4.2 Real-Time Single-Frequency Constrained Solution

This section discusses the real-time, single-frequency continuous solution with both full dynamics and limited dynamics.

#### *5.4.2.1 Full Dynamics*

The results for the real-time, single-frequency, continuous solution with full dynamics are displayed in Figure 5.24. The results are once again as expected, with a decrease in accuracy when processing in real-time being significantly larger when transitioning from the 100% duty cycle to the 50% and 25% duty cycles.

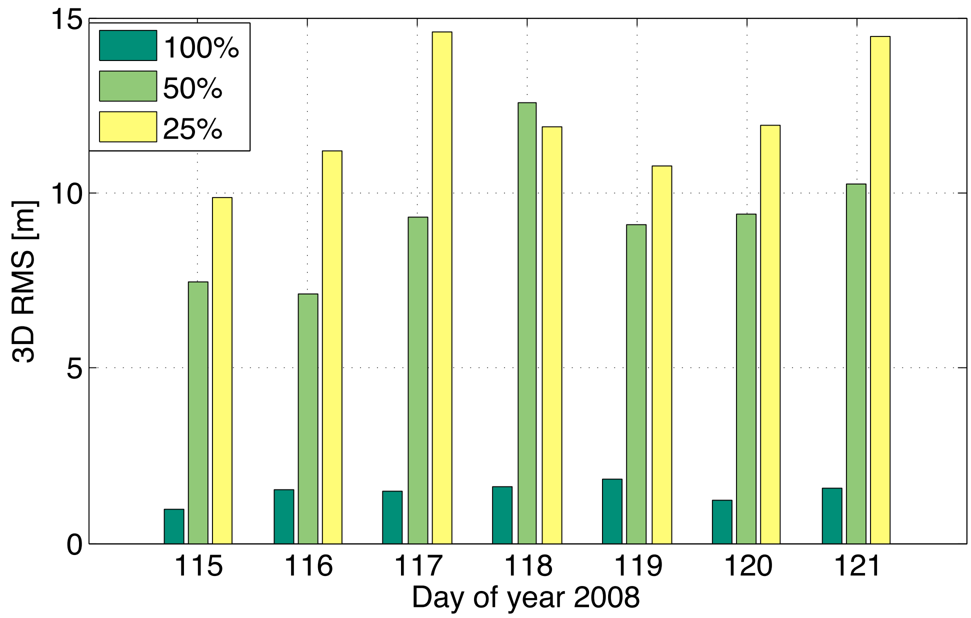


Figure 5.24 3D rms of 6-hour intervals for days 115 – 121 of year 2008 by processing single-frequency data in real-time using the reduced dynamic technique for a 100%, 50% and 25% duty cycle with full dynamics

A summary of the statistics associated with Figure 5.24 is shown in Table 5.13. The degradations in accuracy seen in the real-time single-frequency solution are much greater than those observed in the real-time dual-frequency case. This once again has to do with the initial states provided to the dynamic models to manage the 15-minute GPS data gaps. As one would expect, the initial states provided by the single-frequency solution are less accurate than those provided by the dual-frequency solution. The divergence from the true solution during the large data gaps is thus much larger in the single-frequency solution as compared to the dual-frequency solution. The 3D rms increases to 9.3 m from 1.5 m when utilizing a receiver with a 50% duty cycle, corresponding to a 520% decrease in accuracy. When the receiver has a 25% duty cycle, the 3D rms increases to 12 m, indicating a 700% decrease in accuracy.

| | 100% Duty Cycle | 50% Duty Cycle | 25% Duty Cycle |
|---|---|---|---|
| **3D rms** | 1.5 m | 9.3 m | 12 m |
| **% Increase** | -- | 520 % | 700 % |

Table 5.13 Summary statistics of 3D rms of 6-hour intervals for days 115 – 121 of year 2008 by processing single-frequency data in real-time using the reduced dynamic technique for a 100%, 50% and 25% duty cycle with full dynamics

The maximum 3D difference values are displayed in Table 5.14. The maximum values observed in the real-time single-frequency case are much larger than its dual-frequency counterpart, as expected. For a LEO carrying a single-frequency receiver with a 50% or 25% duty cycle with data gaps of up to 15 minutes, one can expect the maximum 3D difference to be in the tens of metres. This is suitable for a mission in which a real-time solution is required, but with a low power and cost budget.

| | Day 115 | Day 116 | Day 117 | Day 118 | Day 119 | Day 120 | Day 121 |
|---|---|---|---|---|---|---|---|
| **50%** | 34 m | 29 m | 54 m | 71 m | 40 m | 51 m | 55 m |
| **25%** | 37 m | 56 m | 59 m | 67 m | 49 m | 36 m | 66 m |

Table 5.14 Summary statistics of maximum 3D difference of 6-hour intervals for days 115 – 121 of year 2008 by processing single-frequency data in real-time using the reduced dynamic technique for a 50% and 25% duty cycle with full dynamics

The results for the real-time, single-frequency, non-continuous solution with full dynamics are presented in Figure 5.25. The results once again show no definite pattern. Since this is the real-time case, these results are expected. As it turns out, the mean 3D rms for all cases is almost the same. These results are not surprising as the results for the three cases of 4 orbits, 2 orbits and 1 orbit were very similar in the dual-frequency case as well. In addition, the results show that the solution accuracy for the single-frequency case is slightly lower than the dual-frequency case when processing in real-time.

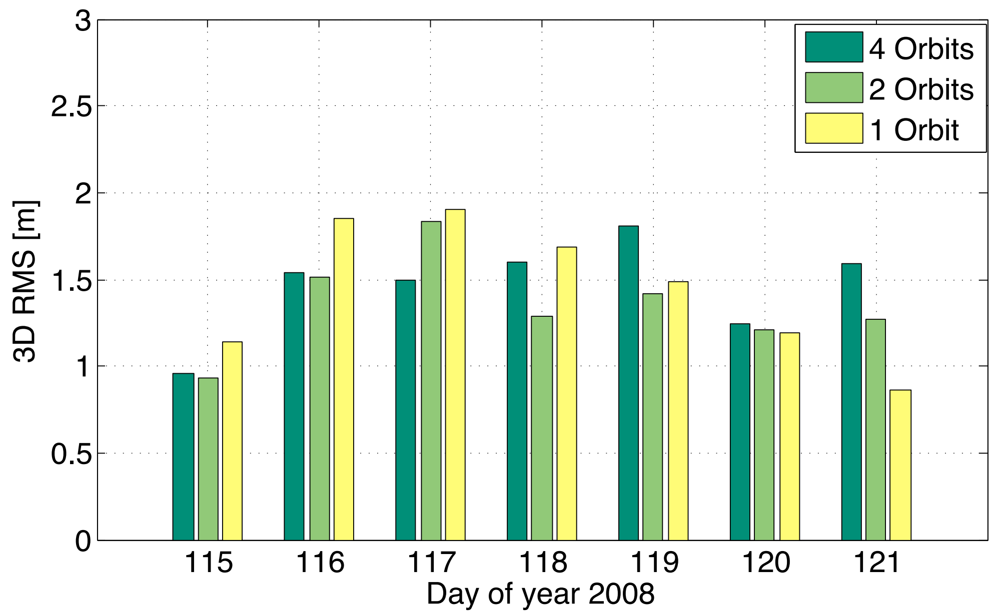


Figure 5.25 3D rms of 6-hour intervals for days 115 – 121 of year 2008 by processing single-frequency data in real-time using the reduced dynamic technique for a 4 orbits, 2 orbits and 1 orbit on/1 orbit off for full dynamics

#### *5.4.2.2 Limited Dynamics*

The results for the real-time, single-frequency, continuous solution with limited dynamics are displayed in Figure 5.26, with a summary of the statistics presented in Table 5.15. Although the difference between the 100% duty cycle and the 50% duty cycle is very large, the difference between the 50% duty cycle and the 25% duty is not so large. The difference that does exist between the 50% duty cycle and 25% duty has to do with the fact that there are more GPS data available in the 50% duty cycle case. The length of the GPS data gaps is the same in both cases: 15-minutes. Thus the contribution made to the large 3D rms values by the diverging solution during the data gaps is about the same in the 50% and 25% duty cycle cases. The increases in the 3D rms for the 50% and 25%

duty cycle as compared to the 100% duty cycle are very large. As before, the importance of the dynamic models is realized with the presence of large GPS data gaps.

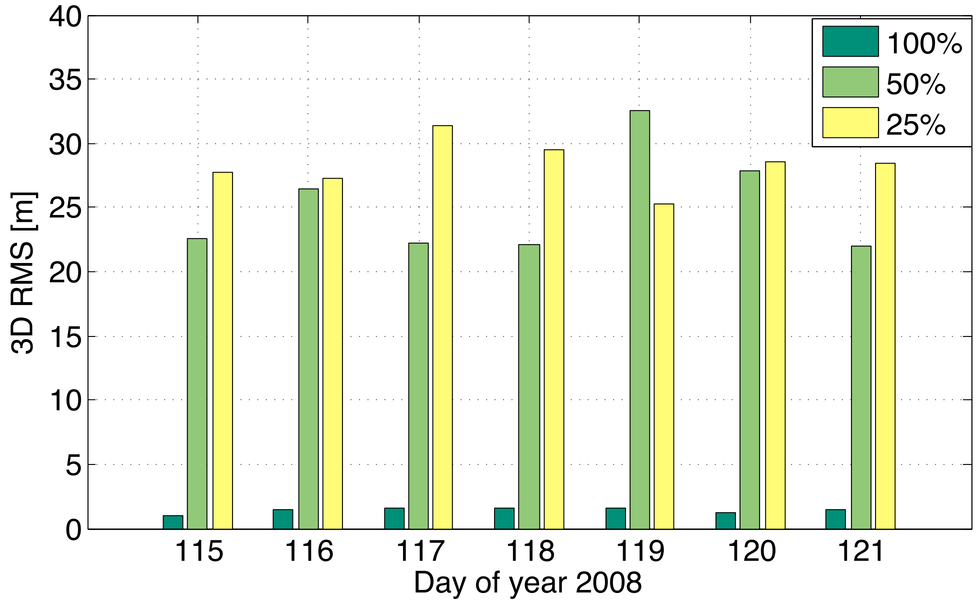


Figure 5.26 3D rms of 6-hour intervals for days 115 – 121 of year 2008 by processing single-frequency data in real-time using the reduced dynamic technique for a 100%, 50% and 25% duty cycle with limited dynamics

| | **100% Duty Cycle** | **50% Duty Cycle** | **25% Duty Cycle** |
|---|---|---|---|
| **3D rms** | 1.4 m | 25 m | 28 m |
| **% Increase** | -- | 1700 % | 1900 % |

Table 5.15 Summary statistics of 3D rms of 6-hour intervals for days 115 – 121 of year 2008 by processing single-frequency data in real-time using the reduced dynamic technique for a 100%, 50% and 25% duty cycle with limited dynamics

The maximum 3D differences are presented in Table 5.16. The maximum error values approach hundreds of metres in the single-frequency limited dynamics case. These values are much larger than the real-time, single-frequency full dynamics case and slightly larger than the real-time, dual-frequency, limited dynamics case.

| | Day 115 | Day 116 | Day 117 | Day 118 | Day 119 | Day 120 | Day 121 |
|---|---|---|---|---|---|---|---|
| **50%** | 85 m | 140 m | 90 m | 94 m | 200 m | 150 m | 118 m |
| **25%** | 120 m | 100 m | 130 m | 130 m | 120 m | 110 m | 120 m |

Table 5.16 Summary statistics of maximum 3D difference of 6-hour intervals for days 115 – 121 of year 2008 by processing single-frequency data in real-time using the reduced dynamic technique for a 50% and 25% duty cycle with limited dynamics

The results for the real-time, single-frequency, non-continuous solution with limited dynamics are presented in Figure 5.27. The results for the limited dynamics case are almost exactly the same as for the full dynamics case. This suggests that increasing the complexity of the dynamic models does not necessarily produce a more accurate solution in the real-time, single-frequency case. Thus for a mission that has a low power budget and a single-frequency receiver, it would be more viable to work with just the $J_2$ gravitational model rather than the full dynamics.

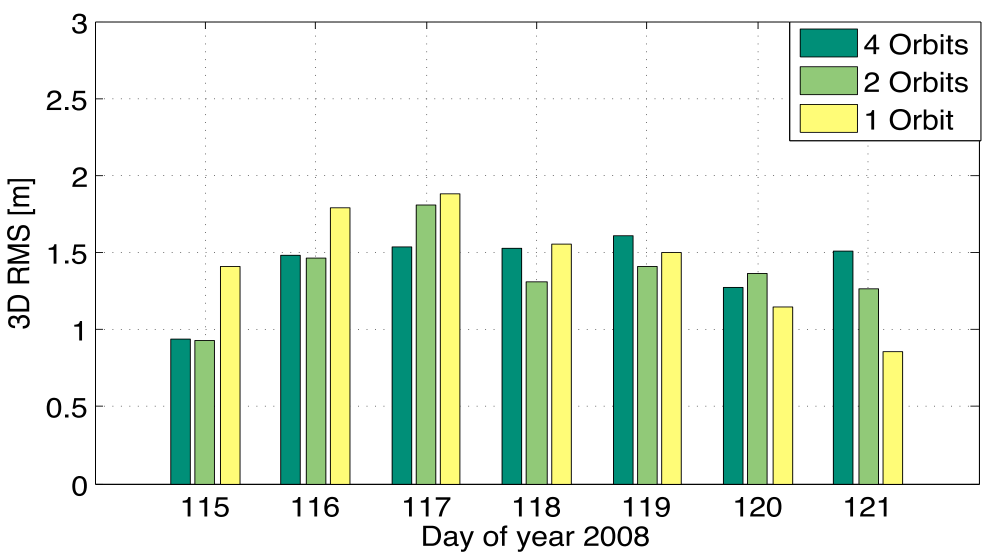


Figure 5.27 3D rms of 6-hour intervals for days 115 – 121 of year 2008 by processing single-frequency data in real-time using the reduced dynamic technique for a 4 orbits, 2 orbits and 1 orbit on/1 orbit off for limited dynamics

# Chapter 6

# 6 Extremely Constrained Orbit Solution Experiments

In this chapter, solutions with a very low GPS receiver duty cycle are investigated. The receiver is simulated to be switched on for 10 minutes and switched off for 80 minutes with the dynamic models filling in for the 80 minute GPS data gaps, thus producing a continuous solution with an 11% receiver duty cycle. A 90 minute orbit is typical for a LEO altitude. This scenario is possible in missions involving nanosatellites with power budgets that are insufficient to power the GPS receiver for long periods of time, due to limited power generation and use of power by other payloads such as cameras or other types of detectors, particularly in science missions. All the solution results are compared against the reference solution, as described in Section 2.9.

## 6.1 Post-Processed Dual-Frequency Solution

The results for the post-processed, dual-frequency solution with the GPS receiver simulated to be switched on for 10 minutes and switched off for 80 minutes are presented in Figure 6.1, with a summary shown in Table 6.1. The range of the 3D rms is very large, as compared to previous results. The extremely large GPS data gaps produce highly unpredictable behaviour. The 3D rms ranges from 2.9 m to 16 m with an average of

9.6 m for the 7 days. The 3D rms of the solution in this case is basically reliant on the performance of the dynamic models during the GPS data gaps. Although the dynamic models may carry excellent accuracy, the overall ability of the dynamic models to maintain an accurate solution depends a great deal on the initial state. An inaccurate initialization to the dynamic models will cause a large divergence from the true solution during the data gap.

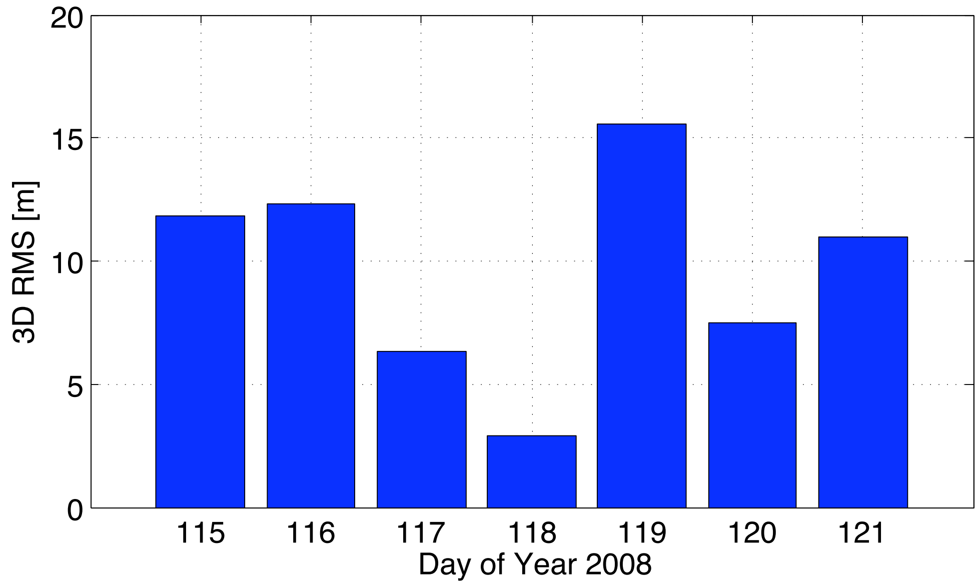


Figure 6.1 3D rms of 6-hour intervals for days 115 – 121 of year 2008 by post-processing dual-frequency data using the reduced dynamic technique for an 11% duty cycle

| Mean | Std. Dev. | Maximum | Minimum |
|---|---|---|---|
| 9.6 m | 4.3 m | 16 m | 2.9 m |

Table 6.1 Summary statistics of 3D rms of 6-hour intervals for days 115 – 121 of year 2008 by post-processing dual-frequency data using the reduced dynamic technique for an 11% duty cycle

The maximum values of the 3D difference are presented in Table 6.2. Although the maximum error values may seem very large, the results are quite impressive considering that the GPS receiver is switched off for such a large part of the orbit. Once again, there is quite a large range in the maximum 3D error values. These results suggest that for a dual-frequency receiver where a continuous solution is required, the maximum divergence from the true solution at the end of an 80-minute data gap one can expect is less than 50 m.

| | **Day 115** | **Day 116** | **Day 117** | **Day 118** | **Day 119** | **Day 120** | **Day 121** |
|---|---|---|---|---|---|---|---|
| **11%** | 33 m | 38 m | 27 m | 8.5 m | 46 m | 21 m | 27 m |

Table 6.2 Summary statistics of maximum 3D difference of 6-hour intervals for days 115 – 121 of year 2008 by post-processing dual-frequency data using the reduced dynamic technique for an 11% duty cycle

A time series of the 3D difference for day 115 of 2008 is shown in Figure 6.2. There are a few points to be noted here. The performance of the forward run is much better than the backward run. The divergence during the data gaps from the true solution in the forward run is not as large as that seen in the backward run. This is due to the poor initial state that is fed into the dynamic models in order to propagate the solution across the GPS data gaps during the backward run. The large divergences in the backward solution cause the smoothed solution to diverge as well. Day 115 is one of the worst days out of the 7 in terms of accuracy, so encountering the large divergence as seen in Figure 6.2 are not very common. The initializations of the dynamic models are typically accurate and the divergences from the true solution are not as large. Another point to note is that the solution for the last one hour is missing, as there is no GPS data available to initiate the backward run at the end of the 6-hour interval. The reason for the missing GPS data at the end of the interval is because that epoch occurs during the time that the receiver is switched off. Initializing from the dynamic solution when it has already diverged significantly from the true solution will heavily skew the results. Hence, the solution is only available for an interval that is less than 6 hours.

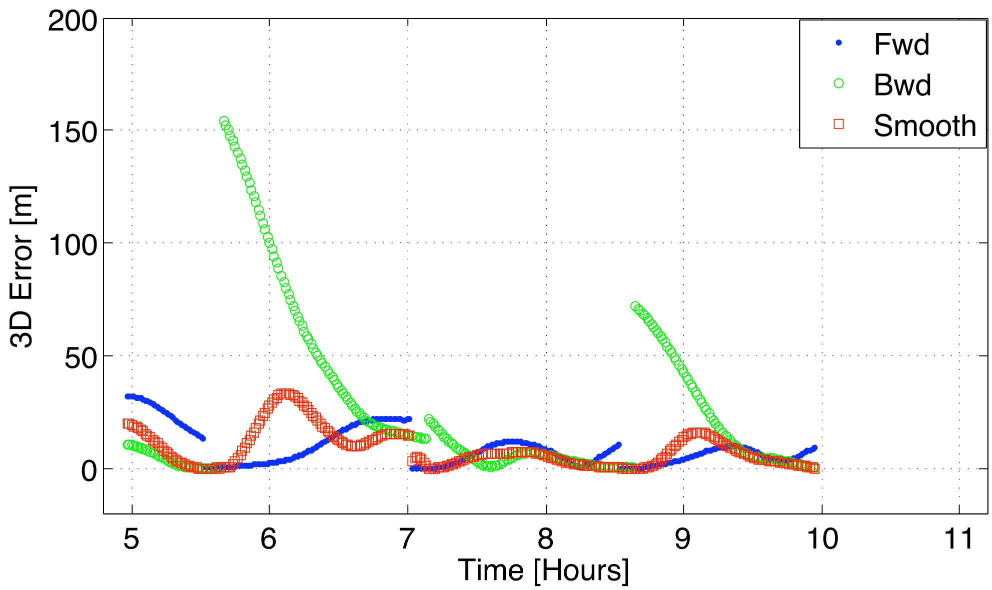


Figure 6.2 Time series of 3D error of a 6-hour interval for 115$^{th}$ day of year 2008 by post-processing dual-frequency data using the reduced dynamic technique comparing at 60-second intervals for an 11% duty cycle

The 3D standard deviation for the same interval of day 115 of 2008 is displayed in Figure 6.3. As before, the 3D standard deviation values for the individual forward run and backward run are much larger as compared to the 3D standard deviation values for the smoothed solution. The forward and backward 3D standard deviation values reach as high as ~80 m whereas they only reach as high as ~40 m for the smoothed solution. Once again, these values are consistent with what is observed in the position error.

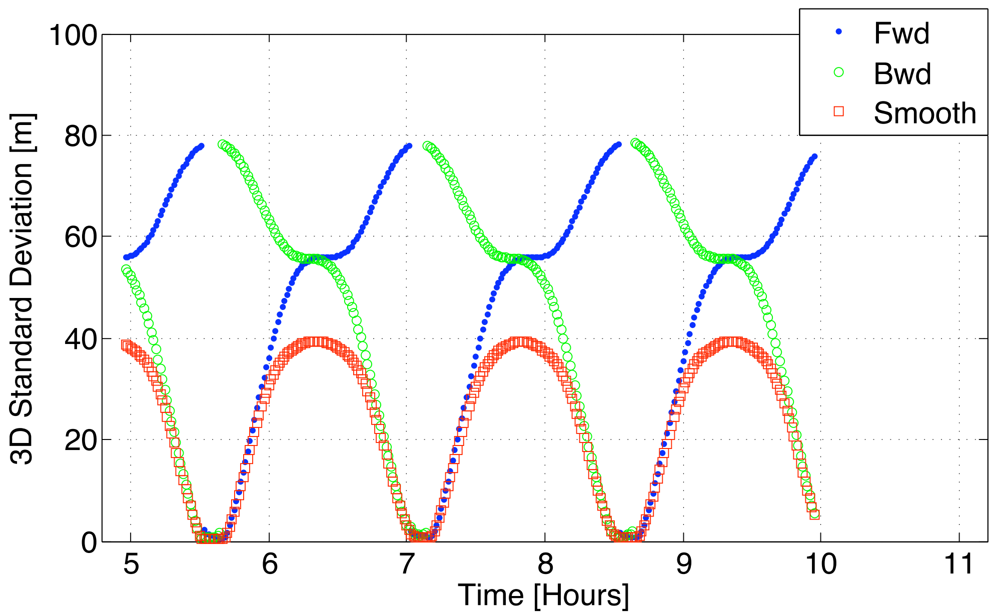


Figure 6.3 3D standard deviation of a 6-hour interval for 115th day of year 2008 by post-processing dual-frequency data using the reduced dynamic technique at 60-second intervals for an 11% duty cycle

## 6.2 Real-Time Dual-Frequency Solution

This section presents the results for the real-time, dual-frequency, continuous solution for the 11% duty cycle with both full and limited dynamics.

### 6.2.1 Full Dynamics

The real-time, dual-frequency solution with the utilization of full dynamics is discussed in this section. The results for the 3D rms error are presented in Figure 6.4. As expected, the range of the results is quite large with a mean 3D rms of tens of metres. A summary of the statistics is shown in Table 6.3. Although the solution is not smoothed, the real-time results are fairly accurate considering the presence of such large data gaps.

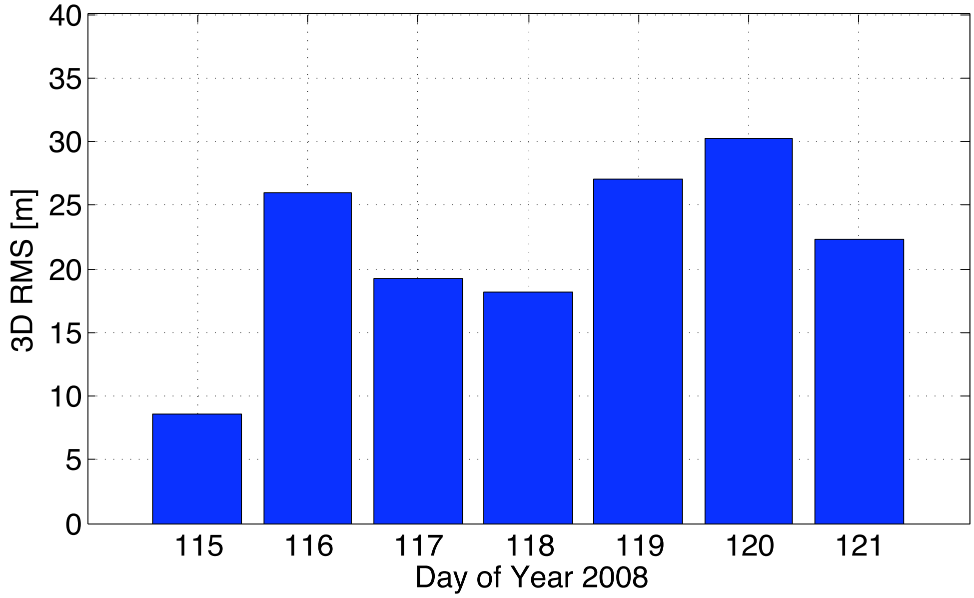


Figure 6.4 3D rms of 6-hour intervals for days 115 – 121 of year 2008 by processing dual-frequency data in real-time using the reduced dynamic technique for an 11% duty cycle with full dynamics

| **Mean** | **Std. Dev.** | **Maximum** | **Minimum** |
|---|---|---|---|
| 22 m | 7.2 m | 30 m | 8.6 m |

Table 6.3 Summary statistics of 3D rms of 6-hour intervals for days 115 – 121 of year 2008 by processing dual-frequency data in real-time using the reduced dynamic technique for an 11% duty cycle with full dynamics

The maximum 3D difference values are displayed in Table 6.4. It is quite impressive to observe that the maximum error one would encounter in this scenario is only 96 m. This scenario is viable for small nanosatellite missions with a very low power budget that require a continuous solution in real-time.

| | **Day 115** | **Day 116** | **Day 117** | **Day 118** | **Day 119** | **Day 120** | **Day 121** |
|---|---|---|---|---|---|---|---|
| **11%** | 26 m | 76 m | 48 m | 65 m | 63 m | 96 m | 79 m |

Table 6.4 Summary statistics of maximum 3D difference of 6-hour intervals for days 115 – 121 of year 2008 by processing dual-frequency data in real-time using the reduced dynamic technique for an 11% duty cycle with full dynamics

A 3D difference time series of the dual-frequency real-time case for day 115 of 2008 is presented in Figure 6.5. Almost the entire solution is based on the dynamic models. Every 80 minutes, the GPS data are recorded for 10 minutes and the solution is brought back closer to the true solution. Once the receiver switches off, the dynamics take over and the solution begins to diverge from the true solution.

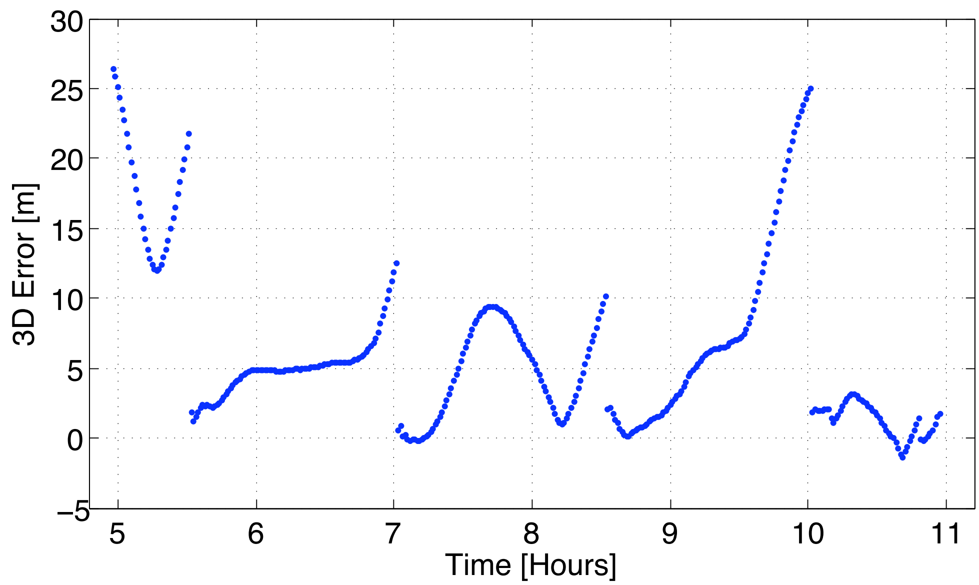


Figure 6.5 Time series of 3D error of a 6-hour interval for 115$^{th}$ day of year 2008 by processing dual-frequency data in real-time using the reduced dynamic technique comparing at 60-second intervals for an 11% duty cycle with full dynamics

The 3D standard deviation of the same interval is displayed in Figure 6.6. It is clear when the GPS receiver is switched off and when it is switched back on. When dynamic models are providing the solution, the 3D standard deviation continues to rise. Once the GPS data become available again, the 3D standard deviation quickly drops back to a lower value. The reason for the sharp drops in the 3D standard deviation after the availability of the GPS data is due to the covariance cutoffs that are in place. If the 3D standard deviation is above a certain empirically determined value when the GPS data becomes available again, the dynamics will be used to propagate the state further. As soon as the GPS solution converges to a desirable accuracy and the 3D standard deviation drops below a certain level, the GPS plus dynamics solution is then kept. This prevents the occurrence of extremely inaccurate initializations from the GPS measurements after the availability of the GPS data.

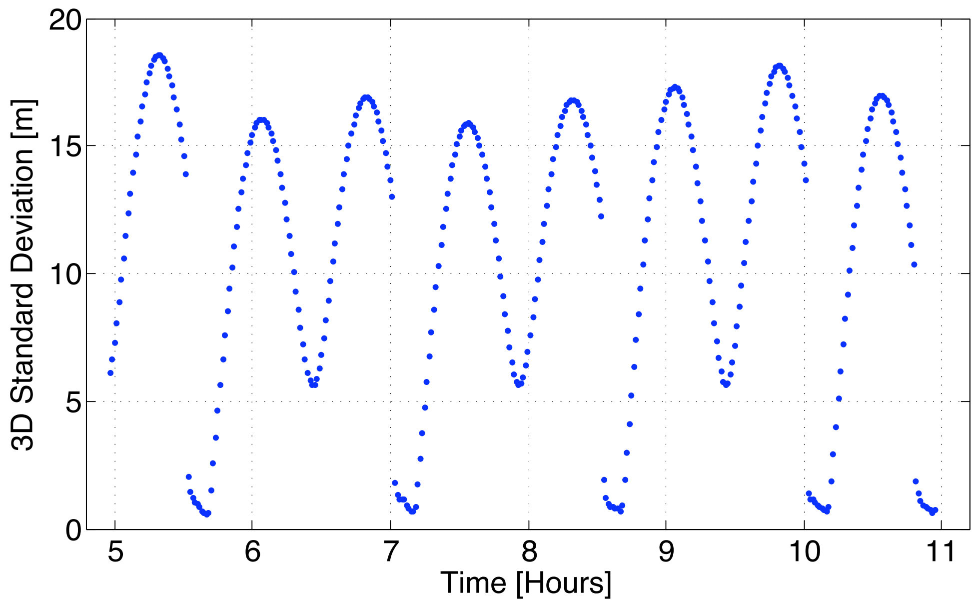


Figure 6.6 3D standard deviation of a 6-hour interval for 115th day of year 2008 by processing dual-frequency data in real-time using the reduced dynamic technique at 60-second intervals for an 11% duty cycle with full dynamics

### 6.2.2 Limited Dynamics

The results for the dual-frequency real-time continuous solution with limited dynamics are displayed in Figure 6.7. As expected, the decrease in accuracy when going from full dynamics to limited dynamics is very large. The 3D rms values now range in the hundreds of metres, instead of tens of metres, as was the case with full dynamics.

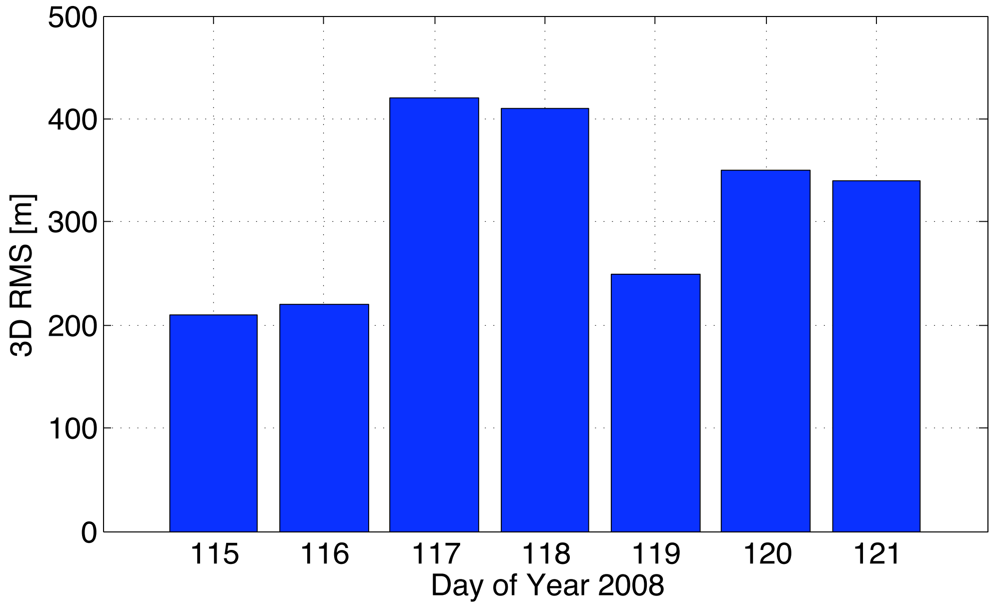


Figure 6.7 3D rms of 6-hour intervals for days 115 – 121 of year 2008 by processing dual-frequency data in real-time using the reduced dynamic technique for an 11% duty cycle with limited dynamics

A summary of the statistics associated with Figure 6.7 is shown in Table 6.5. The difference in the mean 3D rms for the 7 days between the full dynamics and limited dynamics cases is about 300 m. When trying to cover large GPS data gaps, it is thus very crucial that the dynamic models are accurate and complete. Otherwise, the accuracy of the solution is considerably degraded.

| **Mean** | **Std. Dev.** | **Maximum** | **Minimum** |
|---|---|---|---|
| 314 m | 88 m | 420 m | 210 m |

Table 6.5 Summary statistics of 3D rms of 6-hour intervals for days 115 – 121 of year 2008 by processing dual-frequency data in real-time using the reduced dynamic technique for an 11% duty cycle with limited dynamics

The maximum 3D differences are displayed in Table 6.6. The maximum error values now approach 1 km. This mission scenario cannot be used for orbit specification requiring highly accurate solutions. During the GPS data gaps when the receiver is switched off, the divergence from the reference solution is 0.5 to 1 km (3D).

| | **Day 115** | **Day 116** | **Day 117** | **Day 118** | **Day 119** | **Day 120** | **Day 121** |
|---|---|---|---|---|---|---|---|
| **11%** | 590 m | 440 m | 1000 m | 1000 m | 680 m | 1000 m | 730 m |

Table 6.6 Summary statistics of maximum 3D difference of 6-hour intervals for days 115 – 121 of year 2008 by processing dual-frequency data in real-time using the reduced dynamic technique for an 11% duty cycle with limited dynamics

## 6.3 Post-Processed Single-Frequency Solution

The results for the post-processed, single-frequency solution are presented in Figure 6.8. As with the dual-frequency case, the range of the 3D rms values in the 7 days is quite large. The 3D rms values themselves are actually much higher in the single-frequency case as compared to the dual-frequency case when post-processing the data.

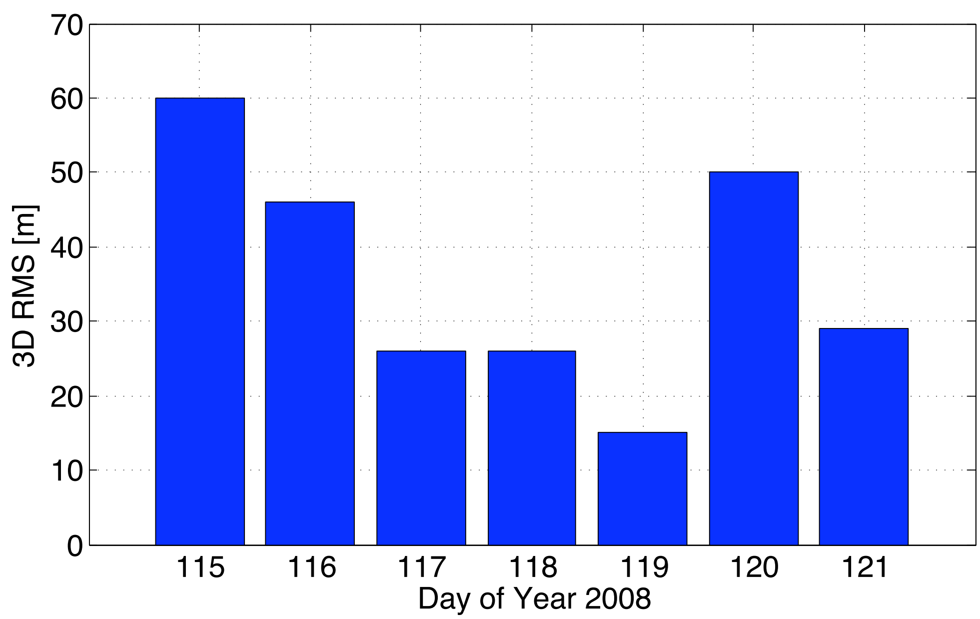


Figure 6.8 3D rms of 6-hour intervals for days 115 – 121 of year 2008 by post-processing single-frequency data using the reduced dynamic technique for an 11% duty cycle

A summary of the statistics is presented in Table 6.7. When going from a dual-frequency receiver to a single-frequency receiver with the 11% duty cycle for post-processing, a decrease of 260% in the accuracy of the solution is observed. Due to the inaccurate initializations to the dynamic models prior to the GPS data gaps, the divergence from the true solution during the GPS receiver off-times becomes quite large.

| Mean | Std. Dev. | Maximum | Minimum |
|---|---|---|---|
| 36 m | 16 m | 60 m | 15 m |

Table 6.7 Summary statistics of 3D rms of 6-hour intervals for days 115 – 121 of year 2008 by post-processing single-frequency data using the reduced dynamic technique for an 11% duty cycle

The maximum 3D difference values are shown in Table 6.8. Following the trend, as the 3D rms results for the continuous solution become larger, the range of the maximum values becomes larger as well. A large 3D rms value does not only suggest lower accuracy levels, but more erratic behaviour of the solution as well.

| | Day 115 | Day 116 | Day 117 | Day 118 | Day 119 | Day 120 | Day 121 |
|---|---|---|---|---|---|---|---|
| **11%** | 190 m | 120 m | 63 m | 53 m | 36 m | 180 m | 78 m |

Table 6.8 Summary statistics of maximum 3D difference of 6-hour intervals for days 115 – 121 of year 2008 by post-processing single-frequency data using the reduced dynamic technique for an 11% duty cycle

Thus for a mission with an extremely low power budget devoted to the single-frequency GPS receiver, one can expect errors as large as 190 m when leaving the receiver switched on for 10 minutes and switched off for 80 minutes.

## 6.4 Real-Time Single-Frequency Solution

This section presents the results for the real-time, single-frequency continuous solution for the 11% duty cycle with both full and limited dynamics.

### 6.4.1 Full Dynamics

The results for the real-time, single-frequency solution with full dynamics are presented in Figure 6.9 with the associated summary of statistics in Table 6.9. The 3D rms is about an order of magnitude larger with the single-frequency receiver as compared to the dual-frequency receiver when processing in real-time with full dynamics. Just as before, the range of the 3D rms values is quite large. This suggests that the single-frequency solution is less accurate and more erratic as compared to the dual-frequency solution.

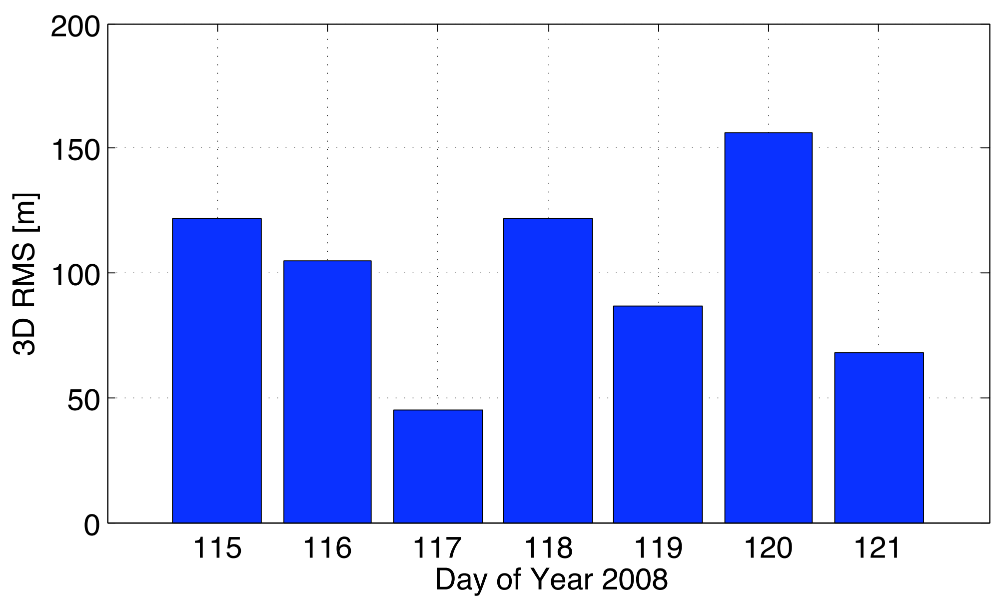


Figure 6.9 3D rms of 6-hour intervals for days 115 – 121 of year 2008 by processing single-frequency data in real-time using the reduced dynamic technique for an 11% duty cycle with full dynamics

| Mean | Std. Dev. | Maximum | Minimum |
|---|---|---|---|
| 100 m | 37 m | 160 m | 45 m |

Table 6.9 Summary statistics of 3D rms of 6-hour intervals for days 115 – 121 of year 2008 by processing single-frequency data in real-time using the reduced dynamic technique for an 11% duty cycle with full dynamics

The maximum 3D differences are displayed in Table 6.10. The range of the maximum values is again very large. However, with a single-frequency receiver, it is still possible to maintain an accuracy of the solution to within half a kilometre accuracy even with the 11% duty cycle. This is suitable for missions where the accuracy requirements are not very stringent and the power and cost budget is relatively low.

| | **Day 115** | **Day 116** | **Day 117** | **Day 118** | **Day 119** | **Day 120** | **Day 121** |
|---|---|---|---|---|---|---|---|
| **11%** | 330 m | 250 m | 110 m | 410 m | 220 m | 480 m | 340 m |

Table 6.10 Summary statistics of maximum 3D difference of 6-hour intervals for days 115 – 121 of year 2008 by processing single-frequency data in real-time using the reduced dynamic technique for an 11% duty cycle with full dynamics

### 6.4.2 Limited Dynamics

The results for the real-time single-frequency solution with limited dynamics are shown in Figure 6.10 with the associated statistics in Table 6.11. As expected, the real-time single-frequency solution with the 11% duty cycle produces the least accurate results from those investigated in this study. This result comes as no surprise and a mission scenario such as this one should only be utilized when the power budget of the satellite is the bare minimum. A single-frequency receiver with a very low duty cycle and real-time solution requirements thus produces 3D rms values at the level of hundreds of metres. The maximum 3D difference values are displayed in Table 6.12. The maximum error values are now well over the 1 km mark, approaching the 2 km mark. Again, this is not a viable option for missions seeking high accuracy. It is however sufficient for nanosatellite missions with low accuracy requirements, with an extremely low power and cost budget that requires a real-time solution.

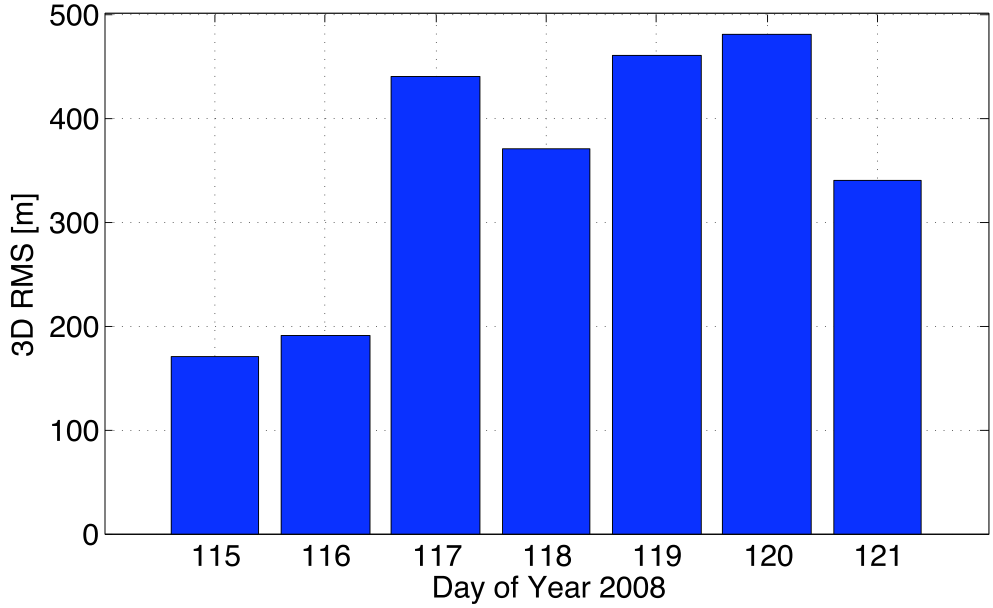


Figure 6.10 3D rms of 6-hour intervals for days 115 – 121 of year 2008 by processing single-frequency data in real-time using the reduced dynamic technique for an 11% duty cycle with limited dynamics

| Mean | Std. Dev. | Maximum | Minimum |
|---|---|---|---|
| 350 m | 126 m | 460 m | 170 m |

Table 6.11 Summary statistics of 3D rms of 6-hour intervals for days 115 – 121 of year 2008 by processing single-frequency data in real-time using the reduced dynamic technique for an 11% duty cycle with limited dynamics

| | Day 115 | Day 116 | Day 117 | Day 118 | Day 119 | Day 120 | Day 121 |
|---|---|---|---|---|---|---|---|
| **11%** | 540 m | 460 m | 1200 m | 1100 m | 1700 m | 1500 m | 710 m |

Table 6.12 Summary statistics of maximum 3D difference of 6-hour intervals for days 115 – 121 of year 2008 by processing single-frequency data in real-time using the reduced dynamic technique for an 11% duty cycle with limited dynamics

# Chapter 7

# 7 Conclusions and Future Work

In this chapter, the research objective is revisited and the outcome is evaluated. The results of the experiments are discussed and analyzed as well. This chapter concludes with suggestions for future research.

## 7.1 Conclusions

The main purpose of this research was to quantify GPS-based LEO orbit determination performance under constrained situations, providing indications of the accuracy of the position solution based on certain parameters. The objectives and results of this research are summarized below:

**Dynamic orbit software development**

The first task of this research was to develop software that would allow the use of dynamic models to predict future states of a LEO. By using various references such as Montenbruck and Gill (2005), software was developed in MATLAB that allows the integration of the equations of motion to predict future states. The accuracy of the gravitational model, various other perturbations and the RK4 integrator was analyzed by comparing the predicted states of the orbit to a reference solution produced by JPL for CHAMP. Increase in accuracy is observed when the degree and order of the gravitational model is increased. In addition, improvements in accuracy become less significant as the degree and the order of the gravitational model is increased, with very little improvement in accuracy beyond 100x100. In terms of achieving good accuracy with other perturbations, modelling air drag is the most important, followed by the lunar gravitational force, solar gravitational force and solar radiation pressure. By including perturbations due to the Sun, Moon, air drag and solar radiation pressure and utilizing a 100x100 gravitational model, the 3D difference after 5 minutes is found to be only 1.6 cm and 55 cm after 30 minutes. These results ensure that the dynamic models will deliver accurate performance that is required by POD.

**GPS-based kinematic orbit software development**

The second task of this research was to develop the software required to conduct the GPS-based constrained experiments. First, PPP software designed to be compatible with LEO data was developed from first principles in MATLAB. In order to decrease processing time, some of the subroutines were developed in C++ and called from MATLAB. The mean 3D rms error for seven different days was found to be 29 cm. Since 29 cm is the $1\sigma$ value, it means that almost the entire solution will be accurate to within 1 m, with the exception of a few outliers. One of the limitations of the kinematic-only orbit solution is that if GPS data are not available for a certain epoch from at least 4 GPS satellites, a solution cannot be produced.

**Reduced dynamic orbit software development**

In order to increase the accuracy of the solution and assure the availability of a solution at each epoch, additional software was developed in MATLAB using the reduced dynamic technique. The reduced dynamic orbit uses both the GPS measurements and the dynamic models combined via an EKF to assure a more accurate and reliable solution. Once implemented, the EKF was tuned by using different data sets. The mean 3D rms error for seven different days was found to be 21 cm, which is a significant improvement over the kinematic-only solution considering that the reduced dynamic technique produces results at every single epoch.

**Constrained orbit solutions**

Once the software was developed and was able to produce state of the art results, recent data from CHAMP was selected to run the experiments. The reduced dynamic software then had to be altered to fulfill the requirements of the various tested scenarios. For example, the implementation of the post-processed orbit solution was different from the real-time orbit solution. Quality control and data combination techniques are different for dual-frequency and single-frequency data, thus each scenario requiring its own version of the reduced dynamic software. The results obtained from the experiments are summarized below in Table 7.1. The general trend that is observed in Table 7.1 is that the solution accuracy declines as one goes downwards in each column. The solution accuracy is degraded as one transitions from dual-frequency to single-frequency data, post-processing to real-time processing and full dynamics to limited dynamics. The utilization of full and limited dynamics is contrasted only in the real-time processing case, because the full complex version of the dynamic models requires more processing time, which may need to be minimized when processing in real-time.

| | **100% DC** | **50% DC** | **25% DC** | **11% DC** | **2 Orbits** | **1 Orbit** |
|---|---|---|---|---|---|---|
| **PP DF** | 15 cm | 42 cm | 70 cm | 9.6 m | 19 cm | 20 cm |
| **PP SF** | 68 cm | 3.9 m | 5.5 m | 36 m | 74 cm | 72 cm |
| **RT DF** | 1.3 m | 3.3 m | 4.9 m | 22 m | 1.3 m | 1.2 m |
| **RT SF** | 1.5 m | 9.3 m | 12 m | 100 m | 1.4 m | 1.4 m |
| **RT DF Limited** | 1.5 m | 24 m | 27 m | 310 m | 1.4 m | 1.3 m |
| **RT SF Limited** | 1.4 m | 25 m | 28 m | 350 m | 1.4 m | 1.4 m |

Table 7.1 Summary of results providing 3D rms values for various constrained scenarios

A point-form summary of the results is presented below:

- As the GPS receiver duty cycle decreases, the error and variability in the solution increase.
- For an application requiring a solution with $1\sigma$ better than half a metre, utilizing a dual-frequency receiver and post-processing the data, a 50% duty cycle would be ideal, thus reserving power onboard the LEO for other equipment. A 25% duty cycle is ideal for an application requiring a solution with a $1\sigma$ value to be better than 1 m.

- When post-processing the data, it is preferable to have the receiver switched on for longer periods in order to achieve maximum accuracy. In real-time processing however, having the receiver switched on for longer periods of time does not necessarily improve the accuracy of the solution.
- When processing in real-time with a dual-frequency receiver, a 25% or 50% GPS receiver duty cycle is suitable for missions that require few metre level accuracy, continuous positioning (or velocity) information and do not have the power capacity to have the GPS receiver switched on at all times.
- When post-processing the data, the utilization of a single-frequency receiver allows for less hardware and thus lower power consumption, while maintaining the 3D rms to well within a metre.
- When processing data in real-time, the increase in accuracy when transitioning from a single-frequency receiver to a dual-frequency receiver does not fully offset the errors associated with real-time processing.
- Increasing the complexity of the dynamic models does not necessarily produce a more accurate solution in the real-time, single-frequency case. Thus for a mission that has a low power budget and a single-frequency receiver, it would be more viable to work with just the $J_2$ gravitational model rather than the full dynamics.

## 7.2 Proposed Future Work

Although much ground has been covered in this research, there are various improvements in the software that can be made, as well as expanding the experiments:

### Software improvements

Although the post-processed, dual-frequency reference solution accuracy is at par with institutions such as JPL and CDAAC, the accuracies in the other scenarios still have room for improvement, particularly the single-frequency solution. There are many extensions that can be added to the current software in order to improve the accuracy of the solution. One way to increase the accuracy of the solution is to add global drag coefficient and solar radiation scale as parameters into the state of the EKF. In order to compensate for any inaccuracies in the dynamic models, radial, along-track and cross-track empirical accelerations can also be added as states into the EKF (Montenbruck et al., 2005). The EKF also requires to be tuned differently for different scenarios, thus producing more realistic standard deviation values. By tweaking the process noise and measurement noise matrices some more for each scenario, the solution has the potential to improve in accuracy. In order to increase the speed of the processor for operational use, the entire code can be compiled. It would also be beneficial to include a transformation function that produces the errors along the radial, along-track and cross-track direction when comparing results to the reference solution. Last but not least, another way to enhance the quality of the results is by making the processor more robust and less data dependent by improving the outlier detection algorithms.

### Further Experiments

The batch of scenarios explored in this study is a small subset of the many different combinations that can be formed by combining the various parameters in different ways.

The scenarios chosen in this study represent the most realistic scenarios that are most likely to come up during mission planning. There do exist however, many scenarios that were not studied here. For example, the 50% duty cycle may be comprised of many different ways. Instead of having the receiver switched on for 15 minutes and switched off for 15 minutes, a mission may require the receiver to be switched on for 30 minutes and switched off for 30 minutes. Although this is a 50% duty cycle, the results will be very different. Thus the results from duty cycles of different lengths can be further explored. In addition, the two types of dynamic models discussed in this study are the full dynamics with a 100x100 gravitational model with all perturbations included and a $J_2$ gravitational model with no other perturbations included. There exist many other options that can be explored with the different mission scenarios as well. For example, a 20x20 gravitational model with no perturbations or a strictly analytical model can also be tested. The list of the various parameter combinations is endless, therefore it is crucial to be efficient and explore those scenarios that would most likely arise during mission planning, as is done in this study.

**Further datasets**

The results obtained with the experiments conducted in this study are meant to represent any LEO, not just CHAMP. Thus running the same experiments with data from other LEOs can provide more information on orbits parameters and accuracy levels. By running other datasets, the processor can also be made to be more robust, thereby ensuring that reliable results will be produced regardless of the dataset. In addition, by automating the quality control parameters the processor will become less dataset dependent. Running experiments using data from LEOs at different altitudes can help us understand how the accuracy levels vary under different constraints at different altitudes. In addition, the experiments can be conducted using The Global Navigation Satellite System (GLONASS) data instead of GPS. Thus by obtaining accuracy level results for different LEOs with GPS and GLONASS data, more information can be available during mission planning.

# References

El-Rabbany, A. (2002). *Introduction to GPS: The Global Positioning System*. Artech House, Norwood, 156 p.

Aoki, S., B. Guinot, G. Kaplan, H. Kinoshita, D. McCarthy and P. Seidelmann (1982). “The New Definition of Universal Time,” *Astronomy and Astrophysics*, Vol. 105, pp. 359-361.

Andersen, P. H., K. Aksnes and H. Skonnord (1998). “Precise ERS-2 orbit determination using SRL, PRARE, and RA observations,” *Journal of Geodesy*, Vol. 72, pp. 421-429.

Arias, E., P. Charlot, M. Feissel and J. Lestrade (1995). “The extragalactic reference system of the International Earth Rotation Service,” *ICRS: Astronomy and Astrophysics*, Vol. 303, pp. 604-608.

Ashby, N. (2007). “Relativity in the Global Positioning System,” *Living Rev. Relativity*, URL http://relativity.livingreviews.org/open?pubNo=lrr-2003-1&page=node1.html. Accessed: Nov., 2010

Beutler, G. (2005). *Methods of Celestial Mechanics: Application to Planetary System, Geodynamics and Satellite Geodesy*. Springer-Verlag, Heidelberg, 451 p.

Bock, H., A. Jaggi, R. Dach, S. Schaer and G. Beutler (2008). “GPS single-frequency orbit determination for low Earth orbiting satellites,” *Advances in Space Research*, Vol. 43, No. 5, pp. 783-791.

Brown, R. and P. Hwang (1997). *Introduction to Random Signals and Applied Kalman Filtering*. John Wiley and Sons, Canada, 484 p.

CDDIS (2009). GNSS Data URL http://cddis.nasa.gov/gnss_datasum.html#daily. Accessed: Jan., 2010.

Colombo, O. and S. Luthcke (2004). “Kinematic Point Positioning of a LEO With simultaneous Reduced-Dynamic Orbit Estimation,” Proceedings of the Institute of Navigation (ION) GNSS-2004 meeting, Long Beach, California, USA, Sept. 2004, pp. 2667-2675.

Connections (2004). Galileo’s Telescope. URL http://cnx.org/content/m11932/latest/. Accessed: March, 2011.

Erdogan, E. and M.O. Karslioglu (2009). "Near Real Time Orbit Determination of BILSAT-1," Recent Advances in Space Technologies, 2009. RAST '09. 4th International Conference, June 11-13, 2009.

Gaudenzi, De R., E. Lijphart and E. Vassallo (1993). "A New High Performance Multipurpose Satellite Tracking System," *IEEE Transactions on Aerospace and Electronic Systems*, Vol. 29, No. 1, pp. 27-43.

Glish, J. (1971). "A Closed-Form Solution for Doppler Satellite Navigation," *IEEE Transactions on Aerospace and Electronic Systems*, Vol. AES-7, No. 5, pp. 875-878.

Grewal, M., L. Weill, and A. Andrews (2007). *Global Positioning Systems, Inertial Navigation, and Integration*. John Wiley and Sons, Hoboken, 525 p.

Grunwaldt, L. (2002). "SLR and the CHAMP Gravity Field Mission," Presentation to 13th International Workshop on Laser Ranging, Washington, DC, USA, October 7-11, 2002.

Gupta, G. K., R. Sacks-Davis and P. E. Tischer (1985). "A Review of Recent Developments in Solving ODEs," *Computing Surveys*, Vol. 17, No. 1, pp. 7-47.

Harris, I. and W. Priester (1962). "Time-Dependent Structure of the Upper Atmosphere," *Journal of the Atmospheric Sciences,* Vol. 19, No. 4, pp. 286-301.

Hightower, J. and G. Borriello (2001). "Location Sensing Techniques," *University of Washington, Computer Science and Engineering*, Seattle, WA., 8 p.

Hugentobler, U. and G. Beutler (2003). "Strategies for Precise Orbit Determination of Low Earth Orbiters Using the GPS," *Space Science Reviews*, Vol. 108, pp. 15–26.

Hwang, C., T. Tang, T. Tseng, T. Lin, D. Svehla and B. Shreiner (2008). "Precise orbit determination for the FORMOSAT-3/COSMIC satellite mission using GPS," *Journal of Geodesy*, Vol. 83, No. 5, pp. 477-489.

IERS (2010). Earth Orientation Data URL http://www.iers.org/nn_10968 /IERS/EN/DataProducts/EarthOrientationData/eop.html?__nnn=true. Accessed: Nov., 2010.

IGS (2009). IGS Products. URL http://igscb.jpl.nasa.gov/components/prods.html. Accessed: March, 2011.

Jaggi, A., U. Hugentobler, H. Bock and G. Beutler (2007). "Precise orbit determination for GRACE using undifferenced or double differenced GPS data," *Advances in Space Research*, Vol. 39, No. 10, pp. 1612-1619.

JPL (2008). Quick Orbits Description URL ftp://sayatnova.jpl.nasa.gov/pub /genesis/orbits/champ/quick/Documents/README.quick. Accessed: Dec., 2010.

JPL (2008). Quick Orbits URL ftp://sayatnova.jpl.nasa.gov/pub/genesis/. Accessed: Nov., 2010.

JPL (2010). Satellite Antenna Corrections URL ftp://igscb.jpl.nasa.gov/igscb /station/general/igs05.atx. Accessed Dec., 2010.

Kaplan, E. and C. Hegarty (2006). *Understanding GPS: Principles and Applications, Second Edition*. Artech House, [Books 24x7 version], Ch.1, 703 p. URL http://common.books24x7.com.ezproxy.library.yorku.ca/book/id_14824/book.asp. Accessed: Nov., 2010.

Kaula, W. (1966). *Theory of Satellite Geodesy*, Blaisdell Publishing Company, Waltham, Massachusetts, 143 p.

Kinoshita, H. and H. Nakai (1989). "Numerical Integration Methods in Dynamical Astronomy," *Celestial Mechanics*, Vol. 45, No. 1, pp. 231-244.

Kouba, J. (2003). "A Guide To Using International GPS Service (IGS) Products," Natural Resources Canada, Geodetic Survey Division, 31 p.

Kouba, J. and P. Héroux (2001). "Precise Point Positioning Using IGS Orbit and Clock Products," *GPS Solutions*, Vol 5., No. 2, pp. 12–28.

Langley, R. (1999). "Dilution of Precision," *GPS World*, May Ed., pp. 52-59.

Leick, A. (2004). *GPS Satellite Surveying*, John Wiley & Sons, Hoboken, 435 p.

Leung, S.Y.F., O. Montenbruck and B. Bruninga (2001). "Hot Start of GPS Receivers for LEO microsatellites," 1st ESA Workshop on Satellite Navigation User Equipment Technologies NAVITEC 2001, ESTEC Noordwijk, 10-12 Dec. 2001.

Lieske, J., T. Lederle, W. Fricke and B. Morando (1977). "Expressions for the Precession Quantities Based upon the IAU (1976) System of Astronomical Constants," *Astronomy and Astrophysics*, Vol. 58, No. 1, pp. 1-16.

Marshal, J. A., S. M. Klosko and J. C. Reis (1995), "Dynamics of SLR Tracked Satellites," *Rev. Geophys.* Vol, 33, Issue S1, pp. 353-360.

Mathworks (2011). Matlab Documentation URL http://www.mathworks.com/help /techdoc/ref/polyfit.html. Accessed Jan., 2011.

Montenbruck, O. (1989). *Practical Ephemeris Calculations*, Springer Verlag, Heidelberg, 146 p.

Montenbruck, O. (2000). "An epoch state filter for use with analytical orbit models of low earth satellites," *Aerospace Science and Technology*, Vol. 4, No. 4, pp. 277–287.

Montenbruck, O. (2003). “Kinematic GPS positioning of LEO satellites using ionosphere-free single frequency measurements,” *Aerospace Science and Technology*, Vol. 7. No. 5, pp. 396-405.

Montenbruck, O. and E. Gill (2005). *Satellite Orbits*. Springer, Berlin, 369 p.

Montenbruck, O. and P. Ramos-Bosch (2007). “Precision real-time navigation of LEO satellites using global positioning system measurements,” *GPS Solutions*, Vol. 12, No. 3, pp. 187-198.

Montenbruck, O. and T. Pfleger (2000). *Astronomy on the Personal Computer*, 4th Edition, Springer Verlag, Heidelberg, 307 p.

Montenbruck, O., T. van Helleputte, R. Kroes and E. Gill (2005). “Reduced dynamic orbit determination using GPS code and carrier measurements,” *Aerospace Science and Technology*, Vol. 9, No. 3, pp. 261-271.

NORAD (2011). About NORAD. URL http://www.norad.mil/about/index.html. Accessed March, 2011.

NRCan (2007). Online Global GPS Processing Service Output Description URL http://www.geod.nrcan.gc.ca/userguide/output/output1_e.php. Accessed Oct., 2010.

NRCan (2010). Online Global GPS Processing Service. http://www.geod.nrcan.gc.ca/products-produits/ppp_e.php. Accessed: Jan., 2011.

Reigber, Ch., H. Jochmann, J. Wünsch, S. Petrovic, P. Schwintzer, F. Barthelmes, K.-H. Neumayer, R. König, Ch. Förste, G. Balmino, R. Biancale, J.-M. Lemoine, S. Loyer and F. Perosanz (2004). “Earth Gravity Field and Seasonal Variability from CHAMP,” Reigber, Ch., Lühr, H., Schwintzer, P., Wickert, J. (eds.), *Earth Observation with CHAMP - Results from Three Years in Orbit*, Springer, Berlin, pp. 25-30.

Sarra, S. (2006). “Chebyshev Interpolation: An Interactive Tour,” *Journal of Online Mathematics and Its Application*”, Vol. 6, No. 1297, pp. 1-10.

Seeber, G. (2003). *Satellite Geodesy*, Walter de Gruyter GmbH and Co. KG, Berling, 2nd Edition, 589 p.

Seidelmann, P. (1982). “1980 IAW Theory of Nutation: The Final Report of the IAW Working Group on Nutation,” *Celestial Mechanics*, Vol. 27, pp. 79-106.

Svehla, D. and M. Rothacher (2003). “Kinematic and reduced-dynamic precise orbit determination of low earth orbiters,” *Advances in Geosciences*, Vol.1, pp. 47–56.

Tapley, B., J. Ries, S. Bettadpur, D. Chambers, M. Cheng, F. Condi, B. Gunter, Z. Kang, P.Nagel, R. Pastor, T. Pekker, S. Poole and F. Wang (2005), “GGM02 – An improved Earth gravity field model form GRACE," *Journal of Geodesy,* Tapley, B., M. Watkins, J. Reis, G. Davis, R. Eanes, S. Poole, H. Rim, B. Schutz, C. Shum, R. Narem, F. Lerch, J. Marshall, S. Klosko, N. Pavlis and R. Williamson (1996). "The Joint Gravity Model 3," *Journal of Geophysical Research* , Vol. 101, pp. 28089-28049.

Wang, M. and Y. Gao (2008). "*A Precise Point Positioning Ambiguity Resolution Method with Narrow-lane Ambiguity Fractional Bias Eliminated*," The University of Calgary, Canada, 8 p.

Willis, P., C. Jayles and G. Tavernier (2004), "Improved DORIS accuracy for Precise Orbit Determination and Geodesy," Institut Geographique National, http://trs-new.jpl.nasa.gov/dspace/handle/2014/37855. Last Accessed: Oct. 2010.

Yamaguchi, S. and T. Tanaka (2006). "GPS Standard Positioning using Kalman filter," presented at the SICE-ICASE International Joint Conference, Bexco, Busan, Korea, Oct. 18-21, 200, pp. 1351-1354.

Yoon, J., K. Lee, B. Lee, B. Kim, K. Choi, Y. Chang, Y. Chun and S. Ra (2004). "Geostationary Orbit Determination for Time Synchronization using Analytical Dynamic Models," *IEEE Transactions on Aerospace and Electronic Systems*, Vol. 40, No. 4, pp. 1132–1146.

Yunck, T., S. Wu, J. Wu and C. Thornton (1990). "Precise Tracking of Remote-Sensing Satellites with the Global Positioning System," *IEEE Transactions of Geoscience and Remote Sensing*, Vol. 28, No.1, pp. 208-116.

# Appendix A: Software Design

The software used in this study was developed from first principles using MATLAB with approximately 3000 lines. Developing the software that produces solutions accurate to the scientific standard was one of the biggest challenges in the completion of this study. This section describes the design and specifications of the software. There are two different types of processors that were developed: the kinematic processor that utilizes just the GPS measurements, and the reduced dynamic orbit.

The kinematic GPS processor uses just the GPS measurements without any dynamic modelling to produce a solution. The design of the kinematic-only software is given in the steps below. The details of each step are described in the body of the thesis.

1. Read observation RINEX file and broadcast navigation message. Reading broadcast navigation message is only required for real-time processing.
2. If post-processing data, read precise clock and orbit files. Then generate the Chebyshev coefficients for the orbits.
3. If post-processing data, begin loop for forward run and backward run to allow smoothing.
4. Begin loop to process each epoch.

5. Filter observations to detect outliers and cycle slips.
6. Generate linear combinations of measurements: ionosphere-free for dual-frequency data and GRAPHIC for single-frequency data.
7. Interpolate precise clock and orbits.
8. Begin residual test loop.
9. Begin sequential least-squares iteration loop.
10. Determine relativistic, Sagnac and phase windup corrections.
11. Apply satellite clock, relativistic, Sagnac and phase windup corrections to the measurements.
12. Use sequential least-squares to determine the correction to the a priori state. If convergence requirement is not met, return to Step 9.
13. Calculate residuals. If the residual requirement for a particular satellite is not met, eliminate the satellite and return to Step 8.
14. Calculate smoothed solution during backward run if post-processing data.
15. Calculate 3D error from reference solution and apply lever arm correction.

These steps are summarized in Figure A.1**.** If a particular epoch contains too many noisy measurements, the produced solution will not be accurate. There are many checkpoints that are placed within the software to check for signs of an inaccurate solution. During the iteration process of the sequential least-squares, the solution is considered invalid if the number of iterations goes above 6. The state for that epoch is declared as unknown. Also, if more than two satellites are rejected due to large residuals, the solution once again is not computed, as it was noted that if more than two large residuals appear in one epoch, the accuracy of the solution will degrade. Finally, if the 3D standard deviation after convergence is too large, the position solution is discarded and considered inaccurate.

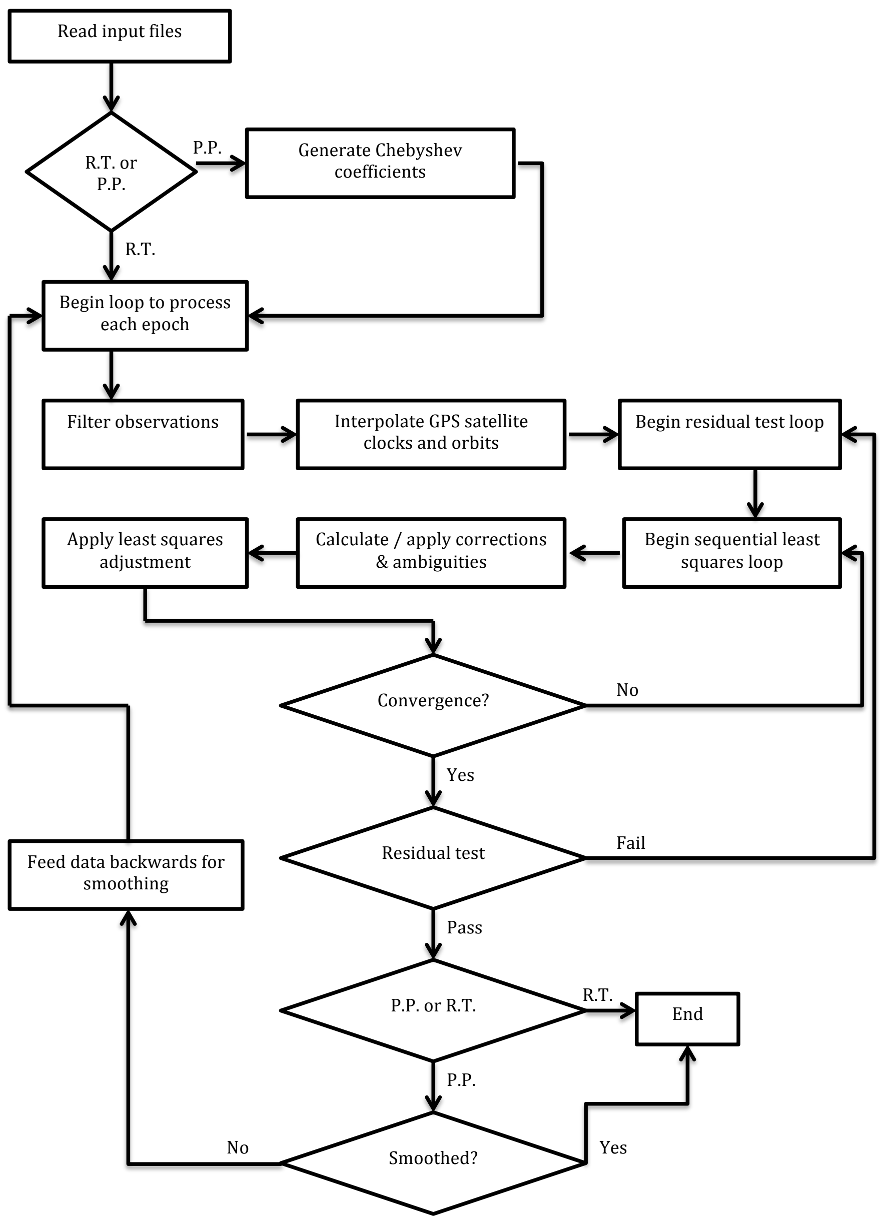


Figure A.1 Kinematic only processor software design

The parameters and different cutoff values are summarized in Table A.1 (NRCan, 2007).

| **Parameter** | **Value** |
|---|---|
| Wide-lane cutoff | 3 m |
| Narrow-lane cutoff | 20 cm |
| 2-D position convergence check | 2 m |
| Ambiguity convergence check | 10 m |
| Pseudorange residual cutoff | 4.47 m |
| Carrier-phase cutoff | 4.6 cm |

Table A.1 Parameters and cutoff values in kinematic only processor

The other processor developed is for the reduced dynamic orbit, which is quite different than the kinematic-only processor. The steps involved in the reduced dynamic orbit are given below:

1. Read observation RINEX file and broadcast navigation message. Reading broadcast navigation message is only required for real-time processing.
2. If post-processing data, read precise clock and orbit files. Then generate the Chebyshev coefficients for the orbits.
3. Calculate coordinate transformation matrices and parameters for the current day.
4. If post-processing data, begin loop for forward run and backward run to allow smoothing.
5. Begin loop to process each epoch.
6. Filter observations to detect outliers and cycle slips.
7. Generate linear combinations of measurements: ionosphere-free for dual-frequency data and GRAPHIC for single-frequency data.
8. Interpolate precise clock and orbits.
9. Apply elevation mask.

10. Begin residual test loop.
11. Determine relativistic, Sagnac and phase windup corrections.
12. Apply satellite clock, relativistic, Sagnac and phase windup corrections to the measurements.
13. Initialize EKF. State is determined using least-squares solution. Covariance is set to default values.
14. EKF
    a. convert state in CRF to TRF
    b. apply time update to covariance
    c. apply measurement update (if GPS data available)
    d. convert state in TRF to CRF
15. Calculate residuals. If the residual requirement for a particular satellite is not met, eliminate the satellite and return to Step 10.
16. Calculate smoothed solution during backward run if post-processing data.
17. Propagate state to next epoch using dynamic models.
18. Calculate 3D error from reference solution and apply lever arm correction.

These steps are summarized in Figure A.2. When GPS data are not available, Steps 6 to 16 are not included. The time update is applied to the state and covariance and the next epoch is processed.

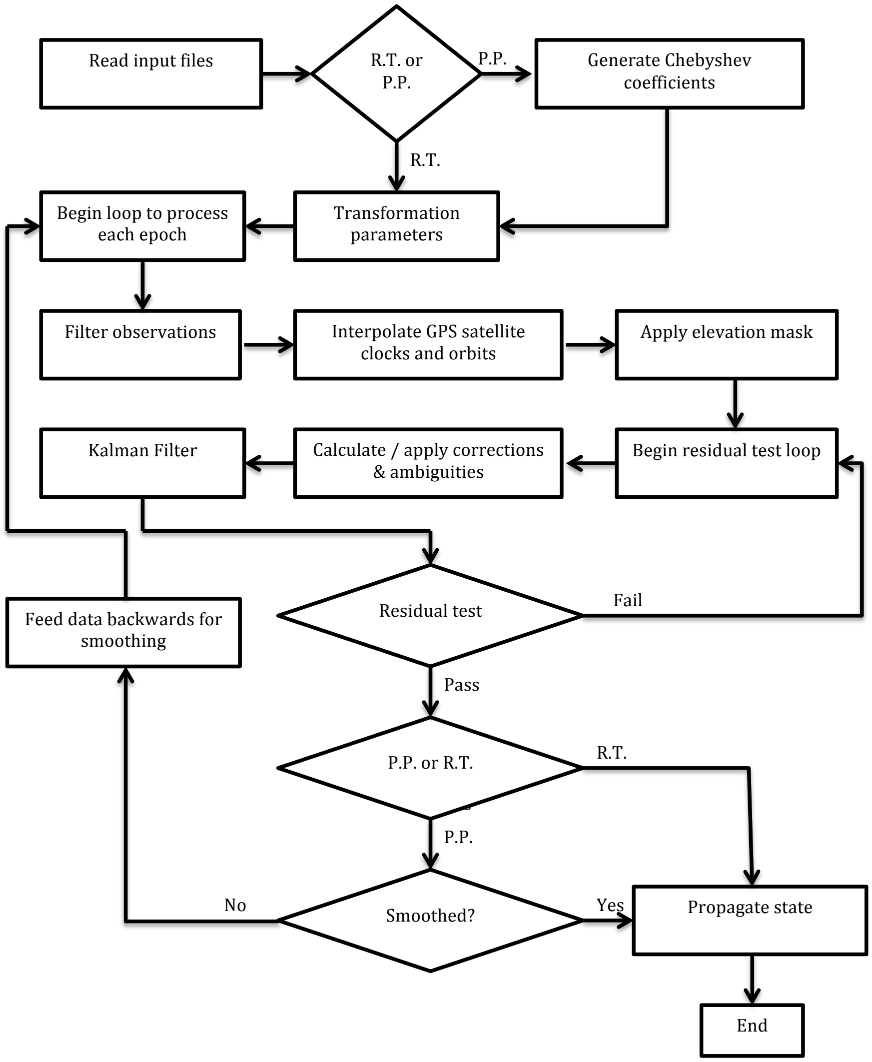


Figure A.2 Reduced dynamic orbit processor software design

The parameters and cutoff values used in the reduced dynamic orbit implementation for the different scenarios are displayed in Table A.2. When the position or the ambiguity standard deviation values, determined empirically, are above the following cutoffs, the dynamic solution is used instead.

| | **PP DF** | **PP SF** | **RT DF** | **RT SF** |
|---|---|---|---|---|
| **Widelane Cutoff** | 3 m | 3 m | 3 m | 3 m |
| **Narrowlane Cutoff** | 20 cm | 20 cm | 20 cm | 20 cm |
| **Elevation Mask** | 9° | 9° | 9° | 9° |
| **Pseudorange residual cutoff** | 4.47 m | 6.47 m | 4.47 m | 6.47 m |
| **Carrier-phase residual cutoff** | 4.6 cm | 46 cm | 4.6 cm | 46 cm |
| **Position Std. Dev. Cutoff** | 10 m | 10 m | 10 m | 10 m |
| **Ambiguity Std. Dev. Cutoff** | 3 m | 3 m | 3 m | 3 m |

Table A.2 Parameters and cutoff values in reduced dynamic orbit

# Appendix B: Low-precision Solar and Lunar Coordinates

For geocentric solar coordinates, assume unperturbed motion of the Earth around the Sun with the following mean orbital elements:

$$a = 149\ 600\ 000\ km \tag{B.1}$$

$$e = 0.016709 \tag{B.2}$$

$$i = 0\overset{\circ}{.}0000 \tag{B.3}$$

$$M = 357\overset{\circ}{.}5256 + 35999\overset{\circ}{.}049 \cdot T \tag{B.4}$$

where

$$T = (JD - 2451545.0)/36525.0 \tag{B.5}$$

which is the number of Julian centuries since 1.5 January 2000 (J2000) and JD is the Julian Date. The Sun's ecliptic longitude $\lambda_{\odot}$ and distance $r_{\odot}$ are determined by:

$$\lambda_{\odot} = \Omega + \omega + M + 6892''\sin M + 72''\sin 2M \tag{B.6}$$

$$r_{\odot} = (149.619 - 2.499\cos M - 0.021\cos 2M) \cdot 10^6 km \tag{B.7}$$

The following rotation is applied to determine the Cartesian coordinates referring to the equator from the previous values:

$$\boldsymbol{r}_\odot = \boldsymbol{R}_x(-\varepsilon)\begin{pmatrix} r_\odot \cos\lambda_\odot \cos\beta_\odot \\ r_\odot \sin\lambda_\odot \cos\beta_\odot \\ r_\odot \sin\beta_\odot \end{pmatrix} \tag{B.8}$$

where

$$\varepsilon = 23\overset{\circ}{.}43929111 \tag{B.9}$$

and

$$\boldsymbol{R}_x(-\varepsilon) = \begin{pmatrix} 1 & 0 & 0 \\ 0 & \cos(-\varepsilon) & \sin(-\varepsilon) \\ 0 & -\sin(-\varepsilon) & \cos(-\varepsilon) \end{pmatrix} \tag{B.10}$$

which is the obliquity of the ecliptic. Since $\beta_\odot = 0$, the expression for $r_\odot$ can be simplified further:

$$\boldsymbol{r}_\odot = \begin{pmatrix} r_\odot \cos\lambda_\odot \\ r_\odot \sin\lambda_\odot \cos\varepsilon \\ r_\odot \sin\lambda_\odot \sin\varepsilon \end{pmatrix} \tag{B.11}$$

The lunar coordinates are calculated based on the following five fundamental arguments: the mean Longitude of the Moon ($L_0$), the Moon's mean anomaly ( $l$ ), the Sun's mean anomaly ( $l'$ ), the mean angular distance of the Moon from the ascending node ($F$) and the difference between the mean longitudes of the Sun and the Moon ($D$).

$$L_0 = 218\overset{\circ}{.}31617 + 481267\overset{\circ}{.}88088 \cdot T - 1\overset{\circ}{.}3972 \cdot T \tag{B.12}$$

$$l = 134\overset{\circ}{.}96292 + 477198\overset{\circ}{.}86753 \cdot T \tag{B.13}$$

$$l' = 357\overset{\circ}{.}52543 + 35999\overset{\circ}{.}04944 \cdot T \tag{B.14}$$

$$F = 93\overset{\circ}{.}27283 + 483202\overset{\circ}{.}01873 \cdot T \tag{B.15}$$

$$D = 297\overset{\circ}{.}85027 + 445267\overset{\circ}{.}11135 \cdot T \tag{B.16}$$

The values of the Moon's longitude with respect to the equinox and ecliptic of the year 2000 is expressed as the obliquity of the ecliptic. Since $\beta_{\odot} = 0$, the expression for $r_{\odot}$ can be simplified further:

$$\boldsymbol{r}_{\odot} = \begin{pmatrix} r_{\odot} \cos \lambda_{\odot} \\ r_{\odot} \sin \lambda_{\odot} \cos \varepsilon \\ r_{\odot} \sin \lambda_{\odot} \sin \varepsilon \end{pmatrix} \tag{B.17}$$

The lunar coordinates are calculated based on the following five fundamental arguments: the mean Longitude of the Moon ($L_0$), the Moon's mean anomaly ( *l* ), the Sun's mean anomaly ( *l'* ), the mean angular distance of the Moon from the ascending node (*F*) and the difference between the mean longitudes of the Sun and the Moon (*D*).

$$L_0 = 218\overset{\circ}{.}31617 + 481267\overset{\circ}{.}88088 \cdot T - 1\overset{\circ}{.}3972 \cdot T \tag{B.18}$$

$$l = 134\overset{\circ}{.}96292 + 477198\overset{\circ}{.}86753 \cdot T \tag{B.19}$$

$$l' = 357\overset{\circ}{.}52543 + 35999\overset{\circ}{.}04944 \cdot T \tag{B.20}$$

$$F = 93\overset{\circ}{.}27283 + 483202\overset{\circ}{.}01873 \cdot T \tag{B.21}$$

$$D = 297\overset{\circ}{.}85027 + 445267\overset{\circ}{.}11135 \cdot T \tag{B.22}$$

The values of the Moon's longitude with respect to the equinox and ecliptic of the year 2000 is expressed as:

$$\lambda_M = L_0 + 22640'' \cdot \sin(l) + 769'' \cdot \sin(2l)$$
$$- 4586'' \cdot \sin(l - 2D) + 2370'' \cdot \sin(2D)$$
$$- 668'' \cdot \sin(l') - 412'' \cdot \sin(2F)$$
$$- 212'' \cdot \sin(2l - 2D) - 206'' \cdot \sin(l + l' - 2D) \tag{B.23}$$
$$+ 192'' \cdot \sin(l + 2D) - 165'' \cdot \sin(l' - 2D)$$
$$+ 148'' \cdot \sin(l - l') - 125'' \cdot \sin(D)$$
$$- 110'' \cdot \sin(l + l') - 55'' \cdot \sin(2F - 2D)$$

The lunar attitude is given by:

$$\beta_M = 18520'' \sin(F + \lambda_M - L_0 + 412 \cdot \sin 2\mathrm{F} + 541 \cdot \sin l')$$
$$- 526'' \cdot \sin(F - 2D) + 44'' \cdot \sin(l + F - 2D)$$
$$- 31'' \cdot \sin(-l + F - 2D) - 25'' \cdot \sin(-2l + F) \tag{B.24}$$
$$- 23'' \cdot \sin(l' + F - 2D) + 21'' \cdot \sin(-l + F)$$
$$+ 11'' \cdot \sin(-l' + F - 2D)$$

The Moon's distance from the centre of the Earth is given by:

$$r_M = (385\,000 - 20\,905 \cos(l) - 3\,699 \cos(2D - l)$$
$$- 2\,956 \cos(2D) - 570 \cos(2l) + 246 \cos(2l - 2D) \tag{B.25}$$
$$- 205 \cos(l' - 2D) - 171 \cos(l + 2D)$$
$$- 152 \cos(l + l' - 2D))\ km$$

The following rotation is applied to determine the equatorial Cartesian coordinates of the Moon:

$$\boldsymbol{r}_M = \boldsymbol{R}_x(-\varepsilon)\begin{pmatrix} r_M \cos\lambda_M \cos\beta_M \\ r_M \sin\lambda_M \cos\beta_M \\ r_M \sin\beta_M \end{pmatrix} \tag{B.26}$$